Search for Exclusive Two Body Decays of $B \to D_s^* h$ at Belle

A dissertation submitted to the

Division of Research and Advanced Studies
of the University of Cincinnati

in partial fulfillment of the
requirements for the degree of

DOCTORATE OF PHILOSOPHY(Ph.D.)

in the department of Physics
of the College of Arts and Sciences

2005

by

Ratnappuli Hewage Luminda Hasantha Kulasiri

B.Sc., University of Colombo, 1996
M.S., University of Cincinnati, 1999

committee chair: Dr. Kay Kinoshita

Abstract

This thesis presents the study of $B^+ \to {D_s}^{*+}\pi^0$, $B^0 \to {D_s}^{*+}\pi^-$ and $B^0 \to {D_s}^{*-}K^+$ decays based on a data sample consisting of 274.8 million $B\bar{B}$ events collected at KEKB accelerator located at KEK in Tsukuba, Japan. KEKB is an asymmetric collider in which electrons and positrons collides at energies 8.5 GeV and 3.0 GeV respectively. The electron-positron collisions produce $\Upsilon(4S)$ mesons which instantly decay into a $B^0\bar{B}^0$ or a B^+B^- pair.

$B^0 \to {D_s}^{*+}\pi^-$ and $B^+ \to {D_s}^{*+}\pi^0$ decays can be used to measure the magnitude of the CKM matrix element V_{ub}. Also the process for $B^0 \to {D_s}^{*+}\pi^-$ decay is the same as that for the doubly Cabibbo suppressed $B^0 \to D^{*+}\pi^-$. It's rate thus provides important input for the measurement of $\sin(2\phi_1 + \phi_3)$ in the time dependent CP violation measurements of $B^0 \to D^{*+}\pi^-$. $\bar{B}^0 \to {D_s}^{*+}K^-$ decays may provide information on W-exchange diagrams and final state interactions. The branching fractions for $B^0 \to {D_s}^{*+}\pi^-$ and $\bar{B}^0 \to {D_s}^{*+}K^-$, are $(2.14 \pm 0.81 \pm 0.26 \pm 0.54) \times 10^{-5}$ and $(1.64 \pm 0.66 \pm 0.23 \pm 0.41) \times 10^{-5}$ respectively. The branching fraction of $B^+ \to {D_s}^{*+}\pi^0$ is $(2.43 \pm 1.12 \pm 0.42 \pm 0.61) \times 10^{-5}$. First the statistical uncertainty is shown and the second is systematic uncertainty excluding the systematic uncertainty of the branching fraction of $D_s \to \phi\pi$. The third error is from the systematic uncertainty of the branching fraction of $D_s \to \phi\pi$.

To my beloved parents

Ratnappuli Hewage Kulasiri

and

Ramanie Kumudulatha Kulasiri

Acknowledgments

I have been extremely lucky to be a graduate student at the department of physics, university of Cincinnati and have the guidance, support, and friendship throughout my graduate student life. It has been a fruitful, educational as well as enjoyable time, that I have passed several important mile stones in my life. I would like to thank everyone who helped me in many ways in this period.

First and foremost, I would like to thank my adviser Prof. Kay Kinoshita for introducing me to the field of high energy physics. I also express my sincere gratitude to her for helping and guiding me throughout the research. Under her guidance I got the opportunity to work at the the High Energy Accelerator Research Organization(KEK) in Tsukuba, Japan as a member of the Belle Collaboration. It was a very productive time and I was able to learn a lot in those stays at KEK. I would also like to thank Prof. Alan Schwartz, who introduced me to hardware in high energy physics, and giving me the opportunity to work in HERA-B experiment at DESY, Hamburg, Germany. I am grateful to Prof. Rohana Wijewardhana for his help and advice during my stay in Cincinnati. I thank Prof. Mike Sokoloff, Prof. Alex Kegan, and Prof. Hans-Peter Wagner as well as Prof. Kay Kinoshita for serving in my dissertation committee.

Many thanks to my friends Ajith, Prasanna, Nimal, Athua and Seema who helped me in various ways. I would like to thank my friends at KEK, where I enjoyed their company and friendship, Suneel, Nitesh and Debrat. I specially like to thank Tim

Gershon, for his useful suggestions, and presenting my reports to the sub group when the video conferencing system fails. I am grateful to Alexey Drutskoy for the fruitful discussions, I had with him in the latter part of my analysis. I would like to extend my thanks to David Will, for helping me with the computer issues.

My special thanks to my wife Kisa and my son Nelitha for being with me all the time. I appreciate their encouragement, support and patience throughout.

Last but not least, I would like to express my indebtedness to my parents for their love, support, and understanding in all my life. Without you I would never have come this far.

Contents

List of Figures

List of Tables

Chapter 1

Introduction

1.1 The Standard Model

The Standard Model is a theory of fundamental particles and their interactions[**?**]. These particles also called elementary particles, are divided into two categories, quarks and leptons. Both quarks and leptons are fermions with spin angular momentum equal to $\frac{1}{2}$. There are three generations of quarks and leptons and their antiparticles. Table 1.1 shows these particles and their properties.

	Charge	1^{st} generation	2^{nd} generation	3^{rd} generation
Quark	$+\frac{2}{3}$	u(up)	c(charm)	t(top)
	$-\frac{1}{3}$	d(down)	s(strange)	b(bottom)
Lepton	0	ν_e(e neutrino)	ν_μ(μ neutrino)	ν_τ(τ neutrino)
	-1	e(electron)	μ(muon)	τ(tau)

Table 1.1: Quarks and Leptons

Quarks		Leptons	
flavor	Mass(MeV/c^2)	flavor	Mass(MeV/c^2)
u	1.5 - 4.0	e	0.511 ± 0.000
d	4 - 8	ν_e	$< 3 \times 10^{-6}$
c	1.15 - 1.35	μ	0.113 ± 0.000
s	80 - 130	ν_μ	< 0.19
t	$(174.3 \pm 5.1) \times 10^3$	τ	$1776.99^{+0.29}_{-0.26}$
b	4.1 - 4.4	ν_τ	< 18.2

Table 1.2: Masses of Quarks and Leptons

In addition there are gluons, photons, and W and Z bosons which are force carriers. Gluons are responsible for strong interactions, and photons are responsible for electromagnetic interactions. Weak interactions occur through W and Z bosons. Since the quark mass eigen states are not the same as electroweak eigenstates, a matrix relating these bases was defined for six quarks. In convention, the mixing is often expressed in terms of a 3×3 unitary matrix V operating on the charge $-e/3$ quark mass eigenstates (d, s, and b);

$$\begin{pmatrix} \mathrm{d'} \\ \mathrm{s'} \\ \mathrm{b'} \end{pmatrix} = \begin{pmatrix} V_{ud} & V_{us} & V_{ub} \\ V_{cd} & V_{cs} & V_{cb} \\ V_{td} & V_{ts} & V_{tb} \end{pmatrix} \begin{pmatrix} \mathrm{d} \\ \mathrm{s} \\ \mathrm{b} \end{pmatrix} \tag{1.1}$$

Gauge boson	Interaction	Charge	Mass(GeV/c^2)
γ	electroweak	0	$< 6 \times 10^{-23}$
$W^{\pm}$	electroweak	± 1	80.425 ± 0.038
Z^0	electroweak	0	91.188 ± 0.002
g	strong	0	0

Table 1.3: Gauge bosons

V is known as the Cabibbo-Kobayashi-Maskawa(CKM) Matrix[?] [?]. It can be represented approximately in the parametric form,

$$V = \begin{pmatrix} 1-\lambda^2 & \lambda & A\lambda^3(\rho - i\eta) \\ -\lambda & 1-\lambda^2/2 & A\lambda^2 \\ A\lambda^3(1-\rho-i\eta) & -A\lambda^2 & 1 \end{pmatrix} + O(\lambda^4). \tag{1.2}$$

Where λ is the sine of the Cabibbo angle[?]. A, λ, and η are real numbers. The values of the individual matrix elements can be determined from weak decays of the relevant quarks or deep inelastic neutrino scattering. Assuming only three generations, the 90% confident limits on the magnitudes of the matrix elements are[?],

$$\begin{pmatrix} 0.9741 \;\; to \;\; 0.9756 & 0.219 \;\; to \;\; 0.226 & 0.0025 \;\; to \;\; 0.0048 \\ 0.219 \;\; to \;\; 0.226 & 0.9732 \;\; to \;\; 0.9748 & 0.038 \;\; to \;\; 0.044 \\ 0.004 \;\; to \;\; 0.014 & 0.037 \;\; to \;\; 0.044 & 0.9990 \;\; to \;\; 0.9993 \end{pmatrix} \tag{1.3}$$

The unitarity of V gives $VV^\dagger = 1$ and leads to six unitarity triangles in the complex plane. They can be obtained by the relation,

$$\sum_j V_{ij}V^*_{jk} = 0 \text{ (i} \neq \text{k)} \tag{1.4}$$

In the explicit form,

$$V_{ud}V^*_{us} + V_{cd}V^*_{cs} + V_{td}V^*_{ts} = 0 \tag{1.5}$$

$$V_{ud}V^*_{cd} + V_{us}V^*_{cs} + V_{ub}V^*_{cb} = 0 \tag{1.6}$$

$$V_{us}V^*_{ub} + V_{cs}V^*_{cb} + V_{ts}V^*_{tb} = 0 \tag{1.7}$$

$$V_{cd}V^*_{td} + V_{cs}V^*_{ts} + V_{cb}V^*_{tb} = 0 \tag{1.8}$$

$$V_{ud}V^*_{td} + V_{us}V^*_{ts} + V_{ub}V^*_{tb} = 0 \tag{1.9}$$

$$V_{ud}V^*_{ub} + V_{cd}V^*_{cb} + V_{td}V^*_{tb} = 0 \tag{1.10}$$

The last equation represents the orthogonality of the first and third column is the most promising one for the CP violation. The CP violation in the B system relates to this triangle.

The angles of the unitarity triangle, ϕ_1,ϕ_2, ϕ_3 are given by,

$$\begin{aligned} \phi_1 &= \pi - arg(\tfrac{-V_{td}V^*_{tb}}{-V_{cd}V^*_{cb}}); \\ \phi_2 &= arg(\tfrac{V_{td}V^*_{tb}}{-V_{ud}V^*_{ub}}); \\ \phi_3 &= arg(\tfrac{V_{ud}V^*_{ub}}{-V_{cd}V^*_{cb}}). \end{aligned} \tag{1.11}$$

In some texts ϕ_1, ϕ_2 and ϕ_3 are referred as β, α and γ respectively. Precise determination of ϕ_1, ϕ_2 and ϕ_3, needed to confirm or refute the Standard Model. If the three

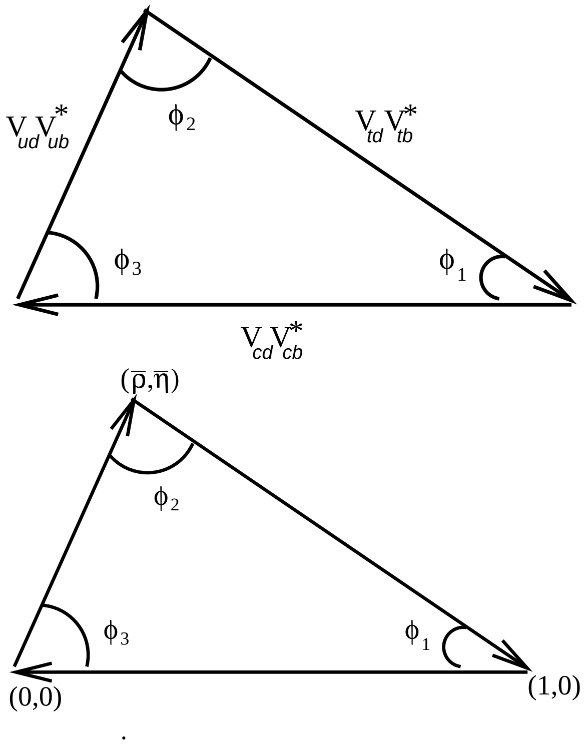

Figure 1.1: Top: Representation in the complex plane of the triangle formed by the CKM matrix elements $V_{ud}V_{ub}^*$, $V_{cd}V_{cb}^*$ and $V_{td}V_{tb}^*$. Bottom: Rescaled triangle with vertices at (0,0), (0,1) and ($\bar{\rho}$,$\bar{\eta}$). $\bar{\rho}$ and $\bar{\eta}$ are $\rho(1-\lambda^2/2)$ and $\eta(1-\lambda^2/2)$ respectively in the Wolfenstein parametrization[**?**]

angles of the CKM matrix is not consistent with 180^0, it implies New Physics beyond the Standard Model. Observation of the decay of a B meson to a D_s^* meson and a $\pi^{0/\pm}$ ($B \to D_s{}^*\pi^{0/\pm}$) would provide opportunity to evaluate the CKM parameter V_{ub}. The decay $B^0 \to D_s{}^{*+}\pi^-$ provide important input for the measurement of the angle $(2\phi_1 + \phi_3)$ where ϕ_1 and ϕ_3 are the angles of the unitarity triangle.

1.2 CP Violation

1.2.1 Charge conjugation(C)

Charge conjugation(C) replaces all particles by their antiparticles, in the same state. C remains invariant in the strong and electromagnetic interactions but is violated by the weak interactions.

1.2.2 Parity(P)

Parity(P) operator changes the sign of the position vector($\vec{r}$). Hence it changes the sign of momentum vector($\vec{p}$), but does not change the sign of the angular momentum vector($\vec{L}$) since $\vec{L} = \vec{r} \times \vec{p}$.

1.2.3 CP violation

CP considered an invariant until J. H. Christenson et al.[**?**] discovered CP violation in the Kaon system in 1964. There are two neutral kaons K^0 and $\bar{K^0}$ where $\bar{K^0}$ is the antiparticle of K^0. The quark combinations of K^0 and $\bar{K}^0$ mesons are $d\bar{s}$ and $\bar{d}s$ respectively. From the definition,

$$CP|K^0\rangle = -|\bar{K^0}\rangle \tag{1.12}$$

then the possible CP eigen states can be written as

$$|K_1^0\rangle = \frac{1}{\sqrt{2}}(|K^0\rangle - |\bar{K^0}\rangle); \quad |K_2^0\rangle = \frac{1}{\sqrt{2}}(|K^0\rangle + |\bar{K^0}\rangle); \tag{1.13}$$

with eigen values +1 and −1 respectively. The two mesons K_1^0 and K_2^0 were identified as K_S^0 and K_L^0, where K_S^0 has a shorter life time. Since K_S^0 has CP eigen value +1 it is expected to decay 2π states, while K_L^0 which has CP eigen value −1 expected to decay 3π states. The small fractional decay ${K_L}^0 \to \pi^+\pi^-$ (branching fraction $= (2.090 \pm 0.025) \times 10^{-3}$)[?] is an evidence for the CP violation in the kaon system. Hence the real ${K_S}^0$ and ${K_L}^0$ states can be given as,

$$\begin{aligned} |K_S^0\rangle &= \tfrac{1}{\sqrt{1+|\epsilon|^2}}(|K_1^0\rangle + \epsilon|K_2^0\rangle) \\ |K_L^0\rangle &= \tfrac{1}{\sqrt{1+|\epsilon|^2}}(\epsilon|K_1^0\rangle + |K_2^0\rangle) \end{aligned} \tag{1.14}$$

where $|\ \epsilon\ |$ is a small complex parameter and its value is $(2.284 \pm 0.014) \times 10^{-3}$ [?].

1.2.4 CP violation in the B meson system

CP violation can occur in both charged and neutral B decays. There are three possible ways.

1. When the amplitude for a decay and its CP Conjugate process have different magnitudes - occur in both charged and neutral B decays

2. CP violation in mixing - occurs when mass eigen states of the neutral B's are not CP eigen states.

3. CP violation in the interference between decays with and without mixing - occurs when B and $\bar{B}$ decays into a same final state.

1.2.5 B-$\bar{B}$ mixing

An arbitrary combination of a neutral B meson state can be written as

$$a|B^0\rangle + b|\bar{B}^0\rangle \tag{1.15}$$

and $CP|B^0\rangle = -|\bar{B}^0\rangle$. Then the time dependent Schrödinger equation

$$i\frac{d}{dt}\begin{pmatrix} a \\ \\ b \end{pmatrix} = H\begin{pmatrix} a \\ \\ b \end{pmatrix} \equiv \begin{pmatrix} M - \frac{i}{2}\Gamma \end{pmatrix}\begin{pmatrix} a \\ \\ b \end{pmatrix} \tag{1.16}$$

Hamiltonian H is defined as

$$H = M - i\Gamma = \begin{pmatrix} M_{11} - \frac{i}{2}\Gamma_{11} & M_{12} - \frac{i}{2}\Gamma_{12} \\ \\ M_{21} - \frac{i}{2}\Gamma_{21} & M_{22} - \frac{i}{2}\Gamma_{22} \end{pmatrix} \tag{1.17}$$

M and Γ which represents real and imaginary parts respectively, are Hermitian matrices. Assuming CPT invariance where T is the time reversal operator, $H_{11} = H_{22}$. Lets consider $M_{11} = M_{22} = M'$ and $\Gamma_{11} = \Gamma_{22} = \Gamma'$. Here M' and Γ' represent mass and width respectively. Then the eigen values $\lambda_{\pm}$ are,

$$\lambda_{\pm} = (M' - \frac{i}{2}\Gamma') \pm \sqrt{(M_{12} - \frac{i}{2}\Gamma_{12})(M^*_{12} - \frac{i}{2}\Gamma^*_{12})} \tag{1.18}$$

The mass eigen states can be written as

$$|B_L\rangle = p|B^0\rangle + q|\bar{B}^0\rangle) \tag{1.19}$$

$$|B_H\rangle = p|B^0\rangle - q|\bar{B}^0\rangle) \tag{1.20}$$

with the normalization condition $\mid q^2 \mid + \mid p^2 \mid= 1$. The ratio

$$\frac{q}{p} = +\sqrt{\frac{M^*_{12} - \frac{i}{2}\Gamma^*_{12}}{M_{12} - \frac{i}{2}\Gamma_{12}}} \tag{1.21}$$

λ_- and λ_+ correspond to $|B_H\rangle$ and $|B_L\rangle$ respectively. By considering the time evolution of the B meson mass eigen states,

$$|B_H(t)\rangle = e^{-iM_H t} e^{\frac{-\Gamma_H t}{2}} |B_H\rangle, \tag{1.22}$$

$$|B_L(t)\rangle = e^{-iM_L t} e^{\frac{-\Gamma_L t}{2}} |B_L\rangle \tag{1.23}$$

We can transform the mass eigen states to weak interaction eigen states by $|B^0\rangle = (|B_L\rangle + |B_H\rangle)/2p$ and $|\bar{B}^0\rangle = (|B_L\rangle - |B_H\rangle)/2q$ assuming $|B^0\rangle$ and $|\bar{B}^0\rangle$ are neutral B mesons at time t=0. Hence at time t,

$$|B^0(t)\rangle = \frac{1}{2}[(e^{-iM_H t} e^{\frac{-\Gamma_H t}{2}} + e^{-iM_L t} e^{\frac{-\Gamma_L t}{2}})|B^0\rangle - \frac{q}{p}(e^{-iM_H t} e^{\frac{-\Gamma_H t}{2}} - e^{-iM_L t} e^{\frac{-\Gamma_L t}{2}})|\bar{B}^0\rangle] \tag{1.24}$$

$$\begin{aligned} = \ & \tfrac{1}{2} e^{-\frac{i}{2}(M_H+M_L)t} e^{-\frac{1}{4}(\Gamma_H+\Gamma_L)} [(e^{-i\frac{(M_H-M_L)t}{2}} e^{\frac{-(\Gamma_H-\Gamma_L)t}{4}} + e^{-i\frac{(M_L-M_H)t}{2}} e^{\frac{-(\Gamma_L-\Gamma_H)t}{4}})|B^0\rangle \\ & -\tfrac{q}{p}(e^{-i\frac{(M_H-M_L)t}{2}} e^{\frac{-(\Gamma_H-\Gamma_L)t}{4}} - e^{-i\frac{(M_L-M_H)t}{2}} e^{\frac{-(\Gamma_L-\Gamma_H)t}{4}})|\bar{B}^0\rangle] \end{aligned} \tag{1.25}$$

Let $M_H - M_L = \Delta M$ and $\Gamma_H - \Gamma_L = \Delta\Gamma$ Let $\frac{M_H+M_L}{2} = M$ and $\frac{\Gamma_L+\Gamma_H}{2} = \Gamma$

$$\begin{aligned} = \ & \tfrac{1}{2} e^{-iMt} e^{-\frac{1}{2}(\Gamma)} [(e^{-\frac{i}{2}(\Delta M)t} e^{\frac{-(\Delta\Gamma)t}{4}} + e^{\frac{i}{2}(\Delta M)t} e^{\frac{(\Delta\Gamma)t}{4}})|B^0\rangle \\ & -\tfrac{q}{p}(e^{-\frac{i}{2}(\Delta M)t} e^{\frac{-(\Delta\Gamma)t}{4}} - e^{\frac{i}{2}(\Delta M)t} e^{\frac{(\Delta\Gamma)t}{4}}|\bar{B}^0\rangle] \end{aligned} \tag{1.26}$$

Assume $\Delta\Gamma << \Delta M$. then,

$$|B^0(t)\rangle = \ e^{-iMt} e^{-\frac{1}{2}(\Gamma)} [cos(\tfrac{\Delta M t}{2})|B^0\rangle + \tfrac{iq}{p} sin(\tfrac{\Delta M t}{2})|\bar{B}^0\rangle] \tag{1.27}$$

similarly

$$\begin{aligned} |\bar{B}^0(t)\rangle \ & = -\tfrac{1}{2}[\tfrac{p}{q}(e^{-iM_H t} e^{\frac{-\Gamma_H t}{2}} - e^{-iM_L t} e^{\frac{-\Gamma_L t}{2}})|B^0\rangle - (e^{-iM_H t} e^{\frac{-\Gamma_H t}{2}} + e^{-iM_L t} e^{\frac{-\Gamma_L t}{2}})|\bar{B}^0\rangle] \\ & = e^{-iMt} e^{-\frac{1}{2}(\Gamma)} [\tfrac{ip}{q} sin(\tfrac{\Delta M t}{2})|B^0\rangle + cos(\tfrac{\Delta M t}{2})|\bar{B}^0\rangle] \end{aligned} \tag{1.28}$$

If f and $\bar{f}$ are final states of the decays of B^0 and $\bar{B^0}$, any asymmetry in decay rates of $B^0 \to f$ and $\bar{B^0} \to f$ indicates CP violation. The time dependent asymmetry can be given,

$$\begin{aligned} A_{CP}(t) &= \tfrac{\Gamma[\bar{B^0}(t)\to f]-\Gamma[B^0(t)\to f]}{\Gamma[\bar{B^0}(t)\to f]+\Gamma[B^0(t)\to f]} \\ &= \tfrac{-1}{(1+|\lambda_f|^2)}[(1- \mid \lambda_f \mid^2)cos(\Delta m_B t) + 2Im\lambda_f sin(\Delta m_B t)] \end{aligned} \tag{1.29}$$

Δm_B is the mass difference between B^0 and $\bar{B^0}$, and λ_f is defined as,

$$\lambda_f = \frac{q\bar{A}_f}{pA_f} \tag{1.30}$$

A_f is the decay amplitude of $B^0 \to f$ and $\bar{A}_f$ is the decay amplitude of $\bar{B^0} \to f$. In Eqn. 1.29, $cos(\Delta m_B t)$ and $sin(\Delta m_B t)$ terms represent direct and indirect CP violations respectively. Recently Belle and Babar experiments observed CP violation in the B meson system. CP violation is allowed in the Standard Model but highly suppressed. The decays $B^0 \to D_s^{*+}\pi^-$ and $B^+ \to D_s^{*+}\pi^0$ can be used to estimate the value of the CKM matrix parameter V_{ub}. Also measuring $\sin(2\phi_1 + \phi_3)$ is important because estimation of all the angles of the unitarity traingle can be used to approve or deny the standard model. Further discussion on $B \to D_s^{*+}h$ decays can be found in chapter 3.

Chapter 2

Experimental Apparatus

The primary goal of the Belle experiment is to measure CP violation in the B meson system. To achieve this goal it is required a high luminosity accelerator with a detector capable of measuring the proper time difference between neutral B meson and its conjugate partner ($\bar{B}^0$). Typical decay distance for B mesons at Belle Detector is 200 μm. $B\bar{B}$ pairs are produced at the KEKB accelerator and the subsequent decay particles are detected by the Belle detector. Together with the sub detectors of the Belle Detector, Belle DAQ system (Data Acquisition System) collects and stores the data for analyses.

2.1 The KEKB Accelerator

The KEK B-factory, KEKB is an asymmetric energy collider with 8 GeV electron and 3.5 GeV positron beams built in a 3 km long tunnel. Electrons and positrons are injected into the storage rings using a linear accelerator (LINAC). The energy difference between the electron and positron beams gives a boost to the produced B meson pairs ($B\bar{B}$). This makes it possible to measure time dependent features of B meson decays. The electron beam and positron beam cross at one point called the interaction point (IP), where electrons and positrons collide. At the interaction point electron and positron beams crosses each other at an angle of ± 22 mrad. This helps to reduce parasitic collisions near the interaction region. Also there is no need for beam separating magnets and this reduces the synchrotron radiation significantly at the interaction point. The belle detector surrounds the IP to catch particles produced by the collisions. The design luminosity is 1.0×10^{34} cm^{-2}s^{-1}. Design beam currents are 2.6 A and 1.1 A for the positron and electron beams respectively. Other important design parameters are shown in table 2.1[?]. The emittance is defined as the region that the particles in a beam can occupy in phase space. β_x^* and β_y^* are known as betatron functions at the interaction point. Lower betatron functions give higher luminosities.

Particles	LER e^+	HER e^-	Units
Horizontal Emittance	18	18	nm
Beam Current	2.6	1.1	A
Number of Bunches	5000		
beta's at IP β_x^*/β_y^*	33/1	33/1	cm
Luminosity	10.0		$10^{33} cm^{-2} s^{-1}$
Energy	3.5	8.0	GeV
Crossing Angle	11		mrad

Table 2.1: Design Parameters of the KEKB

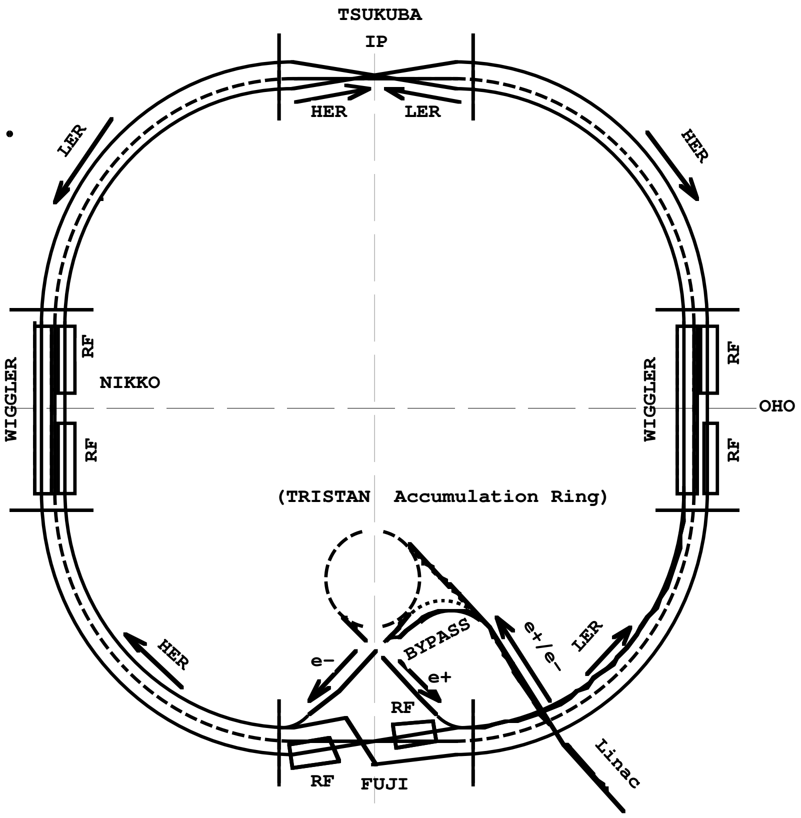

Figure 2.1: KEKB Accelerator-Two electron and positron storage rings and the linac is shown. The interaction point is at the Tsukuba area where the detector is placed. At the interaction point electrons and positrons collides each other and produce $\Upsilon(4S)$ mesons which immediately decays to $B\bar{B}$ pairs.

2.2 Belle Detector

2.2.1 Overview

Belle Detector is installed at the interaction point(IP) of the electron positron beams. The detector is configured with a 1.5 T super-conducting solenoid, which provide the magnetic field for the charged particle detection. B meson decay vertices are measured by the Silicon Vertex Detector (SVD)[?], installed just outside the beryllium beam pipe. Charged particle reconstruction is provided by a wire drift chamber,

	LER	HER	Units
Horizontal Emittance	18	24	nm
Beam Current	1580	1200	mA
Number of Bunches	1289		
beta's at IP β_x^*/β_y^*	59/0.52	56/0.65	cm
Estimated Vertical beam size at IP $\sigma^*{}_y$	2.1	2.1	μm
Beam Lifetime	152@1580	178@1200	min.@mA
Luminosity	13.92		$10^{33}cm^{-2}s^{-1}$

Table 2.2: Accelerator Parameters of the KEKB in Summer, 2004

called Central Drift Chamber (CDC)[?]. Particle identification is provided by dE/dx measurements in CDC, Aerogel Cherenkov Counter (ACC)[?][?] and Time of flight Counters (ToF)[?]. Electrons and photons create showers in the Electromagnetic Calorimeter (ECL), consisting of CsI(Tl) crystals. Resistive plate counters in the Klong and Muon Detector (KLM) detects K_L and muons. The standard coordinate system of the Belle detector is as follows,

- x: horizontally outward from the IP
- y: vertically outward from the IP
- z: along the beam axis to the opposite direction of the positron beam

The beam pipe which is at the center of the detector, is made of double wall beryllium cylinder with an inner radius of 20 mm. The thickness is 0.5 mm. The space between the walls is 2.5 mm. Helium gas is filled between the walls and used for the cooling.

2.2.2 Silicon Vertex Detector (SVD)

Due to the asymmetric energies of the two colliding beams, the two B mesons are produced with $\beta\gamma = 0.425$ in the laboratory frame. Therefore the time difference

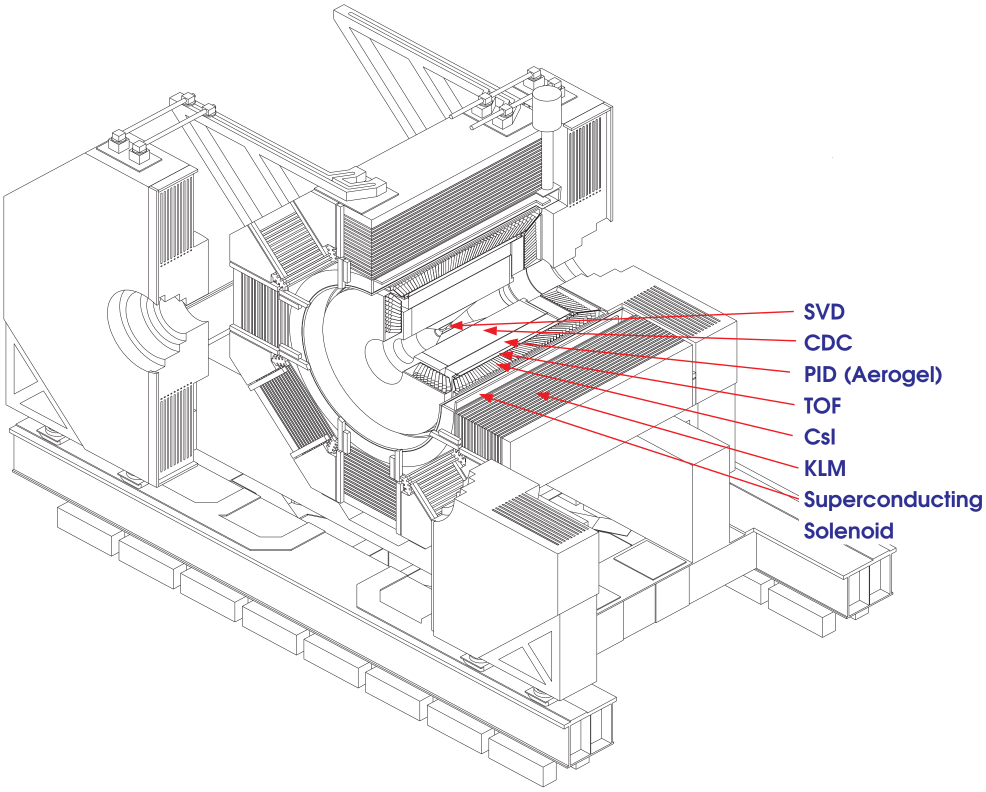

Figure 2.2: Belle Detector

between the two B-meson decays can be determined by measuring the difference of the decay vertex positions. Since the average distance between the two vertices is 200 μm, the vertex detector must be capable of measuring the distance between them with a precision of 100 μm [**?**].

The initial version of the Belle Silicon Vertex Detector (SVD 1), was replaced by SVD 1.2 and SVD 1.4 in 1999 and 2000 respectively. However all those versions are similar in geometrical and electrical configuration, except for the improvements in radiation hardness in the silicon sensors and front end electronics. These consisted

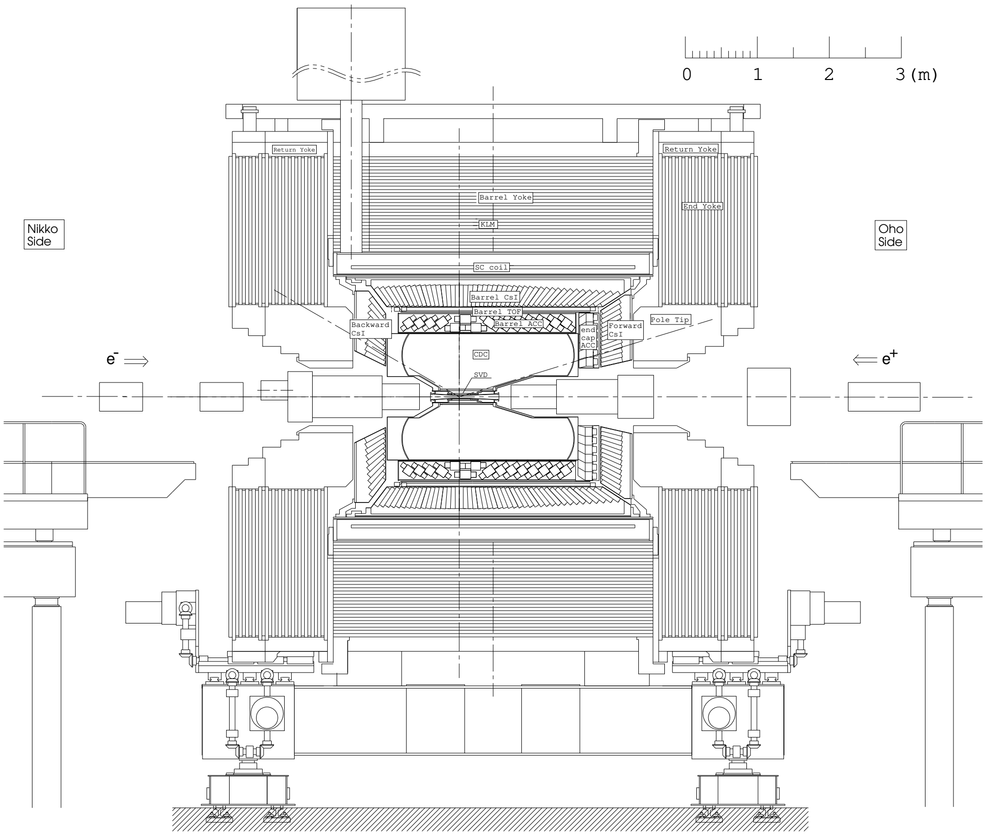

Figure 2.3: Side View of the belle Detector

of three concentric cylindrical layers of silicon sensors and covers the angular range $23^0 < \theta < 139^0$ where θ is the angle from the beam axis. The radii of the three layers are 30, 45.5, 60.5 mm. With record level luminosities, a new SVD (SVD 2) was built to enhance the radiation tolerance, to increase the acceptance and to introduce SVD information into the Belle level-1 trigger[?]. The following discussion is about the SVD 2 which is the current version. SVD 2 has four layers; the radii are 20.0, 43.5, 70.0 and 88.0 mm, respectively. The angular acceptance is expanded to $17^0 < \theta < 150^0$ which is the same as the outer tracker, the Central Drift Camber

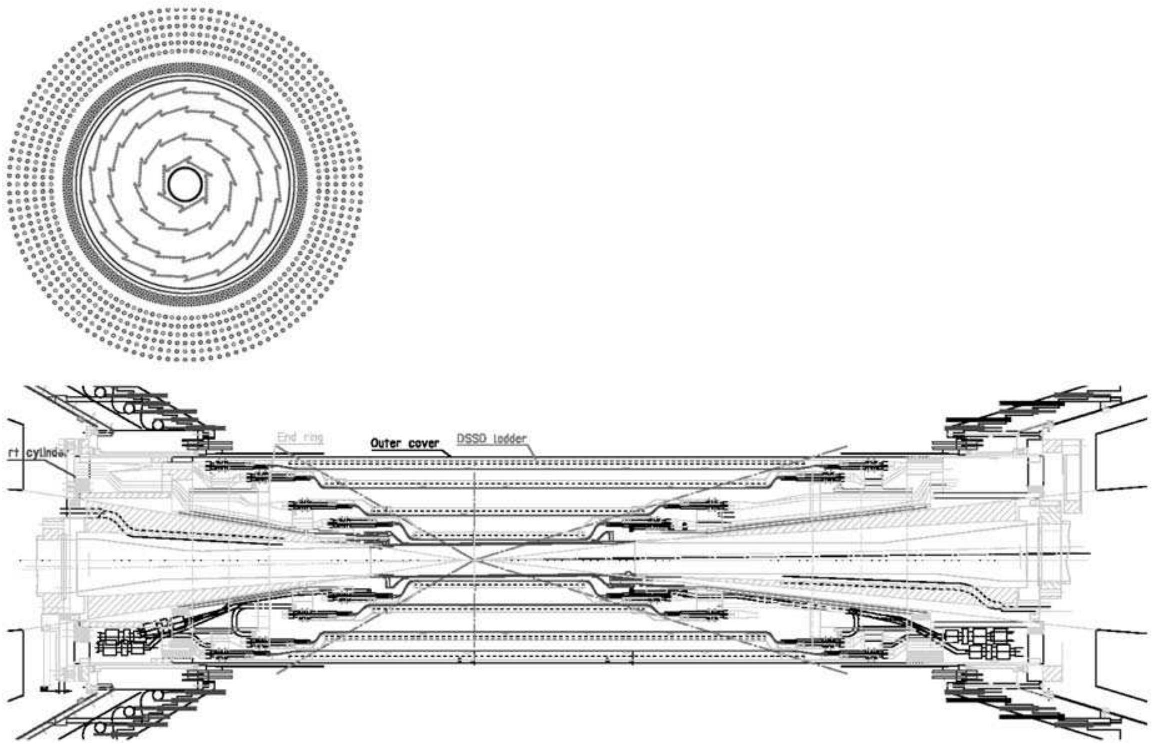

Figure 2.4: Configuration of the Belle SVD 2- The top diagram shows the end view and the bottom diagram shoes the side view.

(CDC). The radius of the beam pipe is reduced from 20 to 15 mm, so that we can place the sensor closer to the interaction point and achieve better vertex resolution. Each layer consists of DSSDs (Double Sided Silicon Strip Detectors). In layer 1/2/3/4, we have 2/3/5/6 DSSDs along the z direction in a ladder, and 6/12/18/18 ladders to cover the ϕ region respectively. When charged particles pass through the DSSDs it produces electron-hole pairs which can be read as a signal using the sense strips.

2.2.3 Central Drift Chamber (CDC)

Central Drift Chamber (CDC) is the primary device for charged particle tracking. The CDC is located in a 1.5 T magnetic field provided by a superconducting solenoid. The CDC covers a polar angle region of $17^0 \leq \theta \leq 150^0$. The main use of the CDC is to determine the precise three dimensional trajectories of the charged particles providing measurements for charged particle momentum vectors. Also the energy loss in the chamber (dE/dx) is used to identify particles. The energy loss primarily occur by ionization and atomic excitation.

Belle CDC is a cylindrical wire drift chamber that contains 50 layers of anode wires and three cathode strip layers. The layers of anode wires consists of 32 axial wires and 18 small angle-stereo layers. The length is 2400 mm, and the inner and outer radii are 83 and 874 mm respectively. The CDC is asymmetric in the z-direction in order to accommodate the fact that the particles from $\Upsilon(4S)$ are boosted because of the asymmetric nature of the collider. The chamber has 8400 drift cells that are organized into six axial and five small-angle-stereo super layers[**?**]. Each drift cell contains one sense wires and eight field wires.

A low-Z gas is used to minimize the multiple coulomb scattering contributions to the momentum resolution. We use a 50% He 50% C_2H_6 gas mixture. The drift velocity of the electrons in the helium-ethane gas mixture is about 40 $\mu m/ns$. The distance to the track from the sense wire is determined using the time of a hit. Then a track segment finder selects the track positions belong to the same track and helix

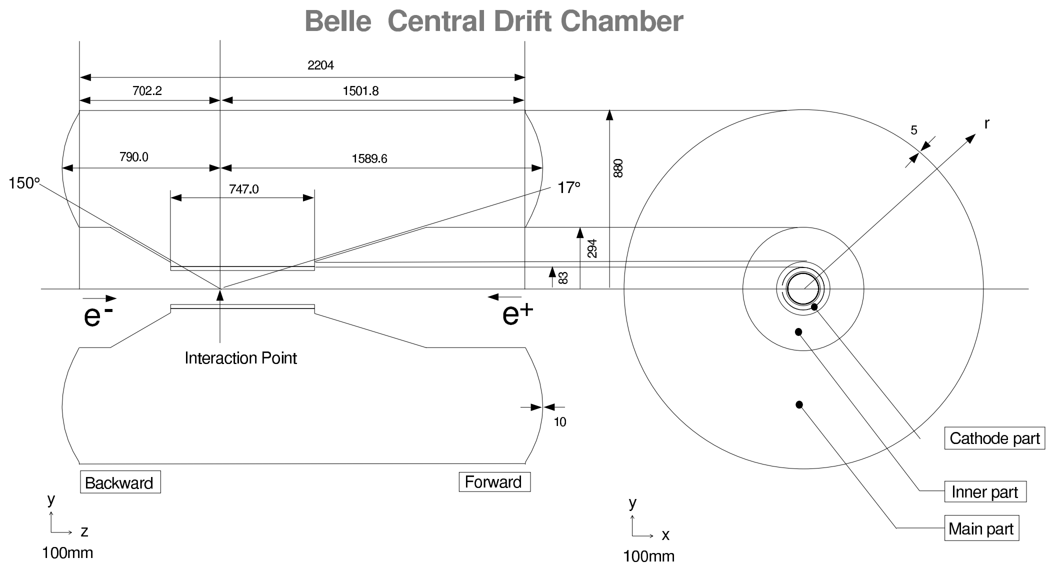

Figure 2.5: Overview of the Belle Central Drift Chamber (CDC). The lengths are in millimeters.

parameters are determined using this information. If SVD information is available for a given track, this information is also considered, determining the helix parameters. SVD information is useful for short lived particles and low momentum particles which decays inside the SVD.

The $r - \phi$ spatial resolution is about 130 μm and transverse momentum resolution is measured to be $(0.19 p_t \oplus 0.30)\% (p_t$ in GeV/c) using cosmic ray data.
Since dE/dx, energy loss by ionization is a function of velocity for a given incident particle, different particle species have different velocities for a given momentum. When the momentum, and dE/dx are known this information is sufficient to separate different particle species. The dE/dx measurements provides over 3σ separation

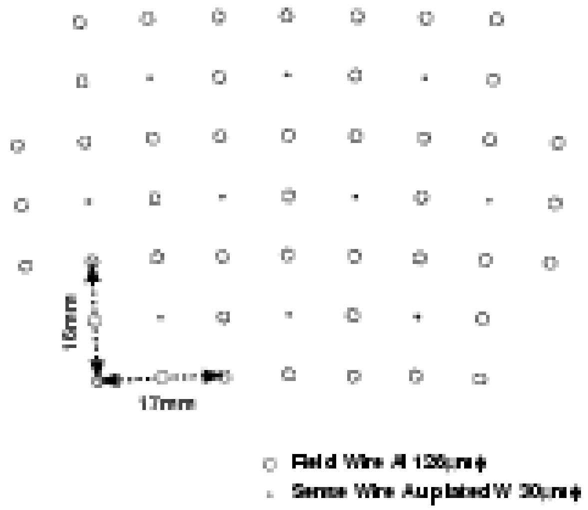

Figure 2.6: The cell structure of the CDC

between K and π for momenta below 0.8 GeV and 2σ separation for momenta above 2.0 GeV.

2.2.4 Aerogel Cerenkov Counter (ACC)

Aerogel Cerenkov Counter is an important part in the particle identification of the Belle detector. It can provide K/π separation in the momentum region up to 3.5 GeV/c, that is beyond the reach of CDC and ToF. The particle identification in the ACC is based on the Cerenkov effect. When a charged particle with velocity v travels in a medium with refractive index n, excited atoms in the vicinity of the particle become polarized. If v is greater than the speed of light in the medium, part of the excitation radiation emitted at a characteristic angle (θ) to the direction of motion.

It can be shown that,

$$\cos(\theta) = \frac{1}{\beta n} \tag{2.1}$$

where $\beta = \sqrt{1 - \frac{v^2}{c^2}}$. Since $v > c/n$, $\beta n > 1$. So a measurement for θ is a direct measurement for the velocity. It is possible to use a suitable medium such as silica aerogel, to produce Cerenkov radiation for one type of particle and while other types of particles do not produce any Cerenkov radiation.

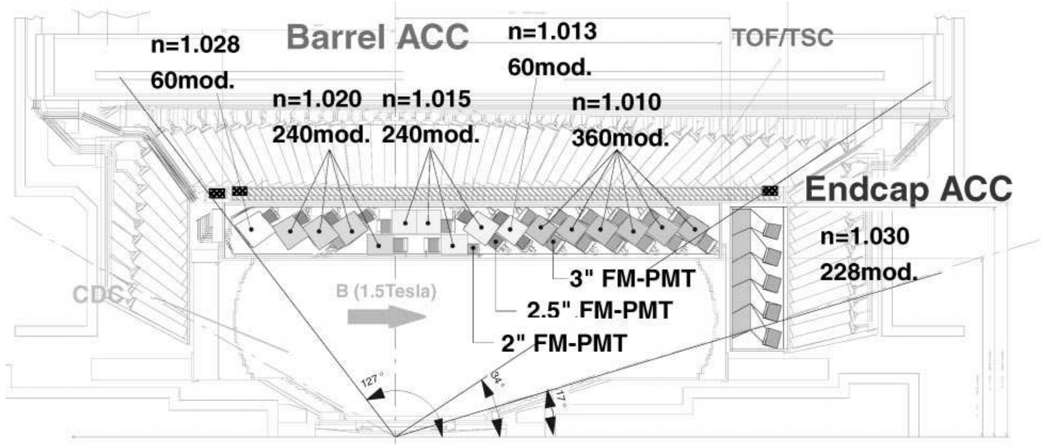

Figure 2.7: Schematic drawing of the BELLE-ACC system[?]

The refractive index of aerogel in the ACC is between 1.010 to 1.030. It contains 960 counter modules in the barrel region and 228 modules in the forward endcap region covering a range of polar angle 17^0 to 127^0. The Cerenkov radiation generated in the aerogel is fed to fine-mesh photo-multipliers (FM-PMTs), which can operate in the 1.5 T magnetic field. The advantage of a FM-PMT is large effective area and high gain[?].

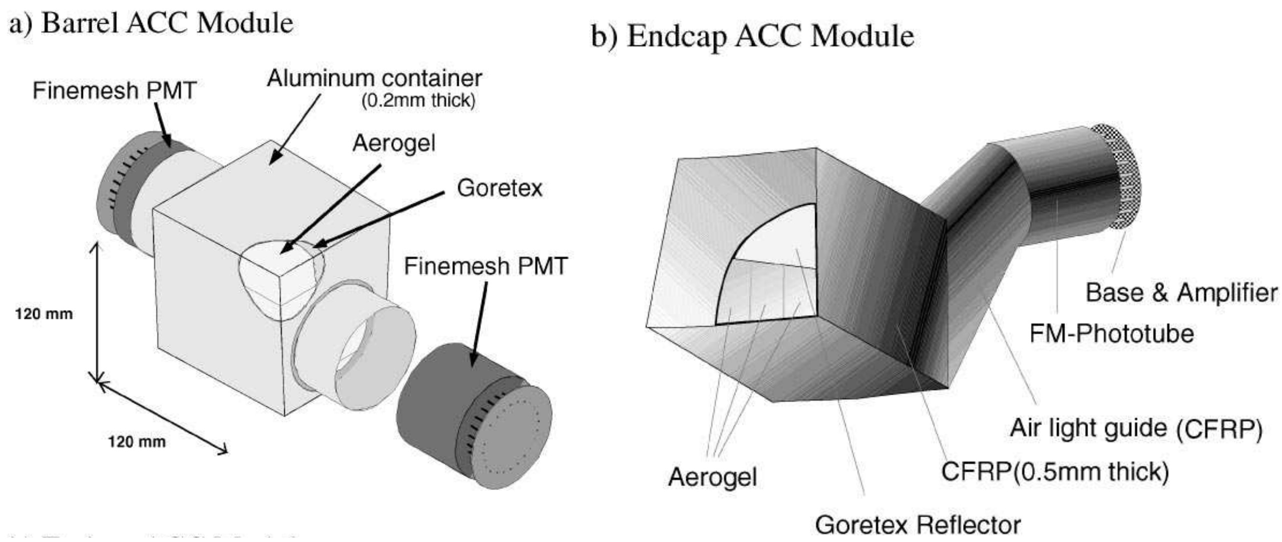

Figure 2.8: Schematic drawing of a typical ACC counter module, for the barrel ACC (left) and endcap ACC (right)[**?**].

2.2.5 Time of Flight System (ToF)

Time of flight counter uses flight time differences to identify particles. For a given flight length, flight time of a particle is different for different particles and dependent on the velocity of the particle. If the momenta of the particles are known, then the Time of Flight gives a measurement for the mass. This technique is used in the Belle time of Flight system which can effectively identify particles with momentum below 1.2 GeV/c[**?**]. For 1.2 m flight path, a ToF system with 100 ps time resolution is effective for 2σ $\pi^{\pm}/K^{\pm}$ separation for particle momentum below 1.2 GeV/c, which encompasses 90% of the particles produced in $\Upsilon(4S)$ decays. To achieve 100 ps design goal, fast scintillator with an attenuation length greater than 2.5 m are used. Phototubes with large area photocathodes are used to maximize the photon collection. The ToF system consists of 64 modules. Each module consists of two ToF counters with readout at both ends, and one thin Trigger Scintillation Counter (TSC). The acceptance of is $33^0 - 121^0$ in polar angle, and the minimum transverse momentum of a particle to reach the ToF counter is 0.28 GeV/c[?].

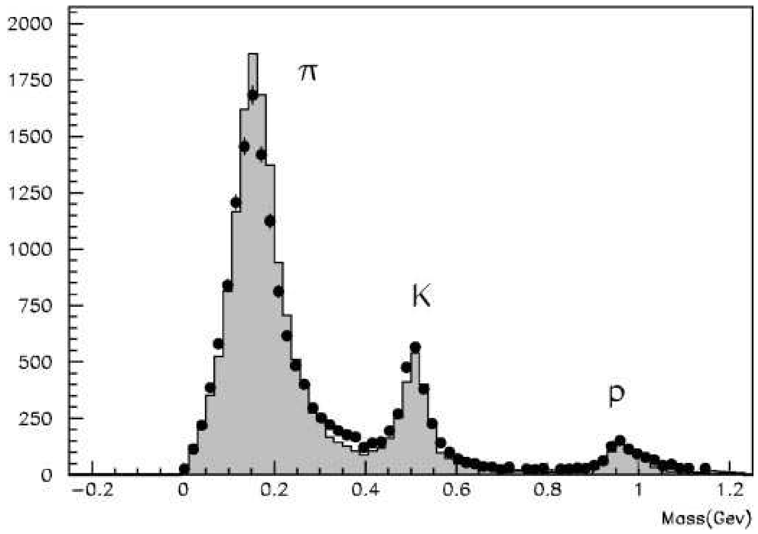

Figure 2.9: Mass distribution from ToF measurement for particle momentum below 1.2 GeV/c[?].

2.2.6 Electromagnetic Calorimeter (ECL)

The main purpose of the Belle CsI(Tl) calorimeter[?, ?] is to detect photons. Photons from B meson decays have relatively low energies. The reason is that most of the photons are end products of the decay cascades. To detect these photons, it is required to have a good performance below 500 MeV. Also some B decays such as $B \to K^*\gamma$ and $B \to \pi^0\pi^0$ produce photons with energies upto 4 GeV. Good resolution at high energies is required to reduce the background. This can be achieved by using highly segmented CsI crystals. In addition to photon detection, ECL can detect electrons which deposit energy in the calorimeter. Since electrons are associated with charged particle tracks, it can be identified separately. Belle CsI(Tl) calorimeter consists of 8736 CsI(Tl) counters. The barrel calorimeter, forward endcap calorimeter, and backward endcap calorimeter consist of 6624, 1152, and 960 counters respectively. Each CsI(Tl) crystal is 30 mm long and its cross section is 5.5 cm $\times$ 5.5 cm at the front face where the particles are entering. The coverage in the polar angle with respect to the electron beam axis is $12^0 < \theta < 155^0$ in the laboratory frame.

2.2.7 K-long Muon Detector (KLM)

The K_L/μ subsystem was designed to identify K_L's and muons with high efficiency over a broad momentum range which is greater than 600 MeV/c. The barrel region of the KLM covers an angular range from 45^0 to 125^0 in polar angle. The forward and backward endcaps extend the range from 20^0 to 155^0. The K_L/μ system consists of alternating layers of charged particle detectors and 4.7 cm thick iron plates. There are 15 detector layers and 14 iron layers in the barrel region, and 14 detector layers and 14 iron layers in each of the endcaps. K_L's interact in iron or in the ECL and produce a shower of ionizing particles. The location of the shower determines the direction of K_L. However the energy of K_L can not be measured due to large fluctuations in the size of the shower. The charged particle detection is provided by glass electrode resistive plate counters (RPSs). The multiple layers of charged particle detectors and iron allow discrimination between muons and charged hadrons based on the distance that they travel and the amount of scattering that occurs. Weakly interacting muons travel significantly faster with smaller deflections on average than strongly interacting hadrons.

2.2.8 Extreme Forward Calorimeter (EFC)

Extreme forward calorimeter is designed to extend the Belle detecting angle from $17^0 \sim 150^0$ to $6.4^0 \sim 171.4^0$ in the lab frame. It gives the instantaneous luminosity. The EFC is made of BGO ($Bi_4Ge_3O_12$) crystals which are tolerant to very high radiation. It also acts as a beam monitor for the KEKB control.

2.2.9 Super Conducting Magnet

The magnet provides an axial magnetic field about 1.5 Tesla over the tracking volume of the Belle detector. The field produced by the coil is returned by the steel plates used in the KLM detector. The nominal current to the coil is 4000 A.

2.2.10 Trigger and Data Acquisition

The purpose of the trigger system is select good events and reject background events as efficient as possible. At the design luminosity ($10^{34} cm^{-2} s^{-1}$) the trigger rate is expected to be at 100 Hz. Due to high beam current, high beam background is also expected. The expected trigger rate for the beam background is also expected to be around 100 Hz. Therefore the total trigger system is designed to keep the total rate below 200 Hz. The Belle trigger system consist of a Level-1 (L1) hardware trigger and a Level-3 (L3) software trigger. Belle Level-1 trigger system consists of two parts. One is the trigger systems of individual components of the Belle detector.

The other one is the central trigger system called the Global Design Logic (GDL). The sub-detector trigger system is based on two categories; track triggers and and energy triggers. The CDC and TOF are used to provide the trigger signals from charged particles. The ECL trigger system provides triggers based on total energy deposit and cluster counting of crystal hits. KLM trigger provides information about muons. Bhabhas ($e^+e^- \to e^-e^+ \ (+n\gamma)$) and two photon events are tagged by EFC trigger. All the event signals are processed parallaly by the sub-detectors and provide the trigger information to the GDL. Finally the event type is characterized by the GDL. The Level-3 (L3) trigger perform a simple reconstruction of the event to filter junk events. This helps to reduce the size of the data sample and reduce the space required to store data. The exact conditions of the trigger changes with each due to operating conditions. Trigger rate correlate with the beam currents, luminosity, and background level. It has been seen that the trigger rate gradually increased with the increase of the luminosity.

The data acquisition system (DAQ) of the Belle experiment was designed to operate with the trigger rate up to 500 Hz. The data size of a typical event is 30 kB. The components of the DAQ system are detector readout systems, an event builder, an online computer farm, and a data storage system. The detector readout systems read signals from the sub detectors and pass them to the event builder, which construct a complete event. The data from the event builder transferred to the online computer farm, and pass through L3 trigger. The online computer farm format the event data

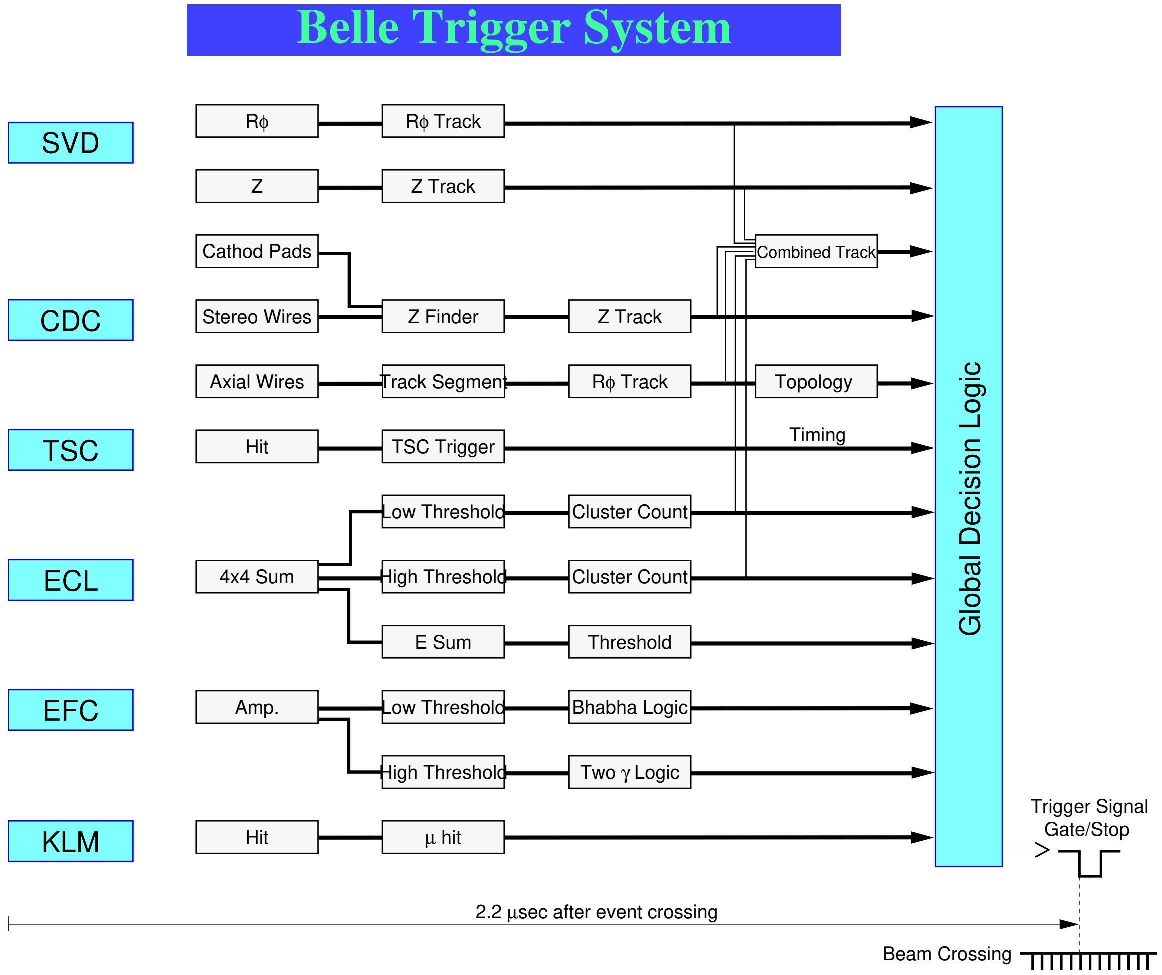

Figure 2.10: Belle trigger system

in to an offline event format and to monitor the data quality with sampled events. The monitoring data is being done by the online Data Quality Monitor (DQM). Then the data is sent to the storage system.

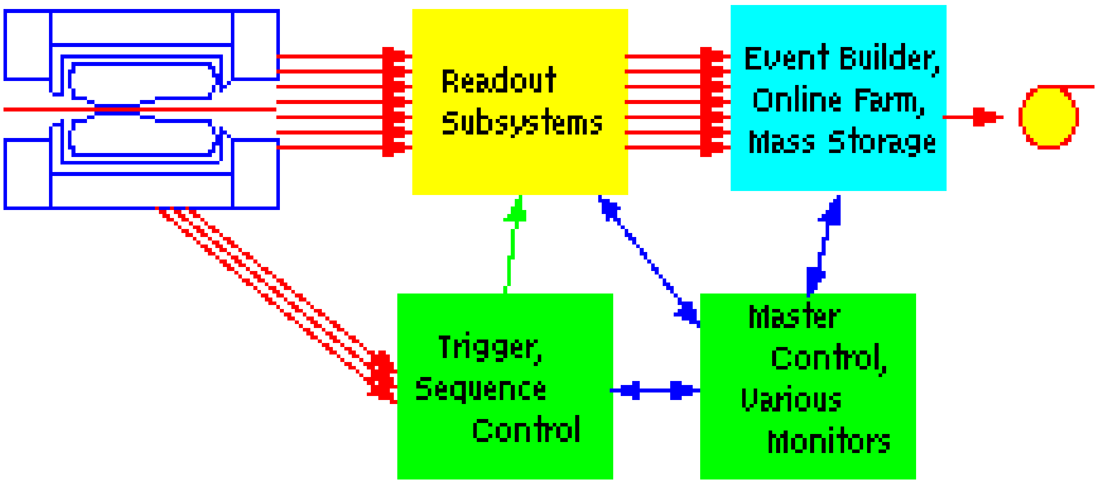

Figure 2.11: Belle DAQ system

Chapter 3

Exclusive two body Decays of B into $D_s^* h$

In this chapter, B decays to $D_s^{*+}\pi^0$, $D_s^{*+}\pi^-$ and $D_s^{*-}K^+$ are discussed. Charged B mesons consist of $b\bar{u}$ or $\bar{b}u$ quark combinations. Neutral B mesons consist of $b\bar{d}$ or $\bar{b}d$ quark combinations. The quark combination in D_s^* and D_s is $c\bar{s}$ or $\bar{c}s$ depending on their charge. None of these decays have been observed experimentally. Pion decay modes and Kaon decay mode can be used to study two different physics goals. One is the precise determination of the CKM matrix element V_{ub}. The other is to study the final state re-scattering effect[?][?].

3.1 Measuring $|V_{ub}|$

Since $B^0 \to D_s^{*+}\pi^-$ and $B^+ \to D_s^{*+}\pi^0$ decays expect to dominate by a $b \to u$ transition, it can in principle, provide the opportunity to determine $|V_{ub}|$, where $|V_{ub}|$ is the so called Cabbibo-Kobayashi-Maskawa matrix element. Current measurements for V_{ub} using $B \to X_u l\nu$ and $B \to \pi l\nu$ depend on phenomenological models[?] [?].

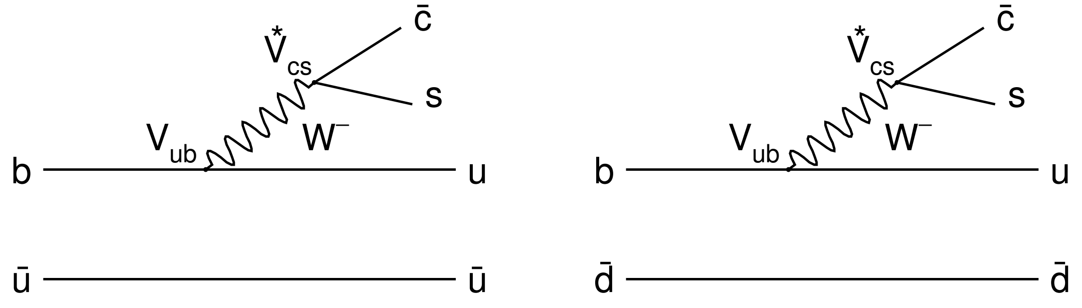

Figure 3.1: Decay diagrams of $B^- \to D_s^{*-}\pi^0$(left) and $B^- \to D_s^{*-}\pi^+$(right). $\bar{c}$ and s quarks form the D_s^{*-} meson. $u\bar{u}$ and $u\bar{d}$ form π^0 and π^+ mesons respectively.

Where l denotes for leptons and X_u denotes for hadrons consisting an up quark. So there is a need for more reliable measurement. $B^0 \to D_s^{*+}\pi^-$ and $B^+ \to D_s^{*+}\pi^0$ decays take place via a graph that has no charm quark, color suppressed tree, penguin or exchange graph. Therefore $D_s^{*+}\pi^0/\pi^-$ provide an opportunity for a clean measurement for $|V_{ub}|$. There are several theoretical predictions, using different approaches to extract $|V_{ub}|$. A. Deandrea et al.[?], obtained the decay rate based on the factorization approximation.

$$\Gamma(\bar{B} \to D_s^{*-}\pi^+) = 5.1 a_1^2 |V_{ub}V_{cs}^*|^2 10^{12} s^{-1} \tag{3.1}$$

where $a_1 = c_1 + c_2/N$ and c_1 and c_2 are known as Wilson coefficients. N is the number of colors. From the calculations done by D. Choudhury et al.[?], have obtained the following results.

$$\Gamma(\bar{B} \to D_s^{*-}\pi^+) = 0.34 |V_{ub}/V_{cb}|^2 [C_1'(m_b)]^2 10^{10} s^{-1} \tag{3.2}$$

$$\Gamma(B^- \to D_s^{*-}\pi^0) = 0.17 |V_{ub}/V_{cb}|^2 [C_1'(m_b)]^2 10^{10} s^{-1} \tag{3.3}$$

Here the notation is different but C_1' is as same as a_1. Also in this approach, factorization approximation was used to calculate the matrix elements of the interaction Hamiltonian between the initial state B meson and the two final state mesons. They have also shown that, rates of the modes such as $\bar{B}^0 \to D^+K^-$, $\bar{B}^0 \to D^+K^{*-}$, $\bar{B}^0 \to D^{*+}K^-$ and, $\bar{B}^0 \to D^{*+}K^{*-}$ are all proportional to C_1^2. So that the ratio of the rates of $\bar{B} \to D_s^{*-}\pi^+$) and any of the above mentioned modes, is independent of C_1'.

$$\frac{\Gamma(B^- \to D_s^{*-}\pi^+)}{\Gamma(B^- \to D^+K^-)} \propto |V_{ub}/V_{cb}V_{us}^*|^2 \tag{3.4}$$

Therefore this ratio is independent of the uncertainty of the effective value of N and the precise numerical values of the Wilson coefficients. The current values for the branching fractions (Br) are as follows[?].

$$Br(B^+ \to D_s^{*+}\pi^0) < 3.3 \times 10^{-4} \text{ at } 90~\%~\text{C.L.} \tag{3.5}$$

$$Br(B^+ \to D_s^{*+}\pi^-) < 4.1 \times 10^{-5} \text{ at } 90~\%~\text{C.L.} \tag{3.6}$$

3.2 Measuring $\sin(2\beta + \gamma)$

It is important to know the angles of the CKM [?] [?] unitarity triangle, to accept or refute the standard model. Non zero area of the triangle implies CP violation. Another important question is that, whether the sum of the three angles is 180^0. If it is not 180^0 that gives evidence for new physics. One of the proposed method to measure the angles of the unitarity triangle is, to measure $\sin(2\beta + \gamma)$ using the time

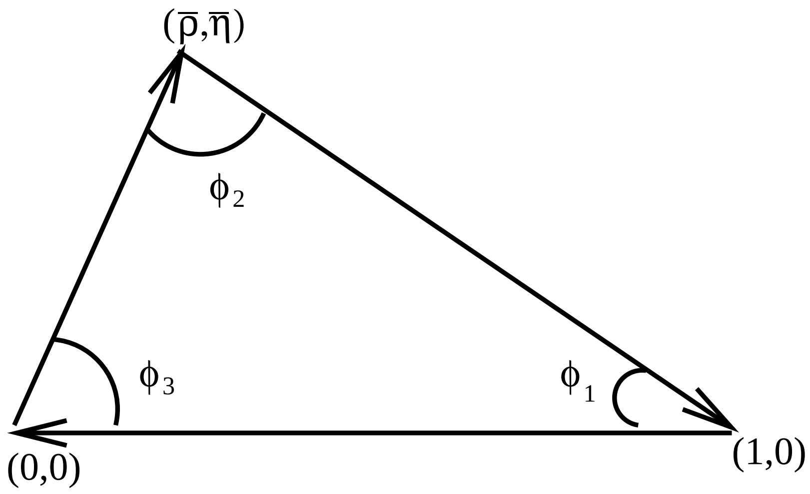

Figure 3.2: Unitarity triangle with vertices at (0,0), (0,1) and ($\overline{\rho}$,$\overline{\eta}$). $\overline{\rho}$ and $\overline{\eta}$ are $\rho(1-\lambda^2/2)$ and $\eta(1-\lambda^2/2)$ respectively in the Wolfenstein parameterization[**?**]

evolution of $B^0 \to D^{(*)+}\pi^-$ and $\bar{B}^0 \to D^{(*)-}\pi^+$ decays [**?**]. The ratio amplitudes is defined by[**?**],

$$R_{D^*\pi} \equiv \frac{|A(B^0 \to D^{*+}\pi^-)|}{|A(B^0 \to D^{*-}\pi^+)|} \equiv \frac{|A(\bar{B}^0 \to D^{*-}\pi^+)|}{|A(\bar{B}^0 \to D^{*+}\pi^-)|} \tag{3.7}$$

$R_{D^*\pi}$ is expected to be very small, ~ 0.02. within the standard model the decay rates of $B^0(\bar{B}^0) \to D^{(*)+}\pi^-$ and $\bar{B}^0 \to D^{(*)-}\pi^+$ can be given by,

$$\Gamma_{B^0\to D^{*+}\pi^-} = \frac{1}{8\tau_{B^0}} e^{-|\Delta t|/\tau_{B^0}}[1 - \cos(\Delta M\Delta t) - S_+\sin(\Delta M\Delta t)] \tag{3.8}$$

$$\Gamma_{B^0\to D^{*-}\pi^+} = \frac{1}{8\tau_{B^0}} e^{-|\Delta t|/\tau_{B^0}}[1 + \cos(\Delta M\Delta t) - S_-\sin(\Delta M\Delta t)] \tag{3.9}$$

$$\Gamma_{\bar{B}^0 \to D^{*+}\pi^-} = \frac{1}{8\tau_{B^0}} e^{-|\Delta t|/\tau_{B^0}} [1 + \cos(\Delta M \Delta t) + S_+ \sin(\Delta M \Delta t)] \tag{3.10}$$

$$\Gamma_{\bar{B}^0 \to D^{*-}\pi^+} = \frac{1}{8\tau_{B^0}} e^{-|\Delta t|/\tau_{B^0}} [1 - \cos(\Delta M \Delta t) + S_- \sin(\Delta M \Delta t)] \tag{3.11}$$

where Δt is the difference between the time of decay of the B meson and the time at which its flavor is tagged (as either B or $\bar{B}$), τ_B is the lifetime of the neutral B meson and ΔM is the mass difference in the $B^0 - \bar{B}^0$ system. The parameters $S_\pm$ are given by[**?**],

$$S_\pm = -2R_{D^*\pi} \sin(2\phi_1 + \phi_3 \pm \delta_{D^*\pi}) \tag{3.12}$$

Measuring $S_\pm$ and $R_{D^*\pi}$ enables us to calculate the angle $\sin(2\phi_1 + \phi_3)$. It is very important to obtain accurate value of $R_{D^*\pi}$. However current data sample may be too small to obtain the value $\frac{|A(B^0 \to D^{*+}\pi^-)|}{|A(B^0 \to D^{*-}\pi^+)|}$. It is very difficult to distinguish $B^0 \to D^{*+}\pi^-$ and $\bar{B}^0 \to D^{*+}\pi^-$, where the latter appear as background in the former. To overcome this problem, BaBar collaboration proposed a different technique to measure $R_{D^*\pi}$[**?**]. In the proposed method,

$$R_{D^*\pi} = \tan\theta_C \sqrt{\frac{Br(B^0 \to D_S^{(*)+}\pi^-)}{Br(B^0 \to D^{(*)-}\pi^+)}} \times \frac{f_{D^{(*)}}}{f_{D_s^{(*)}}}. \tag{3.13}$$

Where θ_C is the Cabibbo angle. $f_{D^{(*)}}$ and $f_{D_s^{(*)}}$ are known as decay constants[?]. The value of the required decay constant ratio is 1.10 ± 0.02[?].

Therefore branching fraction of $B^0 \to D_s^{(*)+}\pi^-$ is an important input for the measurement of $\sin(2\phi_1 + \phi_3)$.

3.3 $B^0 \to D_s^{*-}K^+$ Decay.

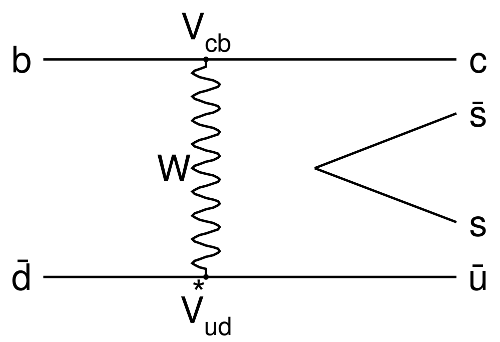

Figure 3.3: Decay diagram of $B^- \to D_s^{*+}K^-$. $\bar{c}$ and s quarks form the ${D_s}^{*-}$ meson. K^- meson is formed by s and $\bar{u}$ quarks.

The decay $B^0 \to D_s^{*-}K^+$ occurs via a W-exchange diagram, which has been first seen in $B^0 \to D_s^- K^+$ decay at Belle[?]. This decay can also provide information about final state re-scattering. It has been shown that $\bar{B}^0 \to D^+\pi^-(B^0 \to D^-\pi^+)$ can turn out to be $D_s^{*-}K^+(D_s^{*+}K^-)$ due to re-scattering effect[?]. If the branching fractions are smaller ($< 10^{-5}$), this means re-scattering does not play an important role. The current value for the branching fraction is[?],

$$Br(B^+ \to D_s^{*-}K^+) < 2.5 \times 10^{-5} \text{ at } 90\ \%\ \text{C.L.} \tag{3.14}$$

Chapter 4

Analysis

4.1 Introduction

The decays of $B \to D_s^* h$ are reconstructed in the modes $D_s^{*+}\pi^0$, $D_s^{*+}\pi^-$ and $D_s^{*-}K^+$. D_s^{*+} is reconstructed in the mode $D_s^{*+} \to D_s^+\gamma$. Three decay modes, $\{\phi \to K^+K^-\}\pi$, $\{\bar{K}^{*0} \to K^-\pi^+\}K^+$ and $\{K_S^0 \to \pi^+\pi^-\}K^+$ are used, in reconstructing D_s meson. In this section, event selection, skimming, candidate selection, background study, branching fractions, and systematic study are discussed.

4.2 Event Selection

The selection of the data sample, and event reconstruction procedure is explained in this section. First a hadronic data sample (see section 4.1.1) is selected from the data accumulated with the Belle detector. Then a sub set containing events for analysis is made. This data sample containing $B \to D_s^* h$ decays is called the 'skim'. Finally this skim is used to reconstruct B meson candidates using final state particles.

4.2.1 Hadronic Data Sample

At Belle, B mesons are produced in e^+e^- collisions, where $e^+e^- \rightarrow \Upsilon(4S) \rightarrow B\bar{B}$ at a center of mass energy of $\sqrt{s} = 10.58$ GeV. In addition Belle collects 10% of its data at 60 MeV below the $\Upsilon(4S)$ resonance, and the off-resonance data is useful for the studying of the continuum backgrounds which are produced by $e^+e^- \rightarrow q\bar{q}$ process. e^+e^- collisions produce events through several other processes such as τ pair, Bhabha, $q\bar{q}$ ($q = u, d, s, c$) and two-photon events. First Hadronic events are separated from those other processes. The selection procedure can be found at [**?**]. This sample known as Hadron-B skim, contains mainly $B\bar{B}$ and $q\bar{q}$ events, with cross sections 1.09 nb, and 2.62 nb respectively.

Belle started to collect data in the summer of 1999. By the end of November 2004, Belle had collected about $330 fb^{-1}$ of data. This data sample consists of sixteen separate run periods which are known as "experiments". Belle uses odd numbers for physics runs, starting from experiment-7, experiment-9, ...experiment-39. Experiment-5 and below are not used for analysis. Also there is no experiment-29. No. of $B\bar{B}$ events (in millions), in each experiment can be summarized as follows.

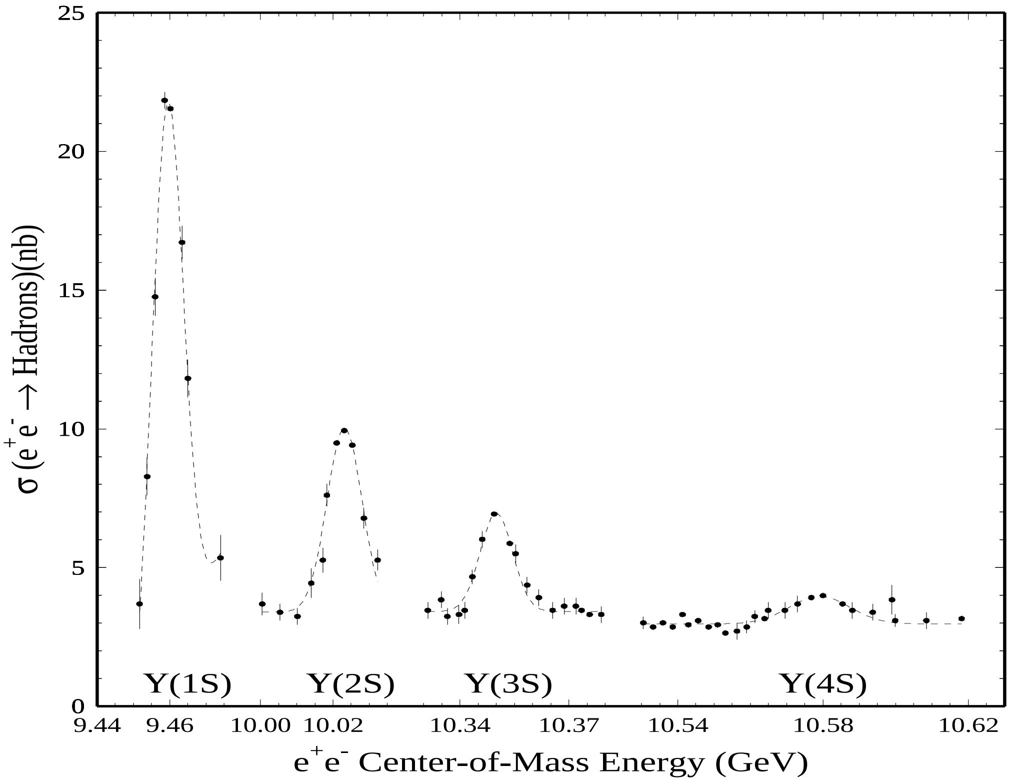

Figure 4.1: The Hadronic cross-section for e^+e^- annihilation measured by CLEO and CUSB showing the $\Upsilon(4S)$ resonances[?]

exp-7	6.46 ± 0.16	exp-23	6.48 ± 0.10
exp-9	$4.76\pm^{0.03}_{0.04}$	exp-25	$28.00\pm^{0.34}_{0.38}$
exp-11	8.85 ± 0.05	exp-27	$28.18\pm^{0.21}_{0.36}$
exp-13	11.70 ± 0.20	exp-31	19.89 ± 0.31
exp-15	13.57 ± 0.10	exp-33	18.35 ± 0.29
exp-17	12.46 ± 0.33	exp-35	17.39 ± 0.27
exp-19	27.17 ± 0.17	exp-37	67.18 ± 1.03
exp-21	4.34 ± 0.07	exp-39	not available yet

Total Hadron-B Data sample contains $(274.75 \pm 3.06) \times 10^6$ $B\bar{B}$ events (experiment 39 is not included).

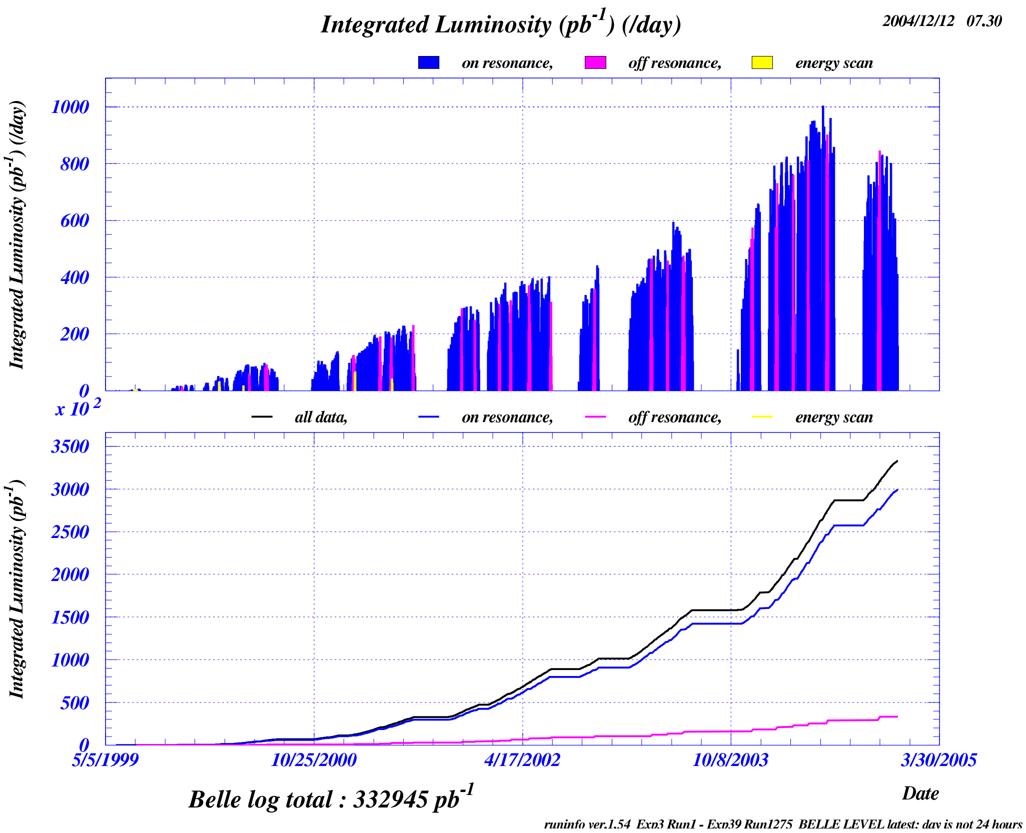

Figure 4.2: Integrated luminosity per day (top) and total integrated luminosity (bottom) as of 12^{th} December, 2004.

4.2.2 Monte Carlo Data

Monte Carlo simulations are done mainly in two parts, event generation, and detector simulation. Monte Carlo events are generated using two generators 'qq' and 'evtgen' [?][?]. Detector simulation is done by a Belle (GSIM) program. The generator programs simulate the physics of the collision and subsequent decays. The user can adjust the decay table which defines the interactions and subsequent decays. A standard decay table is used for mass scale Monte Carlo event generation. The GSIM program which simulate the detector acceptance, accepts parameters such as interaction position, tracking parameters and background information. GSIM is a GEANT which simulates the passage of elementary particles through the matter, based program. Since the experimental conditions are different for different experiments, Monte Carlo data are also generated as separate experiments. Generic Monte Carlo events are separated into four physics categories; charged (charged B decays), charm ($e^+e^- \to c\bar{c}$), uds ($e^+e^- \to u\bar{u},\ d\bar{d},\ s\bar{s}$), and mixed (neutral B decays). Charged MC is used to study charged B meson decays. Neutral MC events are used to study neutral $B\bar{B}$ decays. Charm Monte Carlo contain continuum events that decays to particles with charm quarks. Other possible continuum events are generated as uds. In addition to generic Monte Carlo events, tau and two-photon Monte Carlo events are also generated. Signal Monte Carlo events required for analyses are generated with user defined decay tables.

4.2.3 Flavor tagging

The process to determine the flavor of the B^0 meson is called flavor tagging. It is required to distinguish B^0 from $\bar{B}^0$ for CP violation measurements. B mesons are generated as a pair of B^0 and $\bar{B}^0$ from $\Upsilon(4S)$. This pair is produced in a coherent state and remains coherent until one of them decays. When one of them decays to a CP eigenstate, this B (i.e. $B^0 or \bar{B}^0$) is fully reconstructed. The other B (i.e. $\bar{B}^0 or B^0$)

which consists of all the tracks and energy clusters not used to reconstruct the CP mode are known as 'tag side B' and decay products of this B is used for tagging. Therefore this method is known as 'opposite-side tagging'. The first one to decay can be either 'tag side B' or 'the CP side B', and this only changes the sign of the proper time difference of the two B meson decays.

Leptons and kaons provide good tools for the tagging of the opposite side B meson. The charge of the leptons and kaons that come from the decays of the b-quark is related to the flavor of the B meson they came from. If the charge is $+1(-1)$, the flavor of the tag side B is $B^0(\bar{B}^0)$. Leptons and kaons from the other sources can cause wrong tagging. Also particles misidentified as kaons or leptons can affect the accuracy of the tagging. Wrong tagging dilutes the measured CP asymmetry and one of the sources of the systematic errors. When a fraction of B^0 assigned as $\bar{B}^0$ and a fraction of $\bar{B}^0$ assigned as a B^0 the net difference between number of B^0 and $\bar{B}^0$ reduces by a factor of $1-w$, where w is known as the 'wrong tag fraction'. Therefore, it is important to estimate the wrong tag fraction (w). Two variables 'q' and 'r' are obtained from the tagging process.

$$q = +1 \text{ (for } B^0) \tag{4.1}$$

$$= -1 \text{ (for } \bar{B}^0) \tag{4.2}$$

$$r = 1 - 2w \; (r \to 1, \text{ for good tagging}) \tag{4.3}$$

The value r is known as the dilution factor and provide a a measurement for the accuracy of the tagging. For a good tagging $r \sim 1$.

4.2.4 $B \to D_s^* h$ Skim

Hadron-B data are used to make a skim for the $B \to D_s^* h$ decays. The selection criteria for the skim were chosen very carefully to reduce as much background events as possible while retaining all the signal events and background for study. The advantage of making a skim is, whenever it is needed to re-run data, it is sufficient to run through the skim, which needs much less time and CPU power. However it requires additional space to save the skim. $B \to D_s^* h$ events are skimmed using the following selection criteria.

All charged tracks are selected with the requirement that their impact parameters, $|dr|$ and $|dz|$ be less than 1.0 cm and 3.0 cm, with respect to the interaction point respectively. Then they are saved assuming pions or kaons. Kaons are selected with a very loose Particle ID (PID-see Appendix A) requirement (> 0.002). Pions are selected without any PID requirement. Neutral pions are reconstructed by combining two photons with invariant mass between 117.8 MeV/c^2 and 150.2 MeV/c^2. Both photons must have energy greater than 50 MeV in the lab frame. Also the variance (χ^2) of the mass constrained fitting is required to be less than 30. Photon candidates are required to have energy greater than 30 MeV in the lab frame. K_S^0 candidates are reconstructed using two charged pions satisfying same Particle ID selection requirement mentioned above. In addition to that, two pions must have a common vertex with the variance (χ^2) of the vertex fitting is less than 50. The invariant mass of $\pi^+\pi^-$ combinations are required to be within 20 MeV/c^2 of the expected mass of K^0_S (497.672 ± 0.031 MeV/c^2 [?]). Two oppositely charged kaons are used to reconstruct the ϕ candidate, and the invariant mass of K^+K^- combinations are required to lie between 1.004 GeV/c^2 and 1.034 GeV/c^2. A charged kaon and an oppositely charged pion are combined to reconstruct the K^{*0} candidate. The invariant mass of the $K^-\pi^+$ combinations must be between 0.79166 GeV/c^2 and 0.99166 GeV/c^2. Then, D_s^+ candidates are reconstructed in the modes $D_s^+ \to \phi\pi^+$, $D_s^+ \to K^0_S K^+$, and $D_s^+ \to K^{*0}K^+$. D_s^+ candidate must lie within 100 MeV/c^2 of the nominal mass (1.9685 GeV/c^2)[?].

$D_s^{*+} \to D_s^+\gamma$ candidates are reconstructed by combining a photon with the D_s^+ candidate. The mass difference between $D_s^+\gamma$ and D_s^+ candidates is required to be within 43.8 MeV/c^2 and 243.8 MeV/c^2. Also the momentum of the D_s^{*+} candidate in the $\Upsilon(4S)$ center of mass frame must be less than 2.7 MeV/c. This selection reduces D_s^{*+} candidates produced by $e^+e^- \to q\bar{q}$ (where $q = u,\ d,\ c,\ and\ s$) processes. The B meson candidate is reconstructed by combining D_s^{*+} with a neutral pion, charged pion or a kaon. We use two variables in selecting the B candidate. One is the momentum of the B candidate and the other is the energy of the B candidate. KEKB accelerator produces B mesons from $\Upsilon(4S)$ decays, with mean momentum about 343 MeV/c in the $\Upsilon(4S)$ center of mass frame (CM). Therefore B meson candidates with momentum greater than 1 GeV/c in the $\Upsilon(4S)$ center of mass frame are rejected. In the $\Upsilon(4S)$ frame, the mean energy of the B candidate is equal to the beam energy ($E_b = 5.29$ GeV). To take advantage of this property, we define ΔE ($= E_{cm} - E_b$), which is the energy difference between B candidate energy and the beam energy. The selection requirement for the energy is $|\Delta E| < 0.3$ GeV. Any event containing a B candidate, which satisfy all the requirements, is saved in the skim. Monte Carlo data are also skimmed.

4.2.5 Selection of the B candidate

For this selection, skimmed data which contains events with B candidates are used. Although the B candidates passed through the skimming criteria it is required to use stricter selection criteria to reduce background while keeping as much the signal as possible. The cuts used for skimming are listed below.

	cut
tracks	$\lvert dr\rvert < 1.0$ cm; $\lvert dz\rvert < 3.0$ cm
K	$KID > 0.002$
γ	$E_{lab} > 30$ MeV
π^0	$117.8 < M(\gamma\gamma) < 150.2$ MeV/c^2; $E_{cm}(\gamma) > 50$ MeV
ϕ	$1.004 < M(K^+K^-) < 1.034$ GeV/c^2
K_S^0	$0.4776 < M(\pi^+\pi^-) < 0.5176$ GeV/c^2
K^{*0}	$0.7917 < M(K^-\pi^+) < 0.9917$ GeV/c^2
D_s^+	$1.8685 < M(\phi\pi^+),\ M(K_S^0K^+),\ M(K^{*0}K^+) < 2.0685$ GeV/c^2
D_s^{*+}	$43.8 < M(D_s^+\gamma) - M(D_s^+) < 243.8$ MeV/c^2; $P_{cm} < 2.7$ MeV/c
B	$P_{cm} < 1$ GeV/c; $\lvert\Delta E\rvert < 0.3$ GeV

All charged kaons and pions are required to have PID greater than 0.6 (see Appendix A).

Invariant masses of K^+K^-, $\pi^+\pi^-$, $K^+\pi^-$ pairs are required to satisfy $1.0116 < M(K^+K^-) < 1.0272$ GeV/c^2 (3σ), $0.4902 < M(\pi^+\pi^-) < 0.5051$ GeV/c^2 (3σ) and, $0.8263 < M(K^+\pi^-) < 0.9570$ GeV/c^2 (3σ) respectively. The invariant mass of the reconstructed D_s^+ candidate is required to be within 3σ of the expected mass. The width of the D_s^+ signal varies with its decay mode. For $D_s^+ \to \phi\pi^+$ mode, the selection requirement is $1.9539 < M(\phi\pi^+) < 1.9833$ GeV/c^2 ($\sigma \sim 4.9$ MeV/c^2). For the other two modes the selection requirement is $1.9471 < M(K_S^0K^+) < 1.9901$ GeV/c^2

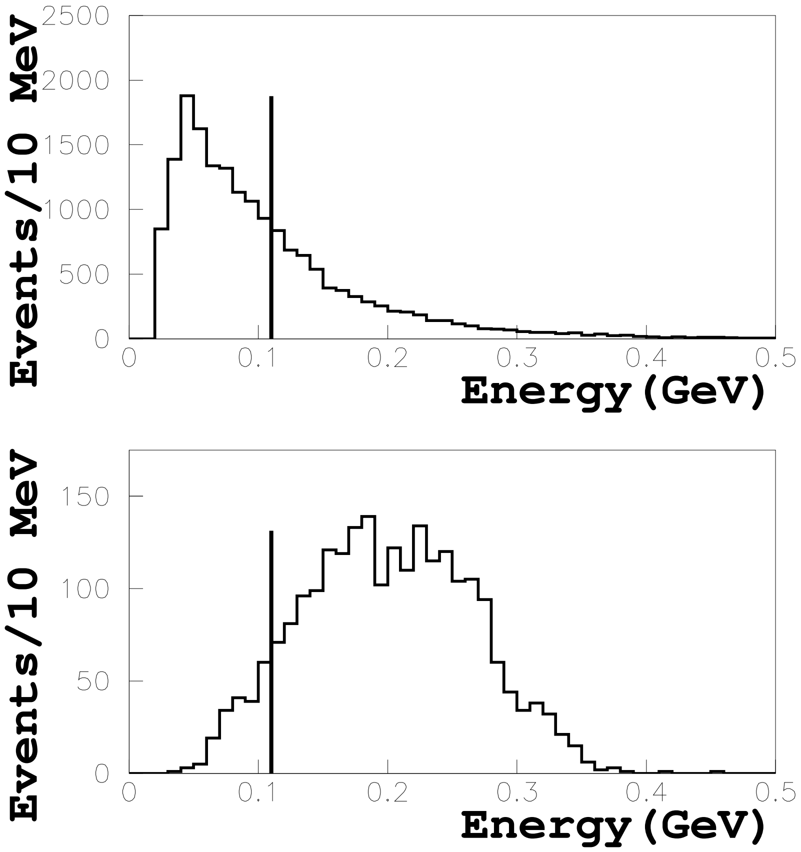

Figure 4.3: Photon energy spectrum (in the $\Upsilon(4S)$ CM frame) from fake (top) and real (bottom) $D_s^{*+} \rightarrow D_s^+\gamma$ decays. Both histograms were produced with signal Monte Carlo events. Vertical line shows the selection requirement.

($\sigma \sim 7.2$ MeV/c^2) and $1.9495 < M(\bar{K}^{*0}K^+) < 1.9877$ GeV/c^2 ($\sigma \sim 6.4$ MeV/c^2). Mass difference between D_s^{*+} candidate and D_s^+ candidate is required to be within three standard deviations ($0.124 < \Delta M < 0.164$ GeV/c^2) of the expectation. All photon candidates are selected with energy greater than 110 MeV in the $\Upsilon(4S)$ center of mass frame. Most of the photons that are not coming from the D_s^{*+} candidate populate the low energy region. Our requirement reduces 50% of the background while keeping 90% of the signal (Fig. 4.3). Possible B candidates are identified using their ΔE and $M(B)$, where

$$\Delta E = (\sum_i E_i) - E_b \tag{4.4}$$

$$M(B) = \sqrt{{E_b}^2 - (\Sigma_i \vec{p_i})^2} \tag{4.5}$$

E_b is the beam energy in the $\Upsilon(4S)$ resonance, and p_i is the momentum of the ith B candidate decay product in the center of mass frame of $\Upsilon(4S)$ resonance. E_i is the energy of the ith B candidate decay product in the $\Upsilon(4S)$ center of mass frame. For the ${D_s}^*\pi^0$ mode, ΔE is required to be between -0.1 and $+0.05$ GeV, and for the ${D_s}^*\pi/K$ modes, ΔE is required to be between -0.05 and $+0.05$ GeV. The reason for a wider ΔE requirement for the neutral pion mode is mainly due to the poorer resolution in the neutral pion energy. The beam constrained mass is required to lie between 5.27 and 5.29 GeV/c.

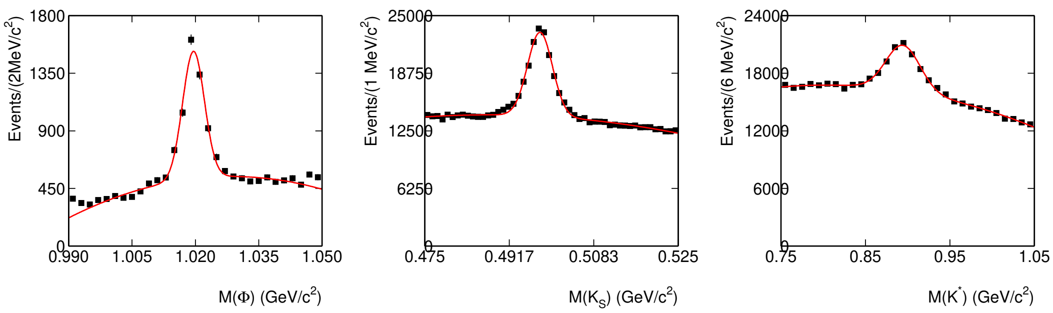

Figure 4.4: Invariant mass distributions of KK, $\pi\pi$ and Kπ respectively for real data

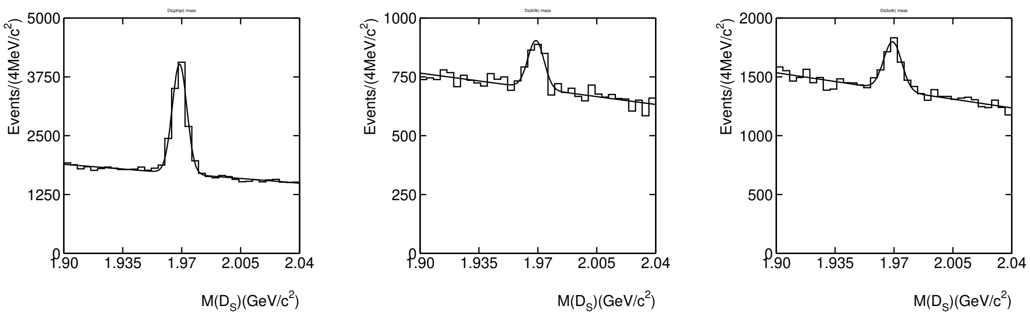

Figure 4.5: Invariant mass distributions of $\phi\pi$, $K_S^0 K$ and $K^{*0}K$ respectively for real data

4.3 Additional Background Suppression

The main source of the background for signal candidates is from $q\bar{q}$ (where $q = u,\ d,\ c,\ and,\ s$) events. Other B meson decays can also appear as background. Several variables used to suppress the background are discussed in this section.

4.3.1 Helicity Angle

Helicity is the component of spin in the direction of motion of a particle. When a spin 0 particle decays into a spin 1 and a spin 0 particles, helicity angle is used as a background reduction method. In the decay $D_s^+ \to \phi\pi^+$ ($\bar{K}^{*0}K^+$), ϕ ($\bar{K}^{*0}$) is spin 1 and π^+ (K^+) is spin 0. Helicity angle for the $\phi\pi$ ($\bar{K}^{*0}K$) mode is defined as the angle between the momentum of D_s^+ in ϕ ($\bar{K}^{*0}$) frame and the momentum of K in ϕ ($\bar{K}^{*0}$) frame. The absolute value of the cosine of the helicity angle is required to be greater than 0.3 (Fig. 4.6).

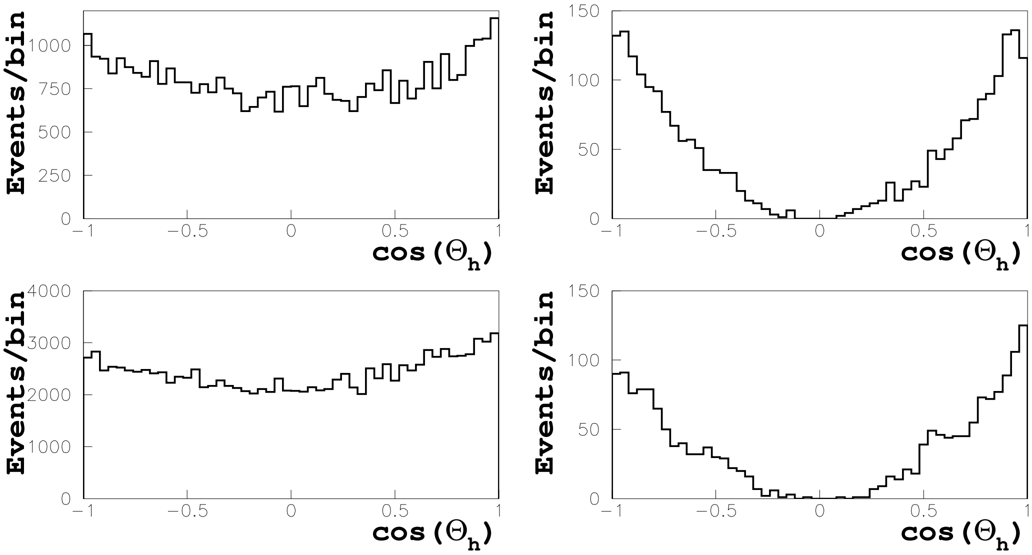

Figure 4.6: Distributions of cosine of the helicity angle. Top row is for $D_s^+ \to \phi\pi^+$ mode and the bottom row is for $D_s^+ \to \bar{K}^{*0}K^+$ mode. Left column plots are for generic Monte Carlo background events and right side column plots are for signal Monte Carlo events. Continuum events exhibit an almost flat distribution, while signal events have $\cos^2(\theta)$ distribution.

4.3.2 Fisher Discriminant

To suppress the background further we use the Fisher Discriminant technique[?]. The Fisher discriminant is a linear combination of nine variables with coefficients set to maximize the separation between signal and background. We define r_l, R_l, θ_{th}, $\cos(\theta_B)$, $(Q_{D_s} \times qr)$ as follows.

- $r_l = \frac{\Sigma_{i,j}|p_i||p_j|P_l(cos\Theta_{ij})}{\Sigma_{i,j}|p_i||p_j|}$, $l = 1, 2, 3, 4$;
- $R_l = \frac{\Sigma_i|p_i||p_h|P_l(cos\Theta_{ih})}{\Sigma_i|p_i||p_h|}$, $l = 2, 4$;

  i, j run through all photons and charged tracks. P_l is the Legendre polynomial of order l. Momenta of charged particles and photons are denoted by $|p_i|$, $|p_j|$

and $|p_h|$. Here h denotes either charged particles coming from B candidates or photons coming from neutral pions that are from B candidates.

- $\cos(\theta_{th})$, where θ_{th} is the thrust angle, the angle between the thrust axis ($\hat{T}$) [?] [?] of the B candidate and that of the remaining particles of the event. The quantity thrust is defined as,

$$T = \frac{\sum_i |\hat{T} \cdot p_i|}{\sum_i |p_i|} \tag{4.6}$$

  where the thrust axis $\hat{T}$ maximizes T. The absolute cosine value of θ_{th} is used.

- $\cos(\theta_B)$, where θ_B is the angle between the B candidate momentum in the $\Upsilon(4S)$ frame and the beam axis. The absolute value of this angle is used.

- $(-Q_{D_s} \times qr)$, which is the product of the charge of the D_s candidate (Q_{D_s}) and qr which is a parameter that contains the flavor information of the other B. q is either $+1$ or -1 depending on whether it is a B candidate or $\bar{B}$ candidate. r can take values only between 0 and 1. For a good flavor tagging q is close to 1.

All the nine variables are combined to form a Fisher discriminant [?] as follows.

$$\mathcal{F} = \sum_l \alpha_l r_l + \sum_l \beta_l R_l + \gamma_1 |\cos(\theta_{th})| + \gamma_2 |\cos(\theta_B)| + \gamma_3(-Q_{D_s} \times qr) \tag{4.7}$$

Then $\mathcal{F}$ is optimized by obtaining the values of the parameters α_l, β_l, γ_1, γ_2, and γ_3 such that it gives the maximum separation between background and signal. MC events are used for the optimization. Optimization is done with the requirements,

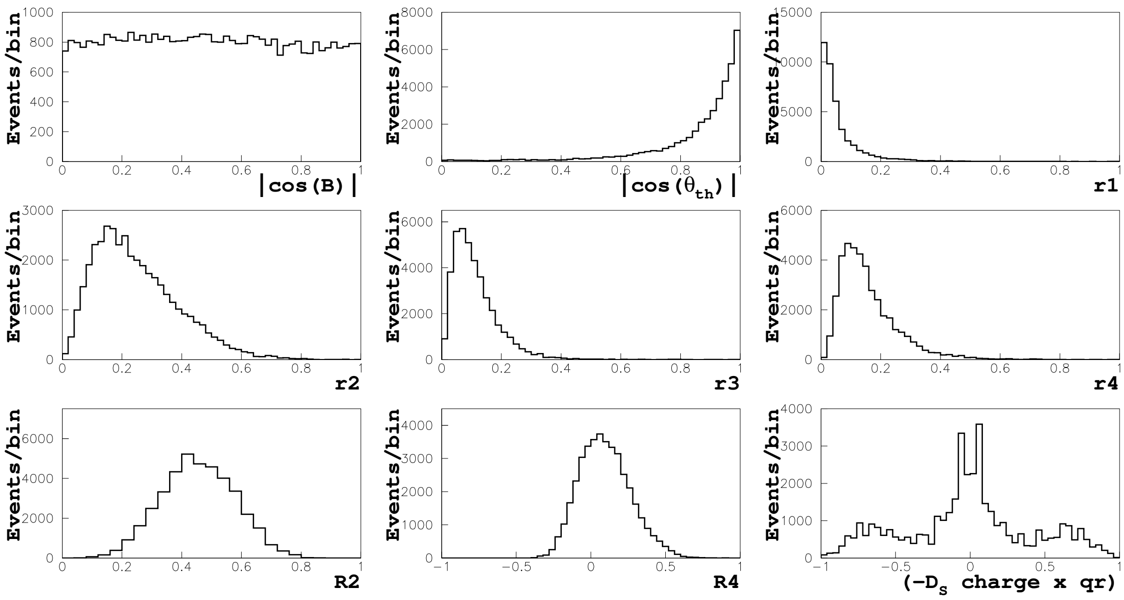

Figure 4.7: Distributions of the nine Fisher variables, for continuum Monte Carlo events. Top row: $|\cos(\delta)|$, $|\cos(\theta_{th})|$, and r_1. Middle row: r_2, r_3, and r_4. Bottom row: R_2, R_4, and $(-Q_{D_s} \times qr)$.

$1.007 < M(\phi) < 1.033$ GeV/c^2, $1.945 < M(D_s) < 1.985$ GeV/c^2, $0.124 < \Delta M < 0.164$ GeV/c^2, and D_s^{*+} momentum in the center of mass frame is between 1.7 and 2.5 GeV/c in the $\Upsilon(4S)$ center of mass frame. The cut value in $\mathcal{F}$ is determined by considering the Figure of Merit (FOM) value

$$FOM = \frac{Signal}{\sqrt{background}} \tag{4.8}$$

as a function of the cut in $\mathcal{F}$ (see Figure 4.9). The goal is to improve FOM without large efficiency reduction. Selected cut values are indicated by dotted lines in Figure 4.9. Table 4.1 shows the Fisher requirements for each decay mode.

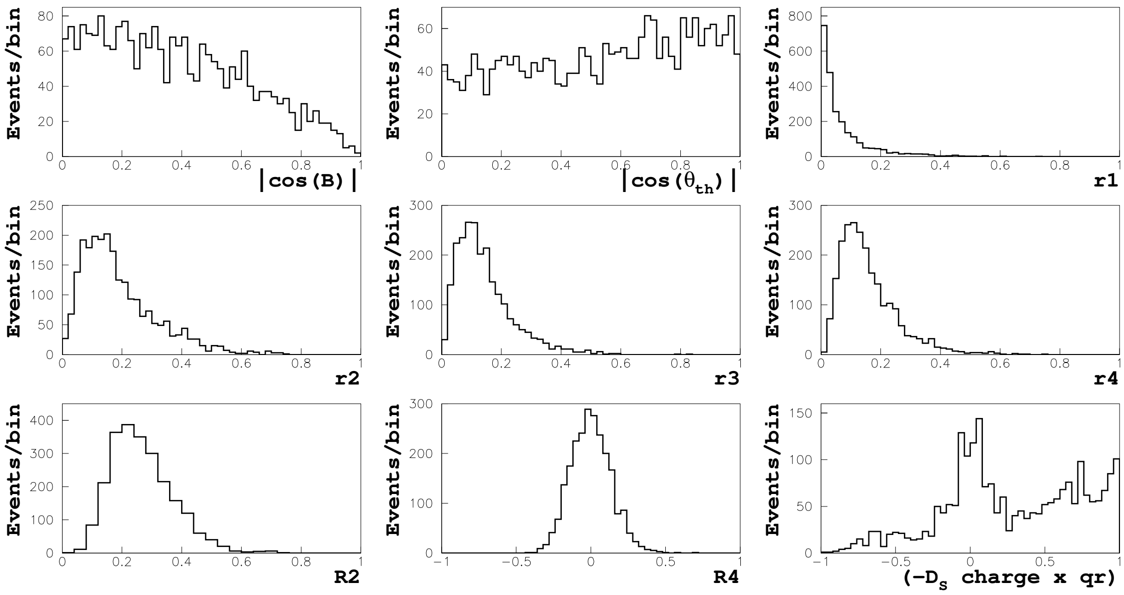

Figure 4.8: Distributions of the nine Fisher variables, for signal Monte Carlo events. Top row: $|\cos(\delta)|$, $|\cos(\theta_{th})|$, and r_1. Middle row: r_2, r_3, and r_4. Bottom row: R_2, R_4, and $(-Q_{D_s} \times qr)$.

Analysis Mode	$D_s \to \phi\pi$	$D_s \to K_S K$	$D_s \to K^* K$
${D_s}^{*-}\pi^0$	-1.0	-1.0	-1.0
${D_s}^{*-}\pi^+$	-1.5	-1.0	-1.0
${D_s}^{*+}K^-$	-1.0	-1.5	-1.0

Table 4.1: Fisher Requirements for different decay modes

4.3.3 π^0 Veto

Photons can be produced in many processes. But in this analysis, the only interest is in the photons from $D_s^{*+} \to D_s^+\gamma$ processes. One of the main processes, that produce unwanted photons is $\pi^0 \to \gamma\gamma$. If a photon candidate when combined with any other photon in the event, has invariant mass between 120 MeV/c^2 and 150 MeV/c^2, it is

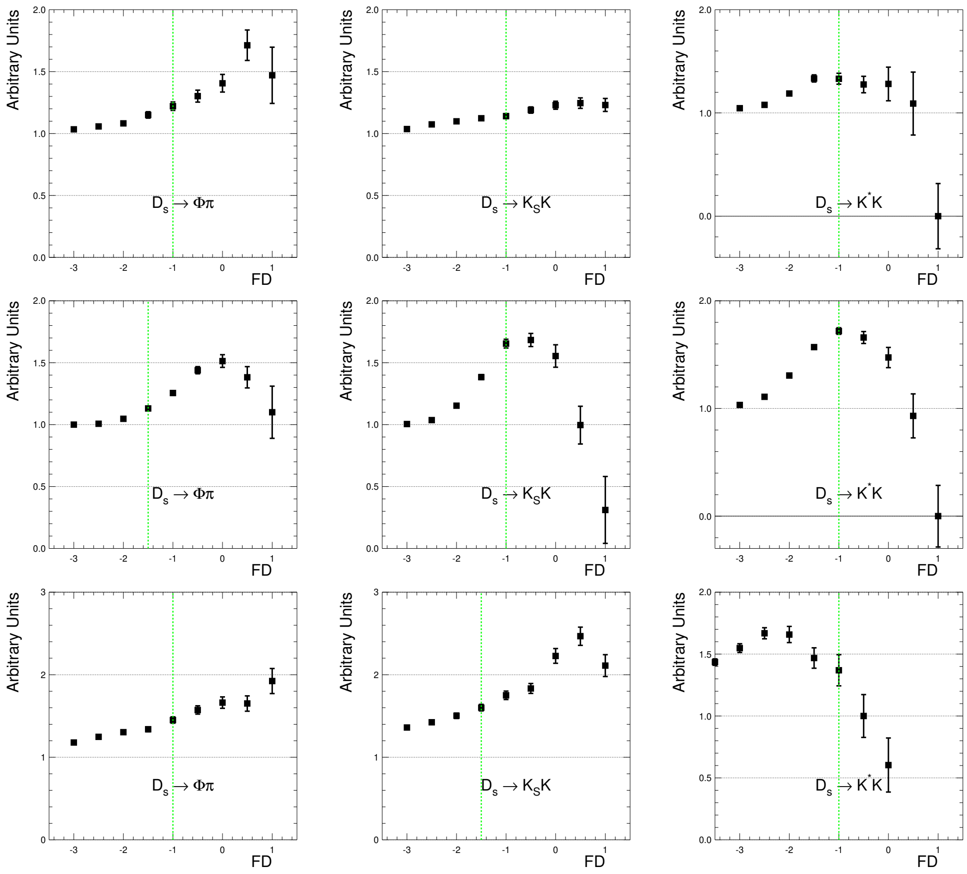

Figure 4.9: Figure of Merit (FOM) against FD. Top row is for $B^+ \to D_s^{*+}\pi^0$, middle row is for $B^0 \to D_s^{*+}\pi^-$, and the bottom row is for $B^0 \to D_s^{*-}K^+$ mode. From left to right, D_s^+ decay modes $\phi\pi$ $K_S^0 K$ and $K^{*0}K$ are shown. Cut values are indicated by the dotted lines.

rejected. The efficiency of this π^0 veto is $\sim 58\%$. About 70% of the background in ΔM can be reduced by this selection.

4.4 Estimation of the Backgrounds

To estimate possible signal, it is necessary to estimate the backgrounds, which satisfy all the selection requirements and appear in the signal region. The background can be divided into two categories. One is non-peaking background. The other is the peaking background. Non-peaking background mainly consists of continuum events. The main source of the peaking background is from B meson decays.

4.4.1 Monte Carlo Model

Non Peaking backgrounds

Simulated generic background (from $q\bar{q}$ and most of the $B\bar{B}$ decay channels) shapes of beam constrained mass were fit with the parametrized empirical background function(also known as the Argus function) given by[**?**],

$$dN/dM(B) = M(B)\sqrt{1-(M(B)/E_b)^2} \times e^{-a(1-(M(B)/E_b)^2)}. \tag{4.9}$$

Where a is a free parameter. E_b is the beam energy. Also all the requirements on masses and ΔM are relaxed to 4.5σ of their expected values. In addition to those requirements ΔE and $M(B)$ requirements are used. For the background determination, no requirement on $\mathcal{F}$ is imposed. There is no significant effect on the background shape by the Fisher Discriminant requirement. To prove this, we studied the background shapes of upper 50% and lower 50% of the distribution in $\mathcal{F}$ (figure 4.10), and found no significant difference in the shape between them. Both upper and lower 50% of the distribution of $\mathcal{F}$ are fitted with the parametrized empirical background function with the same fitting parameters.

Then we use the fitted shape to fit the background in the data excluding the signal region. The signal region is defined as $5.27 < M(B) < 5.29$ GeV/c^2 and

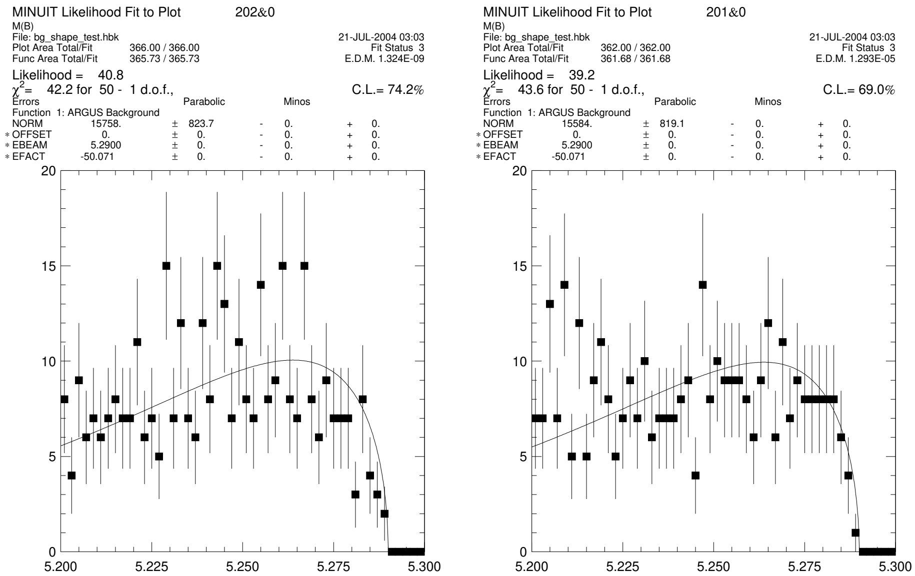

Figure 4.10: Generic MC Background shape in M(B), for the lower (right) and upper (left) 50% of the Fisher Distribution. Both plots were fitted with the same fit parameters. These plots were made for $B^0 \to D_s^{*-} K^+$ mode with $D_s^+ \to \phi\pi^+$.

$-0.1 < \Delta E < 0.05$ GeV for $D_s^{*+}\pi^0$ mode. For the other two modes, the signal region is defined as $5.27 < M(B) < 5.29$ GeV/c^2 and $-0.05 < \Delta E < 0.05$ GeV. Background is estimated by extrapolating the background shape into the signal region.

Peaking Backgrounds

Some B meson decay modes can peak in the signal region when the candidates consist of all or nearly all of the final state particles. Even with a missing low energy neutral pion or a photon, and/or a misidentified hadron, there can be a peak very close to the signal. We shall call these modes "peaking modes'. The modes $D^{*+}\pi^0$, $D^{*+}\pi^-$, $D^{*+}K^-$ and, $D^+\rho^-$ were studied. There are also other modes, but their contribution

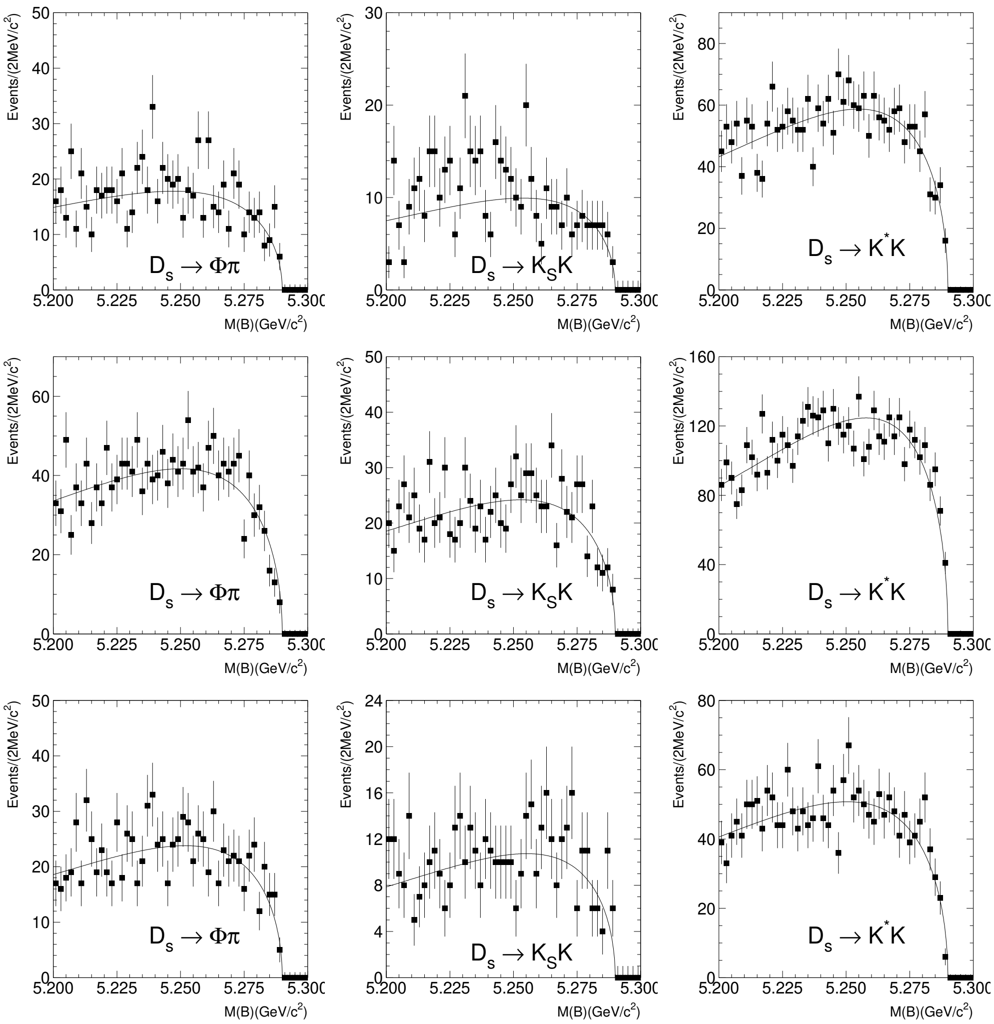

Figure 4.11: Generic MC background shapes in M(B), fitted with Argus function. Top row is for $B^+ \to D_s^{*+}\pi^0$, middle row is for $B^0 \to D_s^{*+}\pi^-$, and the bottom row is for $B^0 \to D_s^{*-}K^+$ mode. From left to right, D_s^+ decay modes $\phi\pi$ K_S^0K and $K^{*0}K$ are shown.

is very small. The above mentioned estimation does not account for this type of peaking backgrounds, they were simulated separately. Then the number of events

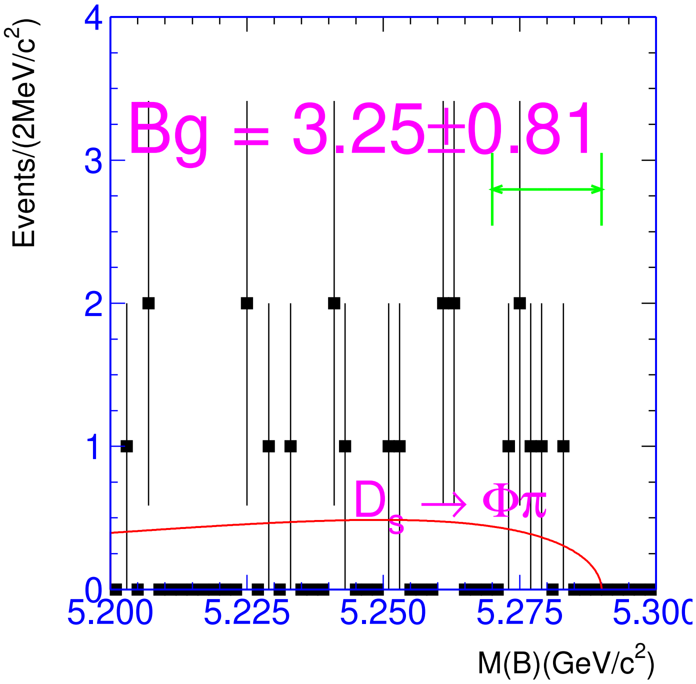

Figure 4.12: Background Shape: M(B) is fitted with the Argus function excluding the signal region and then extrapolated into the signal region. This plot was made for $B^0 \to D_s^{*-} K^+$ with $D_s^+ \to \phi\pi^+$

that passed all the selection requirements were counted. Table 4.2 shows the peaking modes in detail.

When there is no event in the signal region after the selection procedure, the requirement in $\mathcal{F}$ is released and the number of events in the signal region are counted. This number is then scaled down according to the efficiency of the $\mathcal{F}$ requirement. The total peaking background is obtained by adding contributions from all modes together. If no events are found for a particular background mode even without the Fisher selection, then an upper limit of the peaking background, is estimated at 90%

Analysis Mode	D_s Mode	Bg. Mode	Sub. Decay	No. gen.	Estimated Bg.
$B \to D_s{}^*\pi^0$	$\phi\pi$	$D^*\pi^0$	$D^* \to D(\phi\pi)\gamma$	2000	< 0.002
	K_sK	$D^*\pi^0$	$D^* \to D(K_sK)\gamma$	2000	0.0005 ± 0.0005
		$D^*\rho$	$D^* \to K_s\pi$	100k	0.024 ± 0.024
		$D\rho$	$D \to K_s\pi$	105k	0.165 ± 0.165
	K^*K	$D^*\pi^0$	$D^* \to D(K\pi\pi)\gamma$	5000	0.008 ± 0.008
		$D\rho$	$D \to K^*\pi$	105k	0.581 ± 0.290
		$D\rho$	$D \to K\pi\pi$	110k	0.046 ± 0.046
$B \to D_s{}^*\pi$	$\phi\pi$	$D^*\pi$	$D^* \to D(\phi\pi)\gamma$	2000	< 0.02
	K_SK	$D\rho$	$D \to K_S\pi$	105k	0.991 ± 0.372
	K^*K	$D^*\pi$	$D^* \to D(K\pi\pi)\gamma$	25k	0.02 ± 0.02
		$D^*\pi$	$D^* \to D(K^*K)\gamma$	2000	0.018 ± 0.013
		$D\rho$	$D \to D(K^*\pi)\gamma$	105k	0.290 ± 0.205
		$D\pi$	$D \to K\pi\pi$	210k	0.196 ± 0.196
$B \to D_s{}^*K$	$\phi\pi$	$D^*\pi$	$D^* \to D(\phi\pi)\gamma$	2000	< 0.023
		D^*K	$D^* \to D(\phi\pi)\gamma$	1000	< 0.003
	K_SK	$D^*\pi$	$D^* \to D(K_SK)\gamma$	2000	< 0.028
		D^*K	$D^* \to D(K_SK)\gamma$	1000	< 0.003
	K^*K	$D^*\pi$	$D^* \to D(K^*K)\gamma$	2000	< 0.021
		D^*K	$D^* \to D(K^*K)\gamma$	1000	< 0.003
		D^*K	$D^* \to D(K\pi\pi)\gamma$	1000	0.044 ± 0.044

Table 4.2: Estimated background in 250 fb^-1 of data, for different background modes. No. gen. is the number of simulated events used for the study.

confidence level. If there is no background found in any of the peaking modes, total peaking background is also calculated as an upper limit, at 90% confidence level.

4.4.2 Sideband Analysis

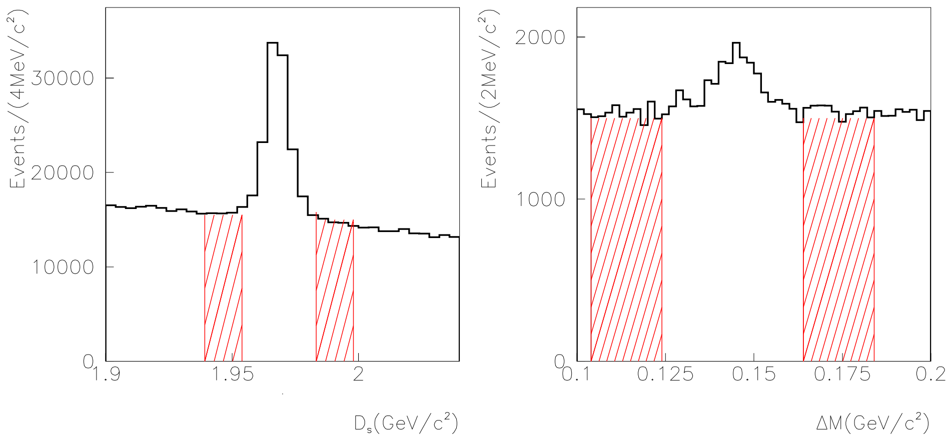

Figure 4.13: Sideband regions of D_s and ΔM(cross hatched) from $\pm 4.5\sigma$ away from the signal mean. $D_s^+ \to \phi\pi^+$ mode was used for the above plots.

The background estimated in the previous section are completely Monte Carlo dependent. Event generation, tracking efficiencies, and neutral particle efficiencies may not be accurate in these simulated events. Also there can be some rare decay modes that are not accounted for. Therefore, sidebands of D_s^+ and ΔM are studied. Sidebands of D_s^+ can be used to study the background from accidental D_s^+. Also sidebands of ΔM can be used to study background from real D_s^+ but not $D_s^{*+} \to D_s^+\gamma$. They are expected to provide a good estimate of the shape and rate of the background in the signal region.

Sidebands of D_s^+ are selected in the criteria same as the signal except the requirement for $\mathcal{F}$. Sidebands are centered at $\pm 4.5\sigma$ away from the signal mean. For $D_s^+ \to$

$\phi\pi^+$ mode, upper and lower sidebands of D_s^+ are selected as $1.9392 < M(D_s^+) < 1.9539$ GeV/c^2, and $1.9833 < M(D_s^+) < 1.9980$ GeV/c^2 ($\pm 1.5\sigma$). For $D_s^+ \to \bar{K}^0 K^+$ mode, $1.9256 < M(D_s^+) < 1.9471$ GeV/c^2, and $1.9901 < M(D_s^+) < 2.0116$ GeV/c^2 ($\pm 1.5\sigma$). The sideband selection for $D_s^+ \to \bar{K}^* K^+$ mode, is $1.9304 < M(D_s^+) < 1.9495$ GeV/c^2, and $1.9877 < M(D_s^+) < 2.0068$ GeV/c^2 ($\sim \pm 1.5\sigma$). The differences in the sideband selection criteria for different D_s^+ decay mode is due to the slight differences observed in the width and mean.

Sidebands of ΔM are centered at $\pm 4.5\sigma$ from the signal mean and, $0.104 < \Delta M < 0.124$ GeV/c^2 and $0.164 < \Delta M < 0.184$ GeV/c^2 ($\pm 1.5\sigma$). Upper and lower sidebands are added together into a single sideband. The range of each side band is selected in such a way that, when added together, its width is same as the signal width. Since the signal of D_s^+ and ΔM are selected as $\pm 3\sigma$ from their nominal values, the total width of the signal is also 6σ. The sidebands are selected with all cuts except the requirement for $\mathcal{F}$. It has been seen that, for the candidates selected from the sidebands, the shapes of $M(B)$ distributions in generic MC are consistent with background shapes in the signal region (see Fig. 4.14-4.19).

Data and generic Monte Carlo sidebands are fitted with the same background shape obtained from the generic Monte Carlo backgrounds and then integrated in the signal region to obtain the number of background events. If there is any peakings in the signal region, a Gaussian shape is also added for the background shape. Sideband shapes of data and generic Monte Carlo are in good agreement for both D_s and ΔM.

The differences between estimated background levels in data and Monte Carlo range from 12% - 22%. Figures 4.14 - 4.19 show sideband shapes for data and generic Monte Carlo. Also see tables 4.11 and 4.12. This difference does not affect the results since we use the sidebands of data to estimate the background levels. Another observation is that the sideband shapes of ΔM closely represent the background shape in the signal region than the sideband shapes of D_s. The reason is that the background of D_s is not completely random, but there are real D_s candidates that do not come from $D_s^{*+} \to D_s^+ \gamma$ decays.

4.5 Reconstruction efficiencies

4.5.1 Estimate using signal Monte Carlo Events

One way to obtain reconstruction efficiencies is by using signal Monte Carlo events. Each signal mode is simulated with one B decaying to the signal mode while the other decays generically. The beam constrained mass distribution for each mode, after all the selection requirements, was fitted with a Gaussian and an Argus function [**?**]. Background events from generic Monte Carlo were added to signal for fitting. The histogram was fitted with the Argus function plus a Gaussian shape. The mean and width of the Gaussian shape was kept free for the fitting. Table 4.5 summarizes the results.

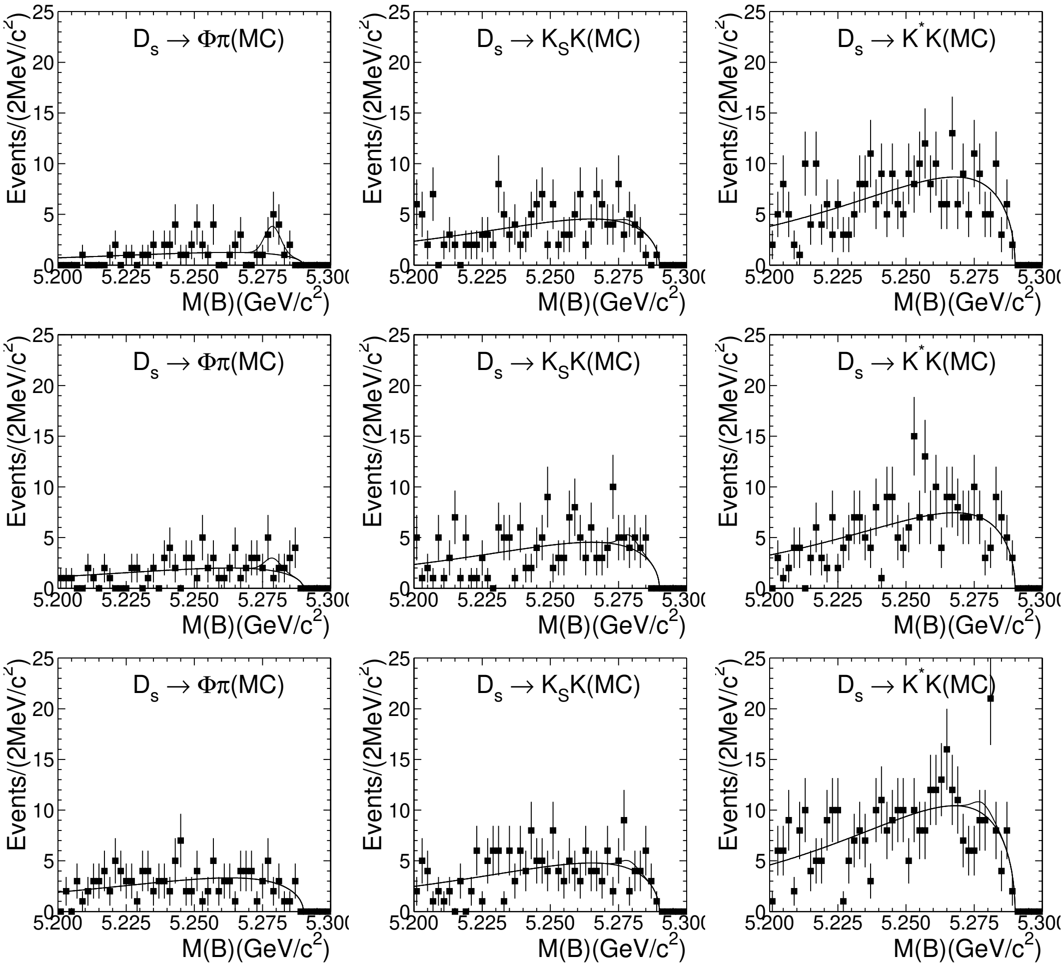

Figure 4.14: Comparisons of MC sidebands with signal region for $D_s^{*+}\pi^0$ mode. The first row is for MC sidebands of D_s. The second and third rows are for MC sidebands of ΔM and the MC background in the signal region respectively. First, second and third, columns show the three D_s decay modes, $\phi\pi$, $K_S^0 K$, $K^{*0} K$ respectively. Experiment 7 - 33 data were used for MC sidebands.

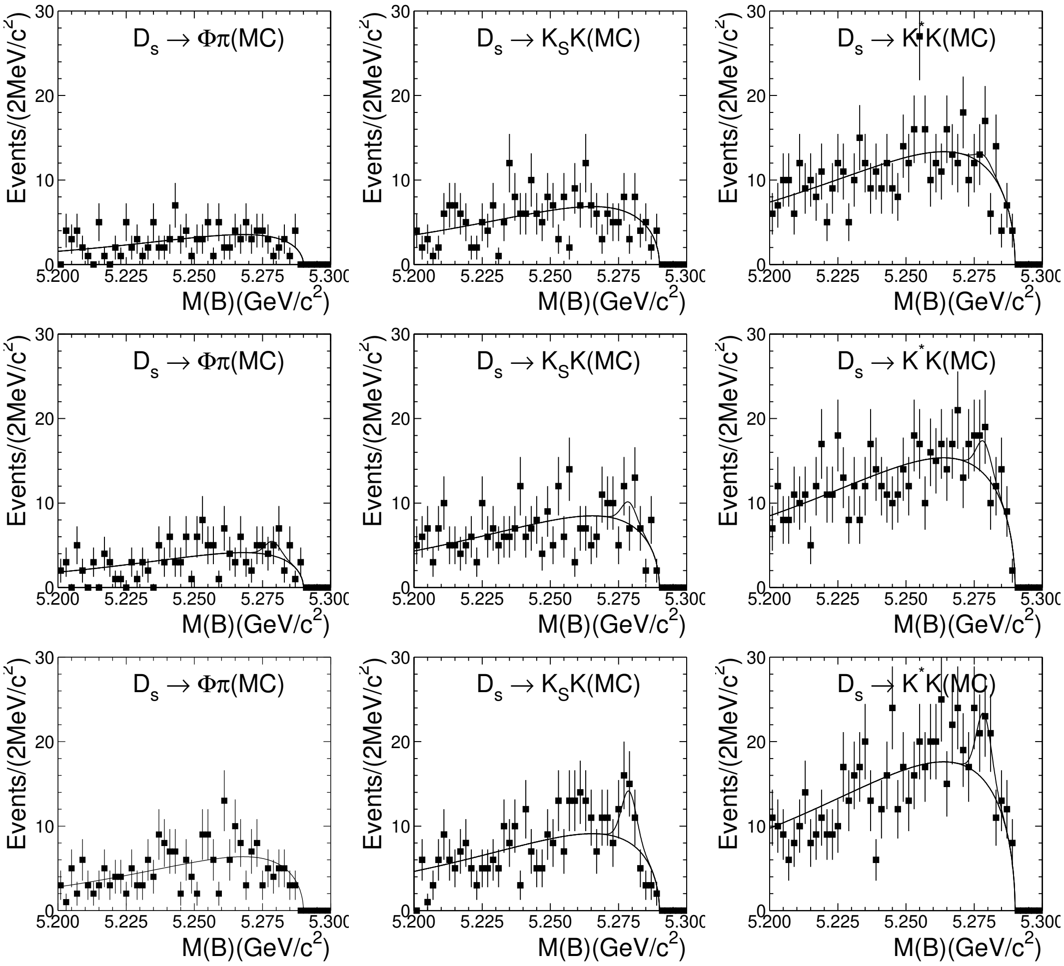

Figure 4.15: Comparisons of MC sidebands with signal region for $D_s^{*+}\pi^-$ mode. The first row is for MC sidebands of D_s. The second and third rows are for MC sidebands of ΔM and the MC background in the signal region respectively. First, second and third, columns show the three D_s decay modes, $\phi\pi$, $K_S^0 K$, $K^{*0}K$ respectively. Experiment 7 - 33 data were used for MC sidebands.

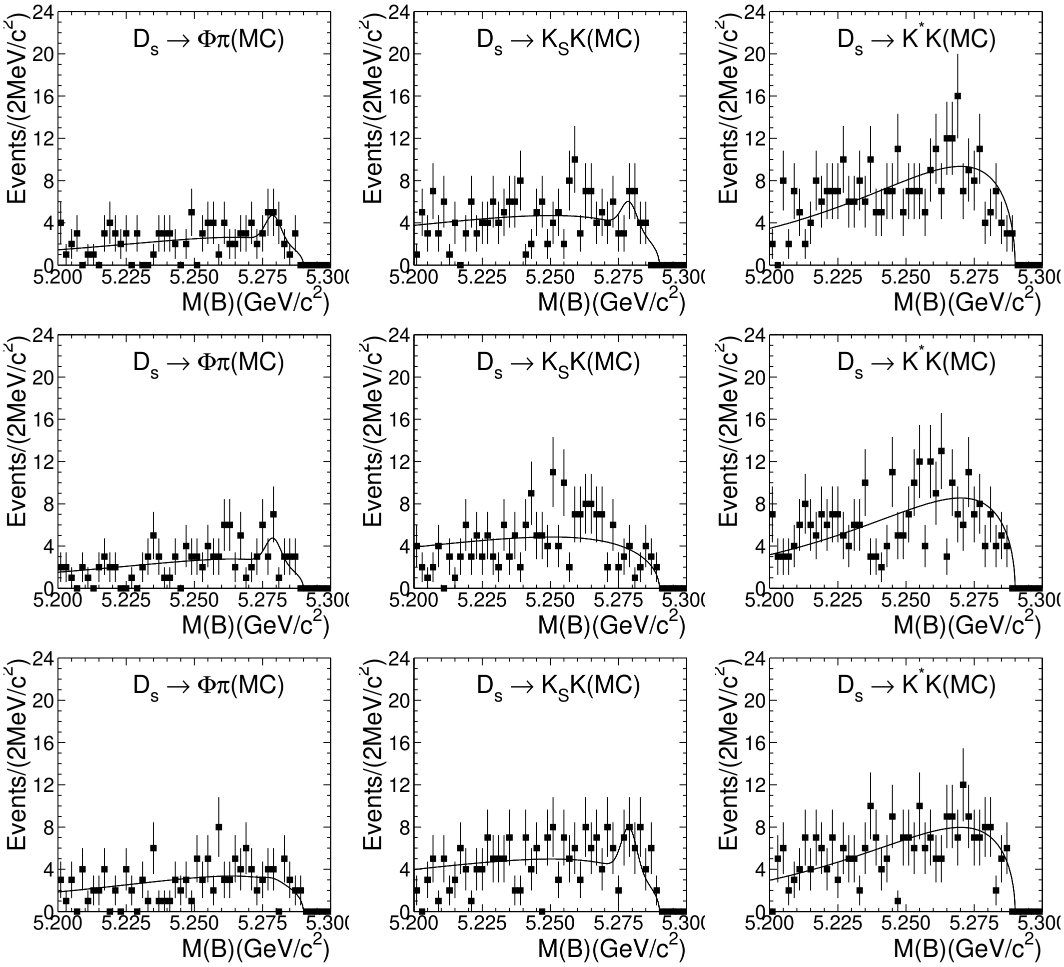

Figure 4.16: Comparisons of MC sidebands with signal region for $D_s^{*-}K^+$ mode. The first row is for MC sidebands of D_s. The second and third rows are for MC sidebands of ΔM and the MC background in the signal region respectively. First, second and third, columns show the three D_s decay modes, $\phi\pi$, $K_S^0 K$, $K^{*0} K$ respectively. Experiment 7 - 33 data were used for MC sidebands.

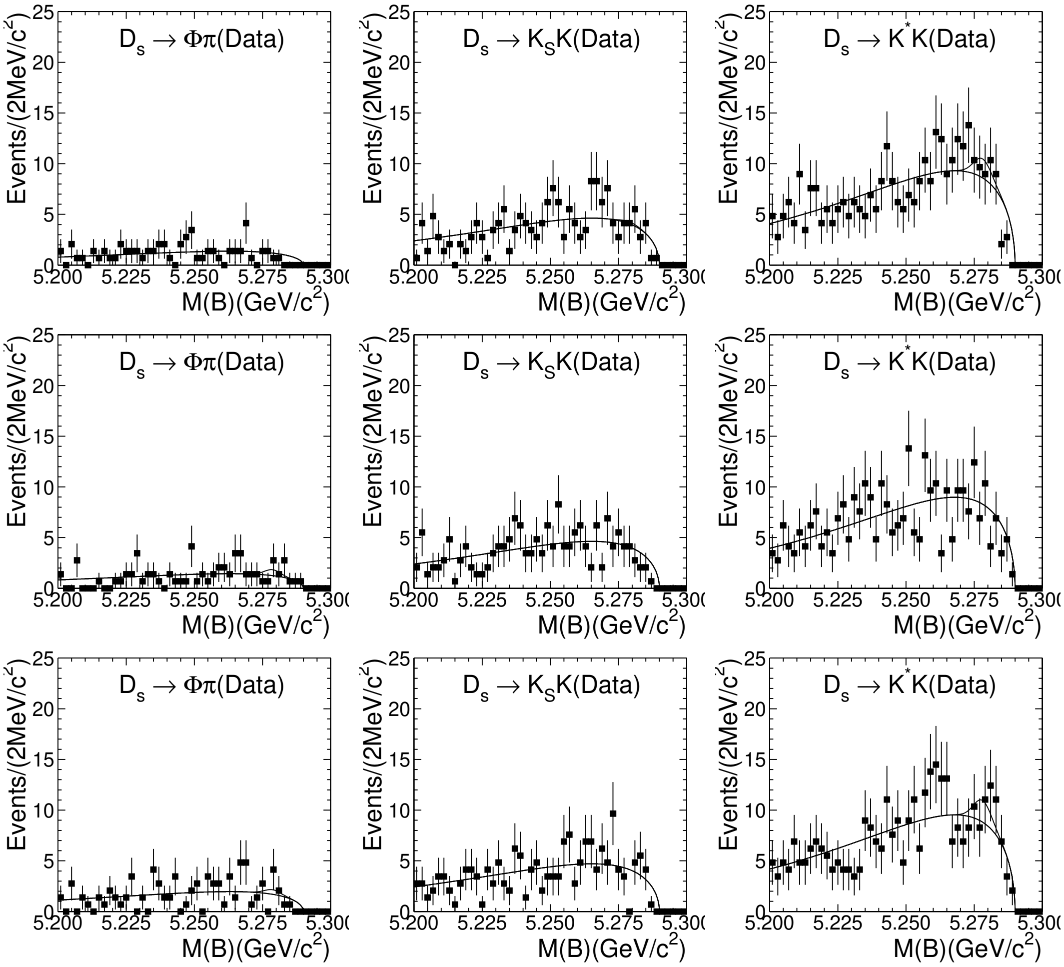

Figure 4.17: Comparisons of data sidebands with signal region for $D_s^{*+}\pi^0$ mode. The first row is for sidebands of D_s. The second and third rows are for the sidebands of ΔM and the background in the signal region respectively. First, second and third, columns show the three D_s decay modes, $\phi\pi$, K_S^0K, $K^{*0}K$ respectively. Experiment 7 - 37 data were used for the sidebands.

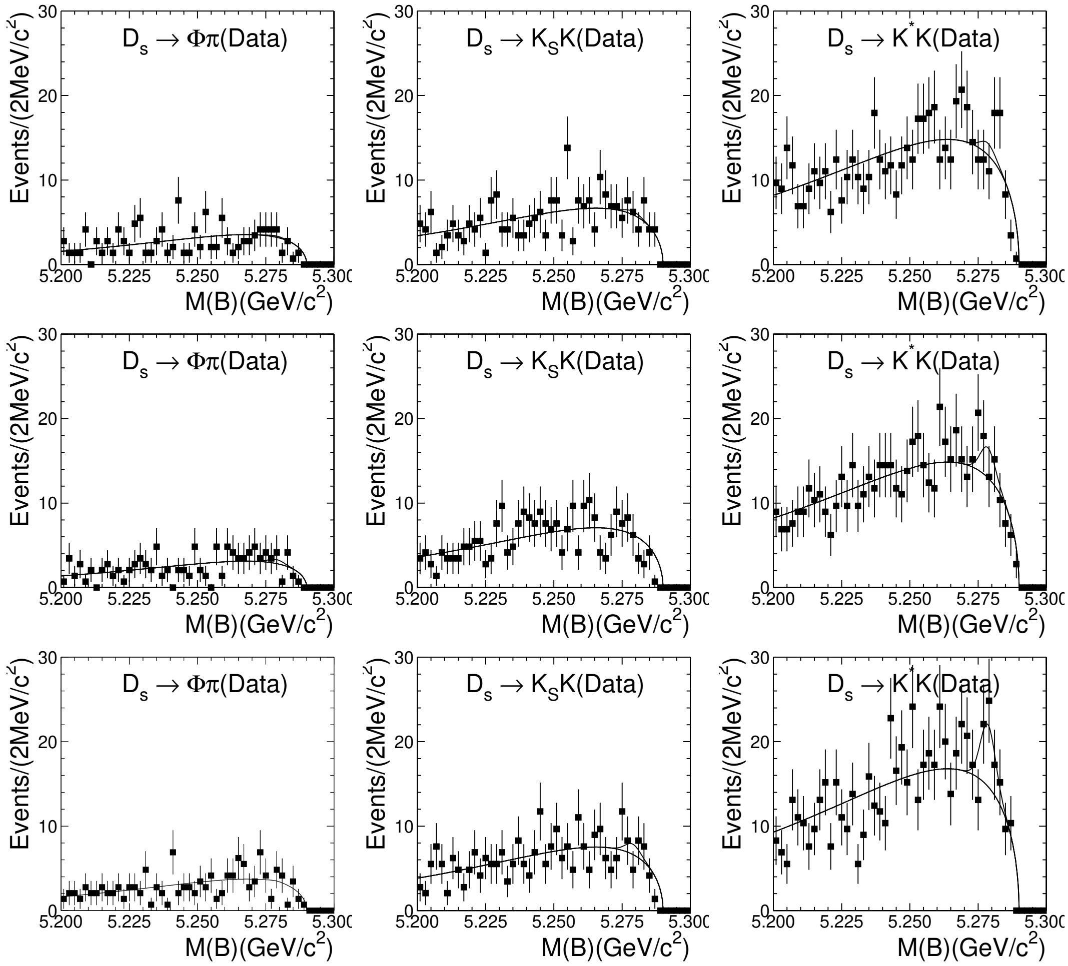

Figure 4.18: Comparisons of data sidebands with signal region for $D_s^{*+}\pi^-$ mode. The first row is for sidebands of D_s. The second and third rows are for the sidebands of ΔM and the background in the signal region respectively. First, second and third, columns show the three D_s decay modes, $\phi\pi$, $K_S^0 K$, $K^{*0} K$ respectively. Experiment 7 - 37 data were used for the sidebands.

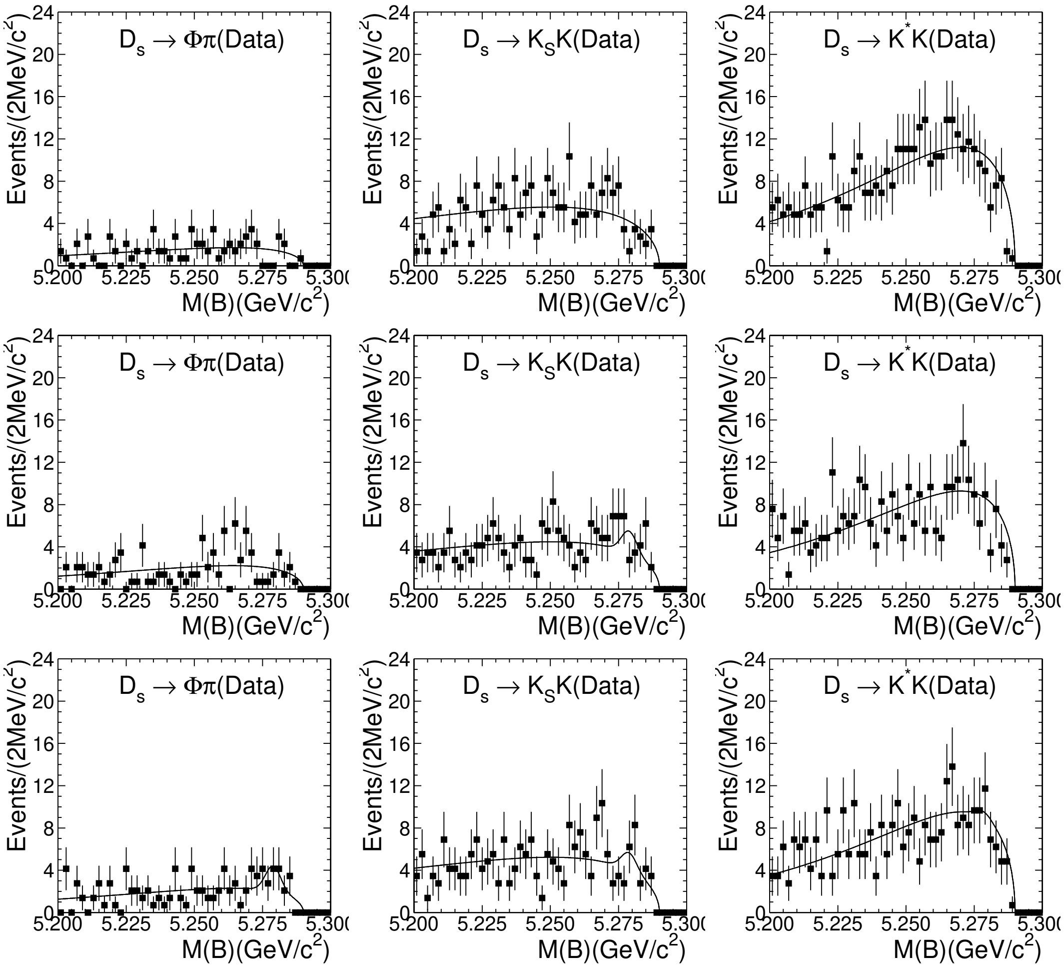

Figure 4.19: Comparisons of data sidebands with signal region for $D_s^{*-}K^+$ mode. The first row is for sidebands of D_s. The second and third rows are for the sidebands of ΔM and the background in the signal region respectively. First, second and third, columns show the three D_s decay modes, $\phi\pi$, $K_S^0 K$, $K^{*0}K$ respectively. Experiment 7 - 37 data were used for the sidebands.

Analysis mode	Sub dec. mode	events generated	Yield	eff. $(\epsilon)\%$
$D_s^{*-}\pi^0$	$\phi\pi$	6000	231 ± 16	3.85 ± 0.26
	$K_S K$	14,000	373 ± 20	3.88 ± 0.21
	$K^* K$	6000	155 ± 15	2.65 ± 0.25
$D_s^{*+}\pi^-$	$\phi\pi$	10,000	848 ± 30	8.48 ± 0.30
	$K_S K$	10,000	471 ± 22	6.86 ± 0.32
	$K^* K$	10,000	303 ± 18	3.13 ± 0.18
$D_s^* K^+$	$\phi\pi$	10,000	675 ± 26	6.75 ± 0.26
	$K_S K$	10,000	404 ± 21	4.04 ± 0.21
	$K^* K$	10,000	492 ± 23	4.92 ± 0.23

Table 4.3: Reconstruction efficiencies, using signal Monte Carlo. No. of events generated and the yield obtained by the fitting, are also indicated in the table. All selection requirements were used including the π^0 veto.

4.5.2 Efficiency correction using inclusive D_s^{*+}

It was suspected that the relative total efficiencies in MC are not consistent with the relative yields obtained from real data. Inclusive D_s^+ and D_s^{*+} yields for both data and generic Monte Carlo events were studied. D_s^{*+} yields were obtained with and without the π^0 veto, since π^0 veto could be a possible source for a discrepancy; It is known that efficiencies of photon detection is not well modeled by Monte Carlo. The momentum of D_s^{*+} in $\Upsilon(4S)$ frame is required to be between 1.7 GeV/c and 2.5 GeV/c. This is approximately the kinematically allowed region for D_s^{*+}, that comes from $D_s^* h$ decays.

	Data		
	$\phi\pi$	K_SK	K^*K
D_s yield	7787 ± 159	2662 ± 246	8479 ± 346
$/\phi\pi$	1.0	0.342 ± 0.032	1.089 ± 0.050
D_s^{*+} yield (no π^0 veto)	2162 ± 117	826 ± 132	2107 ± 200
$/\phi\pi$	1.0	0.382 ± 0.042	0.975 ± 0.106
D_s^{*+} yield (with π^0 veto)	1632 ± 82	724 ± 129	1623 ± 134
$/\phi\pi$	1.0	0.444 ± 0.082	0.994 ± 0.096
	MC		
	$\phi\pi$	K_SK	K^*K
D_s yield	8388 ± 148	3708 ± 190	9140 ± 279
$/\phi\pi$	1.0	0.442 ± 0.024	1.090 ± 0.038
D_s^{*+} yield (no π^0 veto)	3515 ± 118	2338 ± 179	3128 ± 187
$/\phi\pi$	1.0	0.665 ± 0.055	0.890 ± 0.061
D_s^{*+} yield (with π^0 veto)	2282 ± 77	1310 ± 97	2181 ± 113
$/\phi\pi$	1.0	0.574 ± 0.047	0.955 ± 0.059

Table 4.4: Data-MC comparison of inclusive yield for D_s and D_s^{*+}. Yields are compared with the yield of $D_s \to \phi\pi$ mode. The data sample contains ~ 171.9 million $B\bar{B}$ events. The generic Monte Carlo sample equivalent to a data sample containing ~ 152 million $B\bar{B}$ events.

Table 4.6 shows a clear difference in efficiencies; Relative yields (between D_s^+ modes) are not consistent with between data and Monte Carlo. There is a large difference in the ratio of efficiencies of the $D_s^+ \to K_S^0 K^+$ mode to $D_s^+ \to \phi\pi^+$ mode. For data, the efficiency ratio for $D_s^+ \to K_S^0 K$ is 0.342 ± 0.032, and for generic Monte Carlo it is 0.442 ± 0.024. The difference is even larger for D_s^{*+} yields. However the efficiency ratio of generic Monte Carlo events for $D_s^+ \to K^* K^+$ to $D_s^+ \to \phi\pi^+$ mode, is consistent with data. There is no evidence that the π^0 veto makes a difference to the agreement between MC and data. To optimize the accuracy of the measurements the reconstruction efficiencies are corrected in the following way. Assume we have N_{tot} number of D_s^{*+} in the data sample considered. Let the efficiencies of $D_s^+ \to \phi\pi^+, \bar{K}^0 K^+, K^* K^+$ be $\epsilon_{\phi\pi}$, $\epsilon_{K_S K}$ are $\epsilon_{K^* K}$ respectively. Also let the inclusive yields be $N_{\phi\pi}$, $N_{K_S K}$, $N_{K^* K}$ respectively. Then

$$\begin{aligned} N_{\phi\pi} &= N_{tot} \times Br(D_s^{*+} \to D_s^+ \gamma) \times Br(D_s^+ \to \phi\pi^+) \\ &\quad \times Br(\phi \to K^+ K^-) \times \epsilon_{\phi\pi} \end{aligned} \tag{4.10}$$

$$\begin{aligned} N_{K_S K} &= N_{tot} \times Br(D_s^{*+} \to D_s^+ \gamma) \times Br(D_s^+ \to \bar{K}_S^0 K^+) \\ &\quad \times Br(K_S^0 \to \pi^+ \pi^-) \times \epsilon_{K_S K} \end{aligned} \tag{4.11}$$

$$\begin{aligned} N_{K^* K} &= N_{tot} \times Br(D_s^{*+} \to D_s^+ \gamma) \times Br(D_s^+ \to \bar{K}^{*0} K^+) \\ &\quad \times Br(K^{*0} \to K^+ \pi^-) \times \epsilon_{K^* K} \end{aligned} \tag{4.12}$$

By dividing, N_{tot} cancels out:

$$\frac{Br(D_s^+ \to \phi\pi^+)}{Br(D_s^+ \to \bar{K}_S^0 K^+)} \times \frac{Br(\phi \to K^+ K^-)}{Br(K_S^0 \to \pi^+ \pi^-)} = \frac{\epsilon_{K_S K}}{\epsilon_{\phi\pi}} \times \frac{N_{\phi\pi}}{N_{K_S K}} \tag{4.13}$$

Similarly,

$$\frac{Br(D_s^+ \to \phi\pi^+)}{Br(D_s^+ \to \bar{K}^{*0} K^+)} \times \frac{Br(\phi \to K^+ K^-)}{Br(K^{*0} \to K^+ \pi^-)} = \frac{\epsilon_{K^* K}}{\epsilon_{\phi\pi}} \times \frac{N_{\phi\pi}}{N_{K^* K}} \tag{4.14}$$

$N_{\phi\pi}$, $N_{K_S K}$, $N_{K^* K}$ are obtained by fitting ΔM, which is reconstructed inclusively using data. Branching fractions of D_s^+ decays relative to $D_s^+ \to \phi\pi^+$ mode are known values. Also branching fractions of $\phi \to K^+K^-$, $K_S^0 \to \pi^+\pi^-$, and $K^{*0} \to K^+\pi^-$ are known. $\epsilon_{\phi\pi}$ is obtained from Signal Monte Carlo events with all the selection requirements except Fisher requirement, and use that value to obtain the other two efficiencies. Efficiency of the Fisher requirement is obtained separately, since the Fisher requirement is different for the three D_s decay modes. To obtain the total reconstruction efficiency, we multiply each obtained value by the efficiency of the Fisher selection.

Total reconstruction efficiencies can be summarized as follows.

$$\epsilon_{\phi\pi}(tot.) = \epsilon_{\phi\pi} \times \epsilon'_{\phi\pi} \tag{4.15}$$

$$\epsilon_{K_SK}(tot.) = \frac{Br(D_s^+ \to \phi\pi^+)}{Br(D_s^+ \to \bar{K}_S^0 K^+)} \times \frac{Br(\phi \to K^+K^-)}{Br(K_S^0 \to \pi^+\pi^-)} \times \frac{N_{K_SK}}{N_{\phi\pi}} \times \epsilon_{\phi\pi} \times \epsilon'_{K_SK} \tag{4.16}$$

$$\epsilon_{K^*K}(tot.) = \frac{Br(D_s^+ \to \phi\pi^+)}{Br(D_s^+ \to \bar{K}^{*0} K^+)} \times \frac{Br(\phi \to K^+K^-)}{Br(K^{*0} \to K^+\pi^-)} \times \frac{N_{K^*K}}{N_{\phi\pi}} \times \epsilon_{\phi\pi} \times \epsilon'_{K^*K} \tag{4.17}$$

where $\epsilon'_{\phi\pi}$, ϵ'_{K_SK}, ϵ'_{K^*K} are the efficiencies of the Fisher selection of $D_s^+ \to \phi\pi^+$, $D_s^+ \to K_SK^+$ and $D_s^+ \to K^*K$ modes respectively.

4.6 Branching fractions and Upper Limits using Event Counting Method

In this method the number of events in the signal region (see section 4.3.1) was considered as the yield. The individual branching fractions for the D_s^+ decay modes can be obtained as follows. Let the number of events in the signal region be n and

Mode	rec. efficiency(%)	eff. Fisher	total efficiency
$D_s^{*+}\pi^0$			
$D_s^+ \to \phi\pi^+$	$7.65 \pm .36$	$0.841 \pm .004$	$0.064 \pm .003$
$D_s^+ \to K^0 K^+$	$4.19 \pm .79$	$0.958 \pm .007$	$0.040 \pm .008$
$D_s^+ \to K^* K^+$	$7.10 \pm .90$	$0.750 \pm .020$	$0.053 \pm .007$
$D_s^{*+}\pi^-$			
$D_s^+ \to \phi\pi^+$	$14.69 \pm .39$	$0.953 \pm .002$	$0.140 \pm .004$
$D_s^+ \to K^0 K^+$	8.04 ± 1.48	$0.758 \pm .012$	$0.061 \pm .011$
$D_s^+ \to K^* K^+$	13.53 ± 1.64	$0.389 \pm .012$	$0.053 \pm .007$
$D_s^{*+}K^-$			
$D_s^+ \to \phi\pi^+$	$12.94 \pm .36$	$0.873 \pm .003$	$0.113 \pm .003$
$D_s^+ \to K^0 K^+$	7.08 ± 1.30	$0.720 \pm .013$	$0.051 \pm .009$
$D_s^+ \to K^* K^+$	12.06 ± 1.49	$0.741 \pm .012$	$0.089 \pm .011$

Table 4.5: Reconstruction Efficiencies using inclusive ΔM-without π^0 veto. Reconstruction efficiency (without Fisher selection), efficiency of the Fisher selection, and the total reconstruction efficiency is shown. Reconstruction efficiency for $D_s^+ \to \phi\pi^+$ mode is obtained from signal Monte Carlo events.

the estimated background be b. If the total number of $B\bar{B}$ events in the data sample is N_{BB} and the total efficiency including reconstruction efficiency and the branching fractions of sub decay modes is ϵ then,

$$n - b = \quad N_{BB} \times Br \times \epsilon \tag{4.18}$$

$$Br = \quad (n - b)/(N_{BB} \times \epsilon) \tag{4.19}$$

We counted the number of events in the signal region and then constructed a likelihood function as follows. Let n_i be the number of expected events in the signal

Mode	rec. efficiency (%)	eff. Fisher	total efficiency
$D_s^{*+}\pi^0$			
$D_s^+ \to \phi\pi^+$	$4.63 \pm .28$	$0.832 \pm .005$	$0.039 \pm .003$
$D_s^+ \to K^0K^+$	$2.55 \pm .48$	$0.958 \pm .007$	$0.024 \pm .005$
$D_s^+ \to K^*K^+$	$4.09 \pm .50$	$0.750 \pm .020$	$0.031 \pm .004$
$D_s^{*+}\pi^-$			
$D_s^+ \to \phi\pi^+$	8.93 ± 0.30	$0.948 \pm .002$	$0.085 \pm .003$
$D_s^+ \to K^0K^+$	4.92 ± 0.89	$0.758 \pm .012$	$0.037 \pm .007$
$D_s^+ \to K^*K^+$	7.84 ± 0.87	$0.389 \pm .012$	$0.031 \pm .004$
$D_s^{*+}K^-$			
$D_s^+ \to \phi\pi^+$	$7.91 \pm .28$	$0.853 \pm .004$	$0.068 \pm .003$
$D_s^+ \to K^0K^+$	4.36 ± 0.79	$0.720 \pm .013$	$0.031 \pm .006$
$D_s^+ \to K^*K^+$	7.03 ± 0.78	$0.741 \pm .012$	$0.052 \pm .006$

Table 4.6: Reconstruction Efficiencies using inclusive ΔM-with π^0 veto. Reconstruction efficiency (without Fisher selection), efficiency of the Fisher selection, and the total reconstruction efficiency is shown. Reconstruction efficiency for $D_s^+ \to \phi\pi^+$ mode is obtained from signal Monte Carlo events.

region for the i^{th} D_s decay mode, Br be the branching fraction and b_i be the total estimated background. Assuming Poisson Distribution for the observed number of events in the signal region (N_i), a probability density function (PDF) can be written as,

$$PDF = \frac{(N_{B\bar{B}} \times Br \times \epsilon_i + b_i)^{N_i} \times e^{-(N_{B\bar{B}} \times Br \times \epsilon_i + b_i)}}{N_i!} \tag{4.20}$$

where ϵ_i is the total efficiency including the branching fractions of sub decays and reconstruction efficiency, and $N_{B\bar{B}}$ is the number of $B\bar{B}$ events in the data sample.

After dropping the constant terms and summing up for the three sub decay modes the total log likelihood($\mathcal{L}$) becomes,

$$ln\mathcal{L} = \sum_{i=1}^{3} N_i \times ln(N_{B\bar{B}} \times Br \times \epsilon_i + b_i) - (N_{B\bar{B}} \times Br \times \epsilon_i + b_i) \tag{4.21}$$

Maximum value of $ln\mathcal{L}$ gives the most probable value for the branching fraction.

4.6.1 Obtaining the Branching fractions

Branching fraction corresponds to the maximum log likelihood is obtained by the curve, maximum log likelihood vs branching fraction. The values 0.5 below the maximum log likelihood are used to obtain the errors of the branching fraction. There are two branching fractions correspond to two points which are .5 below the maximum log likelihood, on either side of the curve. These two values provide the interval that the possible branching fraction can lie.

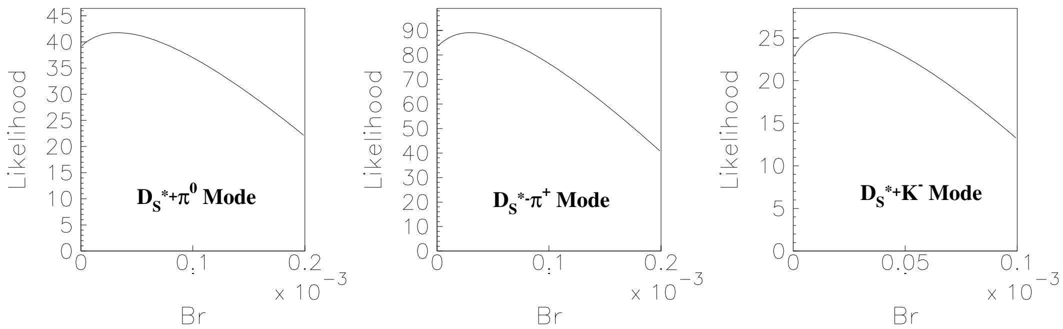

Figure 4.20: Log likelihood($ln\mathcal{L}$) vs. branching fraction(Br) for $D_s{}^*\pi^0$, $D_s{}^*\pi$ and $D_s{}^*K$ modes respectively.

The branching fractions for $B^+ \to D_s^{*+}\pi^0$, $B^0 \to D_s^{*+}\pi^-$ and $B^+ \to D_s^{*-}K^+$ are $(2.55 \pm^{1.30}_{1.09}) \times 10^{-5}$, $(2.32 \pm^{0.93}_{0.83}) \times 10^{-5}$, and $(1.13 \pm^{0.77}_{0.66}) \times 10^{-5}$ respectively.

4.6.2 Obtaining the Upper Limits

If no signal candidates are found, an upper limit at 90% confidence level is obtained in the following way. First 500 numerical experiments with fixed branching fraction(B_{gen}) is generated and for each branching fraction $B_{meas.}$ corresponding to the maximum likelihood is found. Then B_{meas} is plotted in a histogram. The branching fraction value such that 10% of the experiments lie below that value is denoted $B_{10}(B_{gen})$. The procedure is repeated for different fixed branching fractions to obtain a curve for $B_{10}(B_{gen})$. The 90% confidence level upper limit for any experimental value B_{exp} is the value of B_{gen} that corresponds to $B_{exp} = B_{10}(B_{gen})$.

4.6.3 Branching Fractions

Following branching fractions and upper limits are obtained (see 4.13). The data sample used, contains 274.8 million $B\bar{B}$ events. All selection requirements, including π^0 veto was applied.

$$B(B^+ \to D_s^{*+}\pi^0) = (2.55 \pm^{1.30}_{1.09}) \times 10^{-5} \tag{4.22}$$

$$< 5.12 \times 10^{-5}(\text{at } 90\% \text{ C. L.}) \tag{4.23}$$

$$B(B^0 \to D_s^{*+}\pi^-) = (2.32 \pm^{0.93}_{0.83}) \times 10^{-5} \tag{4.24}$$

$$B(B^0 \to D_s^{*-}K^+) = (1.13 \pm^{0.77}_{0.66}) \times 10^{-5} \tag{4.25}$$

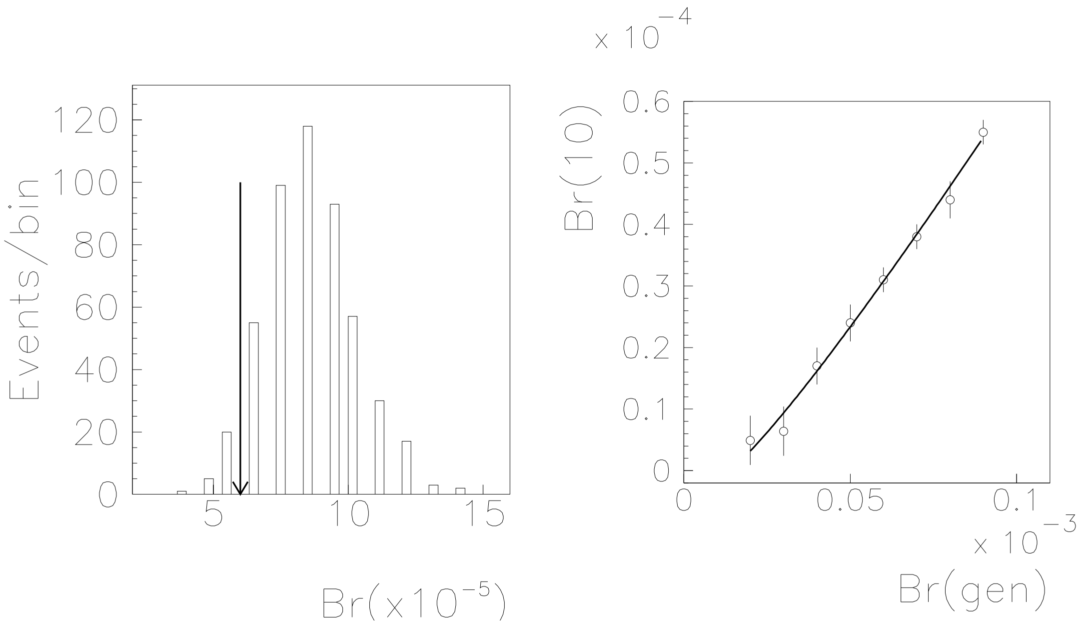

Figure 4.21: Branching fraction corresponds to the maximum likelihood for each experiment(left). The experiments were generated with Br(gen) $= 9\times10^{-}5$ for $D_s^{*+}\pi^0$ mode. The plot on the right shows Br(10) against Br(gen) for the $D_s^{*+}\pi^0$ mode. The fitting function used is $a1 \times Br + a2 \times \sqrt{Br}$.

Only the statistical errors are indicated here.

4.7 Obtaining Branching Fractions Using simultaneous Fit

Sideband analysis has shown that although Data and Monte Carlo backgrounds similar in shapes, levels of the backgrounds are differ by 12% to 22%. Therefore a fitting method is used to reduce the Monte Carlo dependence to obtain the branching fraction. Fitting can account for not only the number of events but also the shape of the histogram. All three D_s decay channels are fitted simultaneously, with a common branching fraction of $B \to D_s^* h$.

Both ΔE and ΔM plots are fitted in this way. To fit all three D_s modes simultaneously, all three modes are plotted in a single histogram. It was done by shifting the three histograms by an integral multiple of the histogram range (see fig. 4.22).

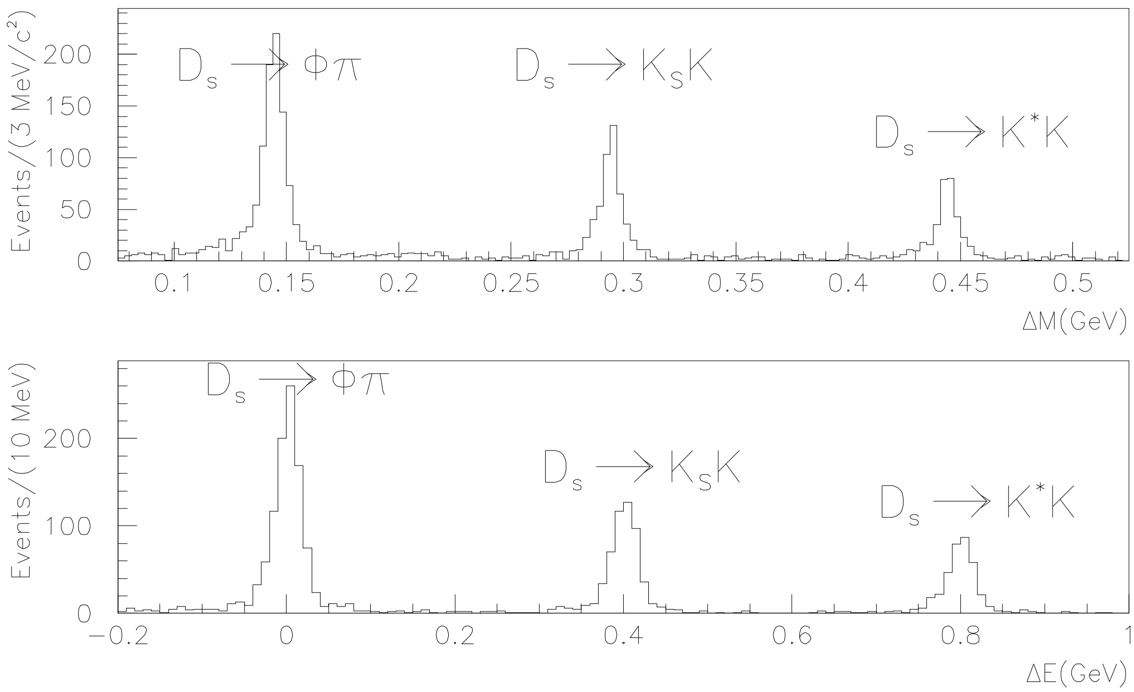

Figure 4.22: Signal MC histograms after shifting for ΔM(top) and ΔE(bottom). The three peaks in each plot represent the signals for $D_s^+ \to \phi\pi^+$, $D_s^+ \to K_S^0 K^+$ and $D_s^+ \to K^{*0} K^+$ modes.

4.7.1 Fitting ΔE

The three signal peaks are fitted with Gaussian shapes. The widths and means of the Gaussian shapes are fixed to the widths and means found by fitting simulated signal events with background. Data show that there are slight differences among the widths and means fitting D_s^+ sub decay channels. Background shape of ΔE is obtained from the sideband shape of ΔM. It has been seen that the sidebands of ΔM represent the background more accurately (section 4.4.2). Since the sideband shapes are obtained with looser cuts to keep enough statistics, they are normalized to the expected background level.

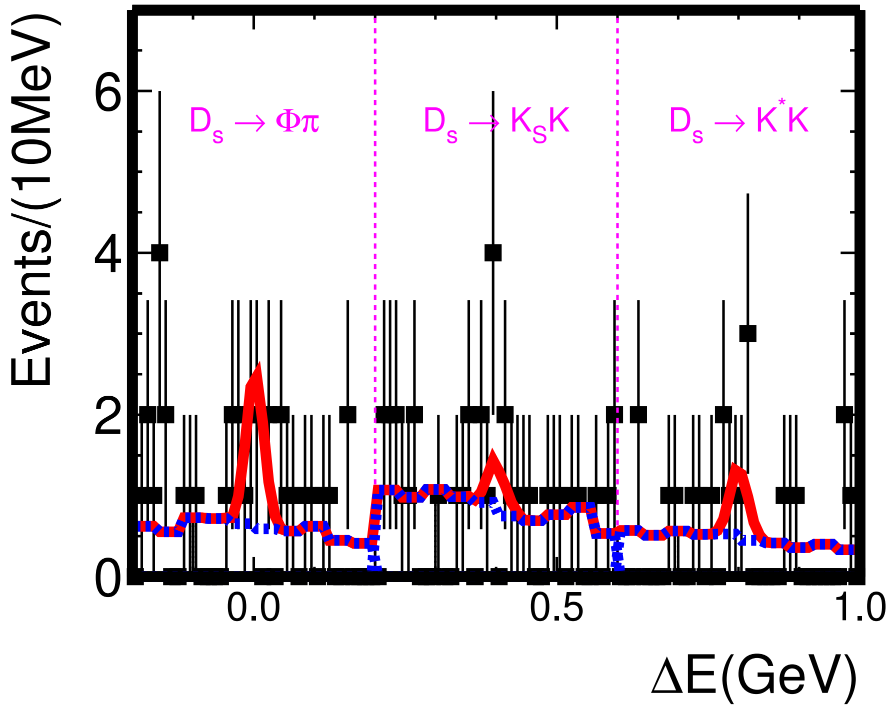

Figure 4.23: Simultaneous fit for ΔE for $D_s^{*+}\pi^+$ mode (with π^0 veto). Data are shown as points with error bars, with fit results overlaid, total (red) and background (blue). Data sample consists of 274.8 million $B\bar{B}$ events. The three peaks in each plot represent the signals for $D_s^+ \to \phi\pi^+$, $D_s^+ \to K_S^0 K^+$ and $D_s^+ \to K^{*0} K^+$ modes.

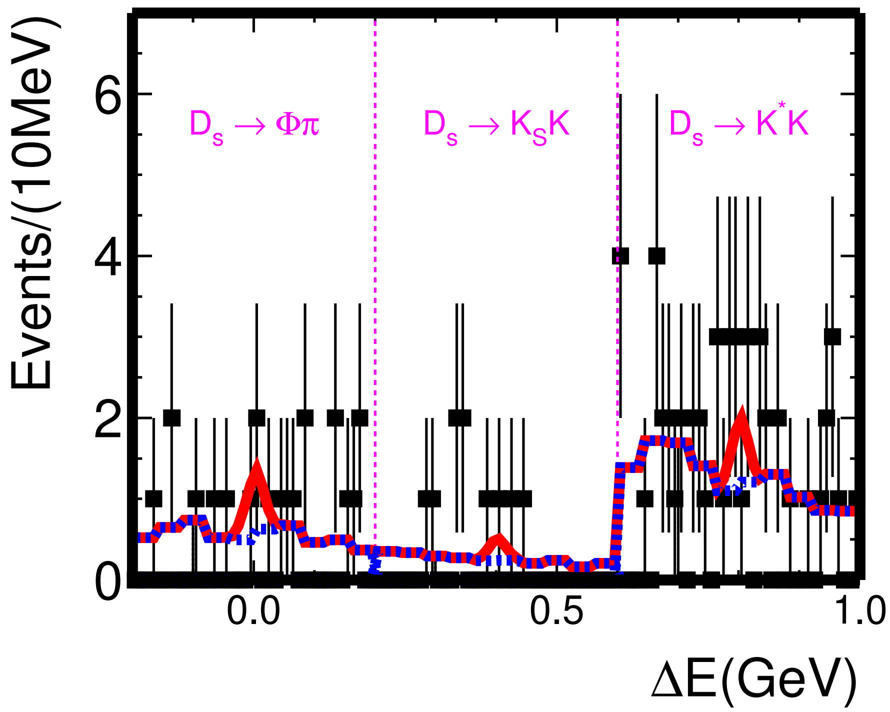

Figure 4.24: Simultaneous fit for ΔE for $D_s^{*+}K^-$ mode (with π^0 veto). Data are shown as points with error bars, with fit results overlaid, total (red) and background (blue). Data sample consists of 274.8 million $B\bar{B}$ events. The three peaks in each plot represent the signals for $D_s^+ \to \phi\pi^+$, $D_s^+ \to K_S^0 K^+$ and $D_s^+ \to K^{*0}K^+$ modes.

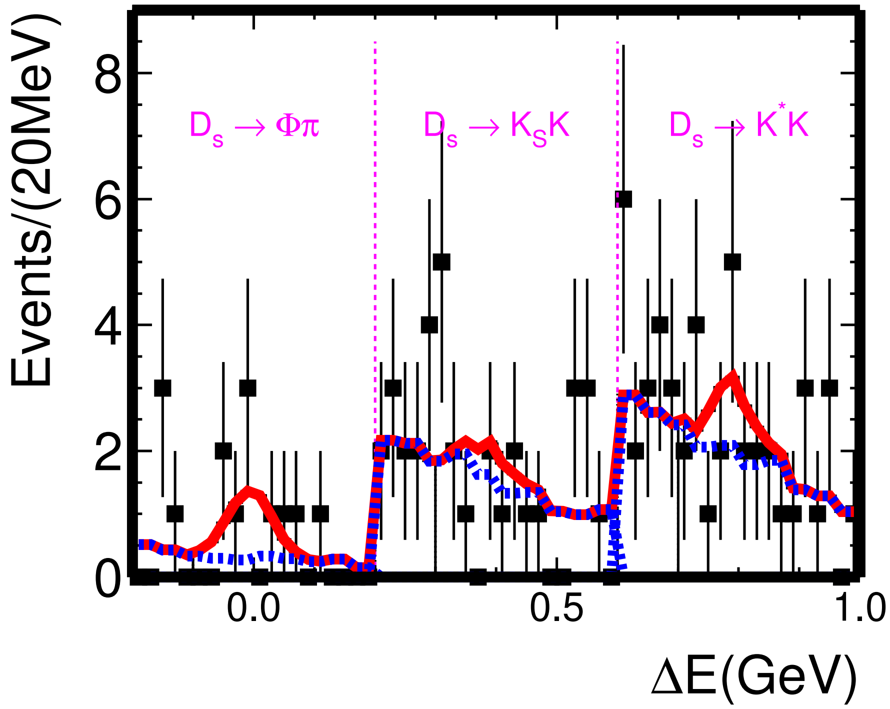

Figure 4.25: Simultaneous fit for ΔE for $D_s^{*+}\pi^0$ mode (with π^0 veto). Data are shown as points with error bars, with fit results overlaid, total (red) and background (blue). Data sample consists of 274.8 million $B\bar{B}$ events. The three peaks in each plot represent the signals for $D_s^+ \to \phi\pi^+$, $D_s^+ \to K_S^0 K^+$ and $D_s^+ \to K^{*0}K^+$ modes.

4.7.2 Fitting ΔM

Signal peaks are fitted with Gaussian shapes, and the widths and means are fixed to the widths and means found by simulated signal events with background. Background is fitted with a straight line shape. The shape is obtained by fitting the ΔM distribution of data using looser selection criteria, excluding the signal region ($0.124 < \Delta M < 0.164$ GeV/c^2).

Mode	rec. eff.(%)	tot. eff.($\times 10^{-4}$)	Sig.	Br($\times 10^{-5}$)
$D_s^* \pi^0$				
$\phi\pi$	3.85 ± 0.23	6.42 ± 1.66	4.82 ± 2.85	2.73 ± 1.76
$K_S K$	2.45 ± 0.46	2.84 ± 0.96	-1.37 ± 2.86	-1.76 ± 3.72
$K^* K$	3.07 ± 0.39	6.53 ± 1.96	1.99 ± 4.86	1.11 ± 2.73
combined				2.81 ± 1.46
$D_s^{*+} \pi^-$				
$\phi\pi$	8.47 ± 0.29	14.13 ± 3.59	4.59 ± 2.98	1.18 ± 0.82
$K_S K$	3.73 ± 0.68	4.33 ± 1.44	4.38 ± 3.12	3.69 ± 2.90
$K^* K$	3.05 ± 0.36	6.53 ± 1.94	5.31 ± 2.97	2.96 ± 1.87
combined				1.82 ± 0.77
$D_s^{*-} K^+$				
$\phi\pi$	6.75 ± 0.24	11.26 ± 2.86	2.10 ± 2.04	0.68 ± 0.68
$K_s K$	3.14 ± 0.58	3.64 ± 1.22	1.45 ± 1.88	1.45 ± 1.94
$K^* K$	5.20 ± 0.59	11.03 ± 3.27	7.34 ± 4.18	2.42 ± 1.56
combined				0.97 ± 0.65

Table 4.7: Branching fractions by fitting ΔE (with π^0 veto). Combined result is obtained from the simultaneous fit. Reconstruction efficiency, total efficiency and no. of signal events (from individual fits) are also shown.

4.7.3 Branching Fractions from the Simultaneous Fit

The data sample used, contains 274.8 million $B\bar{B}$ events. All selection requirements are applied (tables 4.28 and 4.8).

The statistical significance is defined as $\sqrt{-2ln(\mathcal{L}(0)/\mathcal{L}_{max})}$ where $\mathcal{L}_{max}$ is the maximum likelihood and $\mathcal{L}(0)$ is the maximum likelihood if there is no signal.

Mode	rec. eff.(%)	tot. eff.($\times 10^{-4}$)	Sig.	Br($\times 10^{-5}$)
$D_s^*\pi^0$				
$\phi\pi$	3.85 ± 0.23	6.42 ± 1.67	4.34 ± 2.49	2.46 ± 1.55
$K_S K$	2.45 ± 0.46	2.84 ± 0.95	2.68 ± 2.96	3.44 ± 3.97
$K^* K$	3.07 ± 0.39	6.53 ± 1.96	3.55 ± 3.65	2.04 ± 1.08
combined				2.43 ± 1.11
$D_s^{*+}\pi^-$				
$\phi\pi$	8.47 ± 0.29	14.13 ± 3.59	5.08 ± 3.32	1.31 ± 0.58
$K_S K$	3.73 ± 0.68	5.32 ± 1.64	7.42 ± 3.55	6.24 ± 2.29
$K^* K$	3.05 ± 0.36	6.53 ± 1.94	4.32 ± 2.84	2.49 ± 1.20
combined				2.14 ± 0.81
$D_s^{*-}K^+$				
$\phi\pi$	6.47 ± 0.24	10.80 ± 2.75	4.31 ± 2.49	1.45 ± 0.70
$K_s K$	3.14 ± 0.58	3.64 ± 1.22	2.51 ± 2.03	2.51 ± 1.58
$K^* K$	5.20 ± 0.60	11.03 ± 3.27	4.77 ± 3.53	1.61 ± 0.74
combined				1.64 ± 0.66

Table 4.8: Branching fractions by fitting ΔM (with π^0 veto). Combined result is obtained from the simultaneous fit. Reconstruction efficiency, total efficiency and no. of signal events(from individual fits) are also shown.

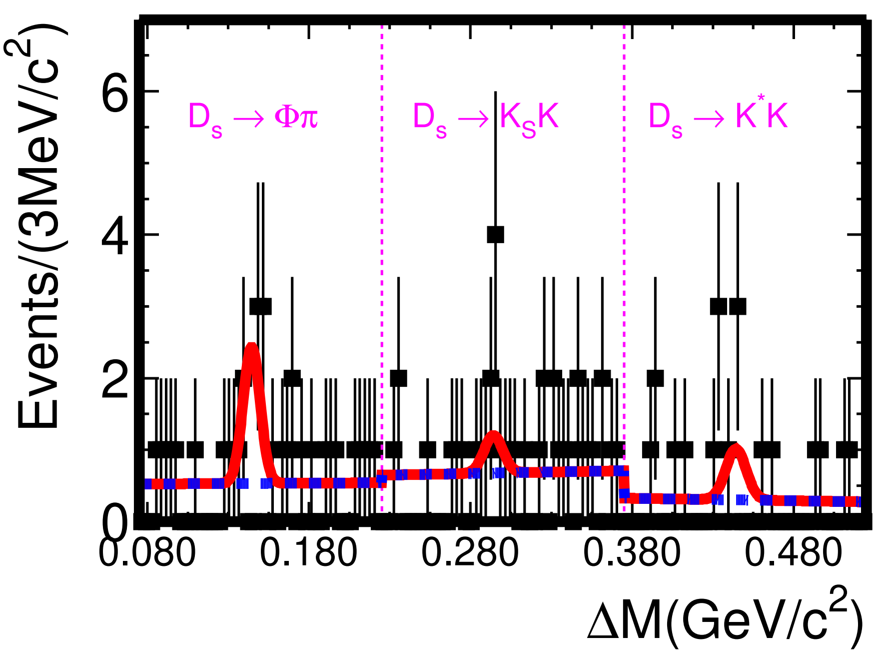

Figure 4.26: Simultaneous fit for ΔM for $D_s^{*+}\pi^+$ mode (with π^0 veto). Data are shown as points with error bars, with fit results overlaid, total (red) and background (blue). Data sample consists of 274.8 million $B\bar{B}$ events. The three peaks in each plot represent the signals for $D_s^+ \to \phi\pi^+$, $D_s^+ \to K_S^0 K^+$ and $D_s^+ \to K^{*0}K^+$ modes.

The branching fractions from the ΔE fit are as follows.

Mode	branching fraction	significance
$B(B^+ \to D_s^{*+}\pi^0)$	$(2.81 \pm 1.46) \times 10^{-5}$	2.90σ
$B(B^0 \to D_s^{*+}\pi^-)$	$(1.82 \pm 0.77) \times 10^{-5}$	4.05σ
$B(B^0 \to D_s^{*-}K^+)$	$(0.97 \pm 0.65) \times 10^{-5}$	2.45σ

The branching fractions from the ΔM fit are as follows.

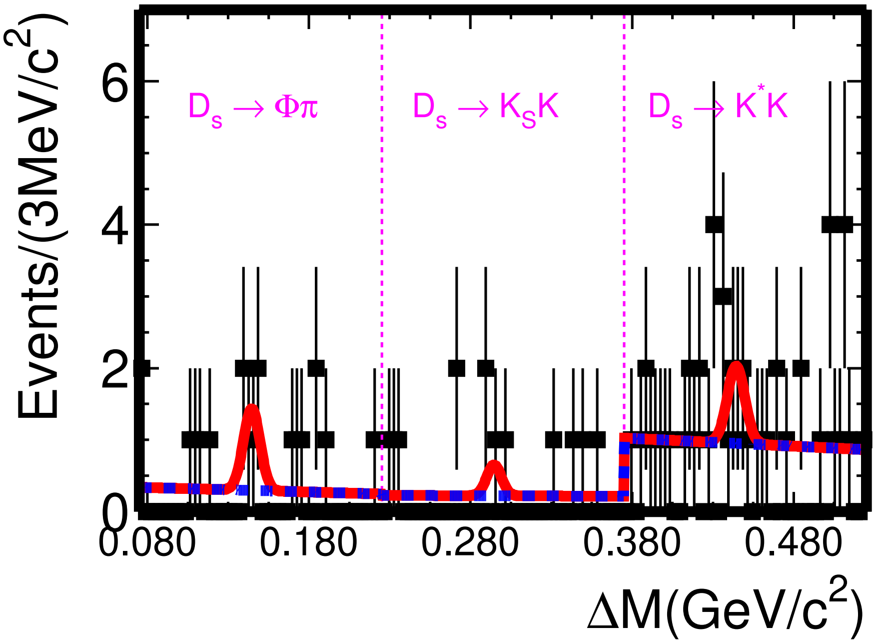

Figure 4.27: Simultaneous fit for ΔM for $D_s^{*+}K^-$ mode (with π^0 veto). Data are shown as points with error bars, with fit results overlaid, total (red) and background (blue). Data sample consists of 274.8 million $B\bar{B}$ events. The three peaks in each plot represent the signals for $D_s^+ \to \phi\pi^+$, $D_s^+ \to K_S^0 K^+$ and $D_s^+ \to K^{*0}K^+$ modes.

Mode	branching fraction	significance
$B(B^+ \to D_s^{*+}\pi^0)$	$(2.43 \pm 1.11) \times 10^{-5}$	4.00σ
$B(B^0 \to D_s^{*+}\pi^-)$	$(2.14 \pm 0.81) \times 10^{-5}$	4.75σ
$B(B^0 \to D_s^{*-}K^+)$	$(1.64 \pm 1.11) \times 10^{-5}$	4.53σ

The errors shown are statistical only. Results from both fits agree each other, within their errors.

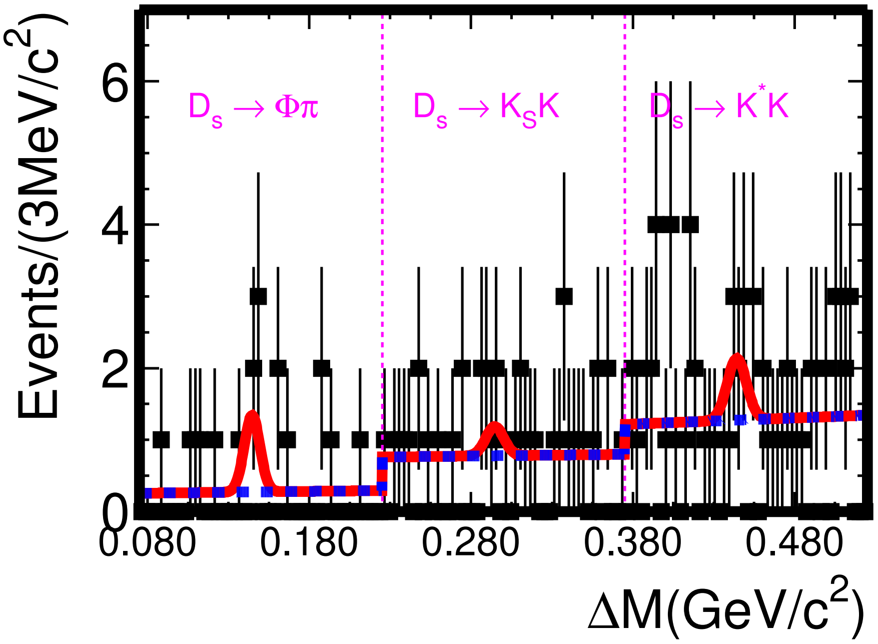

Figure 4.28: Simultaneous fit for ΔM for $D_s^{*+}\pi^0$ mode (with π^0 veto). Data are shown as points with error bars, with fit results overlaid, total (red) and background (blue). Data sample consists of 274.8 million $B\bar{B}$ events. The three peaks in each plot represent the signals for $D_s^+ \to \phi\pi^+$, $D_s^+ \to K_S^0 K^+$ and $D_s^+ \to K^{*0}K^+$ modes.

4.8 Estimation of Systematic Uncertainties

Errors that are not random are considered as systematic errors or systematic uncertainties. There can be many sources of systematic uncertainties.

The largest of the systematic uncertainties comes from the branching fractions of $D_s \to \phi\pi$, $D_s \to \bar{K}_S^0 K$ and $D_s \to \bar{K}^{*0}K$. The uncertainties on $D_s \to \phi\pi$, $D_s \to \bar{K}_S^0 K$ and, $D_s \to \bar{K}^{*0}K$ are 25.0%, 30.6% and 27.3% respectively[**?**].

Belle class 'kid_eff' provides the uncertainty of kaon and pion efficiencies for a given momentum and angle. The angle is measured between the momentum direction and the z-axis. These uncertainties are obtained using an inclusive D^* sample[?]. Each track is associated with a systematic uncertainty of $1 - 1.3\%$[?]. We added all the individual tracking uncertainties for tracks coming from the B candidate to obtain the total tracking uncertainty. The number of $B\bar{B}$ events has a 1%[?] uncertainty. The systematic uncertainty in kaon and pion identification efficiency is estimated as $\sim 1\%$[?]. The total systematic uncertainty due to particle identification is obtained by adding all pion and kaon identification uncertainties linearly for each candidate. Also π^0, K_S, and γ reconstruction efficiencies carry systematic uncertainties of 5%[?], 3% and 5%[?], respectively. Tables 4.12 and 4.13 summarize the systematic uncertainties. The total systematic uncertainty for each mode is taken to be the quadratic sum of individual components.

	$D_s^{*+}\pi^-$			$D_s^{*-}K^+$			$D_s^{*+}\pi^0$		
	$\phi\pi$	K_sK	K^*K	$\phi\pi$	K_sK	K^*K	$\phi\pi$	K_sK	K^*K
No. of $B\bar{B}$	0.009			0.009			0.009		
$B(D_s{}^* \to D_s\gamma)$	0.0276			0.0276			0.0276		
γ recon	0.05			0.05			0.05		
π^0 recon.	-			-			0.05		
total(comm.)	0.058			0.058			0.076		

Table 4.9: Common systematic uncertainties as fractions of signal.

	${D_s}^{*+}\pi^-$			${D_s}^{*-}K^+$			${D_s}^{*+}\pi^0$		
	$\phi\pi$	K_SK	K^*K	$\phi\pi$	K_SK	K^*K	$\phi\pi$	K_SK	K^*K
K_S recon.	0.0	0.03	0.0	0.0	0.03	0.0	0.0	0.03	0.0
$\frac{Br(D_s)}{Br(D_s\to\phi\pi)}$	0.00	0.222	0.091	0.00	0.222	0.091	0.00	0.222	0.091
$Br(\text{sub } D_s)$	0.014	0.004	0.002	0.014	0.004	0.002	0.014	0.004	0.002
tracking		0.044			0.045			0.034	
PID		0.040			0.039			0.029	
MC stat.		0.045			0.061			0.081	
fitting		0.082			0.094			0.149	
common		0.058			0.058			0.076	
total		0.120			0.143			0.180	
$Br(D_s \to \phi\pi)$		0.250			0.250			0.250	

Table 4.10: Total systematic uncertainties for the three decay modes, as fractions of signal.

Anal. Mode	D_s Mode	D_s Sideband		ΔM Sideband		Signal Region	
		Non Peak.	Peak.	Non Peak.	Peak.	Non Peak.	Peak.
$D_s^*\pi^0$	$\phi\pi$	7.80 ± 1.53	12.38 ± 4.78	16.91 ± 2.23	0.94 ± 3.88	22.38 ± 2.54	-0.48 ± 4.02
	K_sK	33.38 ± 3.25	3.17 ± 5.83	34.67 ± 3.25	6.03 ± 6.35	32.31 ± 3.18	-0.68 ± 5.60
	K^*K	64.08 ± 4.69	-1.62 ± 8.16	55.17 ± 4.49	1.39 ± 7.60	80.47 ± 4.93	0.00 ± 0.10
$D_s^*\pi$	$\phi\pi$	28.21 ± 3.09	-8.91 ± 3.48	32.06 ± 3.68	3.63 ± 5.58	49.81 ± 4.07	-5.65 ± 5.37
	K_SK	56.36 ± 4.19	-11.73 ± 5.41	64.16 ± 4.49	$6.83 \pm \pm 7.74$	71.48 ± 4.73	15.89 ± 8.79
	K^*K	106.88 ± 5.63	1.25 ± 8.89	115.32 ± 5.88	10.04 ± 10.23	134.36 ± 6.34	23.64 ± 11.67
D_s^*K	$\phi\pi$	20.92 ± 2.50	8.60 ± 5.26	22.00 ± 2.60	7.30 ± 5.43	24.67 ± 2.71	0.93 ± 4.71
	K_SK	31.86 ± 2.73	9.31 ± 6.00	37.06 ± 2.97	-7.64 ± 3.92	31.76 ± 2.75	13.63 ± 6.69
	K^*K	77.53 ± 5.31	-11.50 ± 6.55	75.68 ± 5.25	-10.37 ± 6.90	61.90 ± 4.74	0.69 ± 6.86

Table 4.11: Estimated background from generic Monte Carlo sidebands of D_s and ΔM. Analysis Mode, D_s^+ decay mode, D_s sideband region, ΔM sideband region and signal region are shown. Non peaking (non. peak.) and Peaking (peak.) backgrounds are indicated separately in each column. The generic Monte Carlo data set used, is equivalent to a data set containing 154 million $B\bar{B}$ events.

Anal. Mode	D_s Mode	D_s Sideband		ΔM Sideband		Signal Region	
		Non Peak.	Peak.	Non Peak.	Peak.	Non Peak.	Peak.
$D_s^*\pi^0$	$\phi\pi$	9.87 ± 1.51	-1.68 ± 2.00	9.81 ± 1.54	2.70 ± 3.21	11.82 ± 1.66	2.98 ± 3.18
	K_sK	32.75 ± 2.83	-1.25 ± 4.49	31.84 ± 2.82	0.99 ± 4.75	30.97 ± 2.66	-0.00 ± 0.07
	K^*K	63.18 ± 4.20	5.50 ± 7.44	63.67 ± 4.38	0.00 ± 0.21	63.43 ± 4.22	13.97 ± 8.13
$D_s^*\pi$	$\phi\pi$	27.88 ± 3.42	0.44 ± 5.90	23.73 ± 2.52	3.09 ± 4.21	27.91 ± 2.75	2.31 ± 4.48
	K_SK	51.78 ± 3.62	5.30 ± 6.39	58.99 ± 3.81	$-5.61 \pm \pm 5.26$	61.02 ± 3.92	7.22 ± 6.87
	K^*K	104.81 ± 5.04	8.62 ± 9.06	110.25 ± 5.15	15.86 ± 9.46	126.74 ± 5.28	36.75 ± 13.34
D_s^*K	$\phi\pi$	15.58 ± 1.93	-5.80 ± 2.06	17.54 ± 2.04	-3.00 ± 2.69	19.38 ± 2.18	7.39 ± 4.72
	K_SK	34.61 ± 2.54	-5.17 ± 3.94	30.00 ± 2.41	9.96 ± 5.78	35.01 ± 2.56	2.56 ± 4.73
	K^*K	95.08 ± 5.25	-5.28 ± 7.29	71.98 ± 4.57	-1.58 ± 6.54	69.72 ± 4.51	4.41 ± 6.91

Table 4.12: Estimated background from sidebands of D_s and ΔM. Analysis Mode, D_s^+ decay mode, D_s sideband region, ΔM sideband region and signal region are shown. Non peaking (non. peak.) and Peaking (peak.) backgrounds are indicated separately in each column. The data set used, contains 154 million $B\bar{B}$ events.

Analysis Mode	D_s Decay Mode	N	ϵ%	Generic Background	Peaking Background	Total Background	Br $\times 10^{-5}$
${D_s}^*\pi^0$	$\phi\pi$	8	3.85 ± 0.23	2.09 ± 0.74	< 0.01	2.10 ± 0.74	3.34 ± 1.18
	K_sK	13	2.45 ± 0.46	11.44 ± 1.79	0.83 ± 0.48	12.27 ± 1.85	0.94 ± 0.26
	K^*K	25	3.15 ± 0.39	23.36 ± 2.68	2.20 ± 0.78	25.56 ± 2.79	$-0.31 \pm .0.06$
	total	46	-	36.89 ± 3.40	3.03 ± 0.92	39.93 ± 3.43	$2.55^{+1.30}_{-1.09}$ < 5.12 (90 % C.L.)
${D_s}^*\pi$	$\phi\pi$	14	8.47 ± 0.29	8.61 ± 1.63	< 0.04	8.65 ± 1.63	1.38 ± 0.37
	K_sK	14	3.73 ± 0.68	6.20 ± 1.32	1.79 ± 0.74	7.99 ± 1.50	5.06 ± 1.35
	K^*K	11	3.15 ± 0.36	4.02 ± 1.04	0.61 ± 0.17	4.65 ± 1.05	3.50 ± 1.05
	total	39	-	18.83 ± 2.34	2.44 ± 0.74	21.27 ± 2.46	$2.32^{+0.93}_{-0.83}$
${D_s}^*K$	$\phi\pi$	6	6.47 ± 0.24	4.30 ± 1.07	< 0.12	4.38 ± 1.07	0.55 ± 0.22
	K_sK	4	3.14 ± 0.58	1.64 ± 0.58	< 0.06	1.68 ± 0.58	2.32 ± 1.16
	K^*K	19	5.32 ± 0.60	14.19 ± 2.19	0.04 ± 0.04	14.23 ± 2.19	1.57 ± 0.36
	total	29	-	20.13 ± 2.51	0.04 ± 0.04	20.29 ± 2.51	$1.13^{+0.77}_{-0.66}$

Table 4.13: Branching fractions using counting technique. The above table shows the no. of events in the signal box (N),generic background, peaking background, total background and the branching fraction (Br). The total branching fractions correspond to the related maximum likelihoods.

Chapter 5

Results and Conclusion

5.1 Branching fractions and Upper Limits of $B \to D_s^* h$ Decays

Branching fractions are obtained using the counting technique, simultaneous fit of ΔM and simultaneous fit of ΔE. Of the three sets of results, the simultaneous fit of ΔM gives most consistent results (tables 4.28 and 4.8. For the decays $B^0 \to D_s^{*+}\pi^-$ and $B^0 \to D_s^{*-}K^+$ significant signals have been observed.

$$Br(B^+ \to D_s^{*+}\pi^0) = (2.43 \pm 1.11 \pm 0.42 \pm 0.61) \times 10^{-5} \tag{5.1}$$

$$< 4.69 \times 10^{-5} \text{ (at 90\% C. L.)} \tag{5.2}$$

$$Br(B^0 \to D_s^{*+}\pi^-) = (2.14 \pm 0.81 \pm 0.26 \pm 0.54) \times 10^{-5} \tag{5.3}$$

$$Br(B^0 \to D_s^{*-}K^+) = (1.64 \pm 0.66 \pm 0.23 \pm 0.41) \times 10^{-5} \tag{5.4}$$

The first error is statistical, and the second is systematic excluding the systematic error from the branching fraction of $D_s \to \phi\pi$. The third error is from the branching fraction of $D_s \to \phi\pi$.

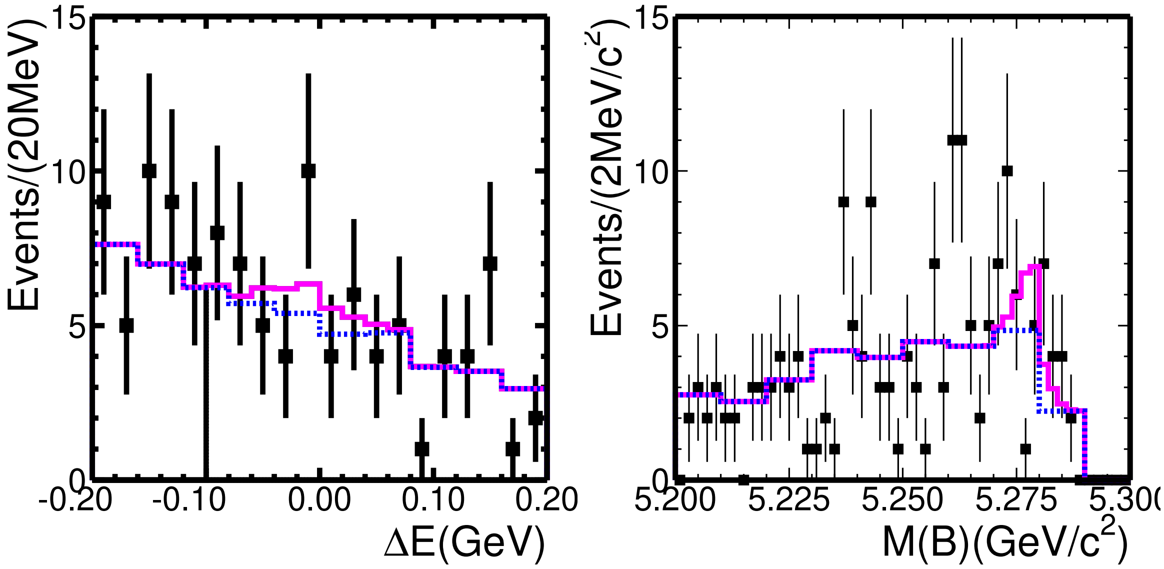

Figure 5.1: ΔE (left) and $M(B)$ (right) for $D_s^{*+}\pi^0$ after combining all three D_s decay channels together. Data are shown as points with error bars, with fit results overlaid as histograms, total (solid) and background (dotted).

5.2 Measurements for V_{db} and $R_{D^*\pi}$

Extracting the value of $|V_{db}|$

From equation 3.1[?],

$$\Gamma(\bar{B}^0 \to {D_s}^{*-}\pi^+) = 5.1 a_1^2 |V_{ub} V_{cs}^*|^2 10^{12} s^{-1}. \tag{5.5}$$

$$|V_{ub}|^2 = \frac{\Gamma(\bar{B} \to {D_s}^{*-}\pi^+)}{5.1 a_1^2 \times |V_{cs}^*|^2 10^{12}} \tag{5.6}$$

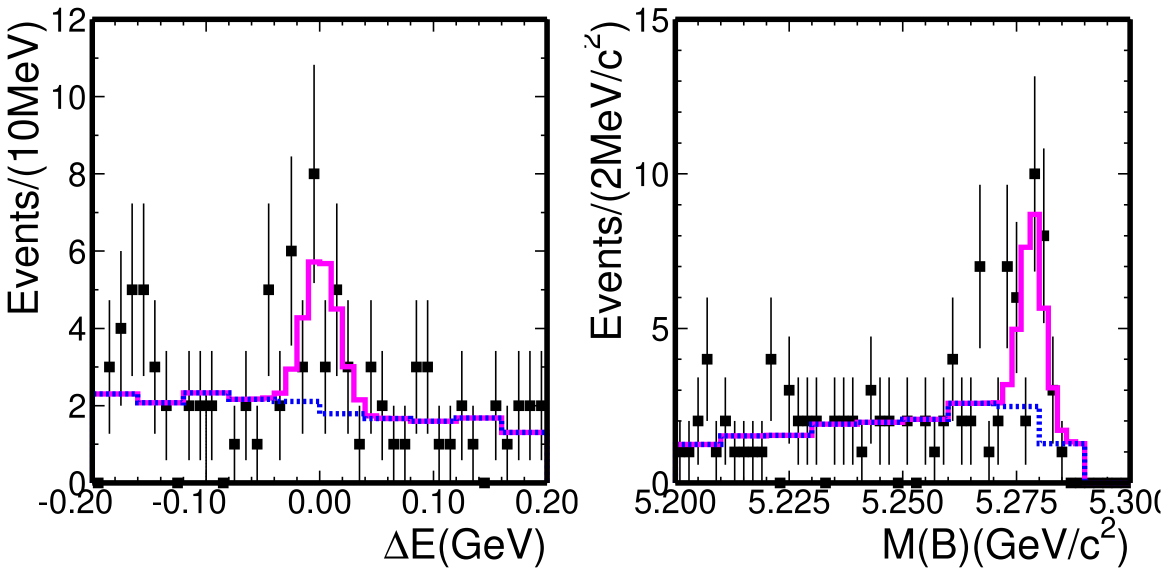

Figure 5.2: ΔE (left) and $M(B)$ (right) for $D_s^{*+}\pi^-$ after combining all three D_s decay channels together. Data are shown as points with error bars, with fit results overlaid as histograms, total (solid) and background (dotted).

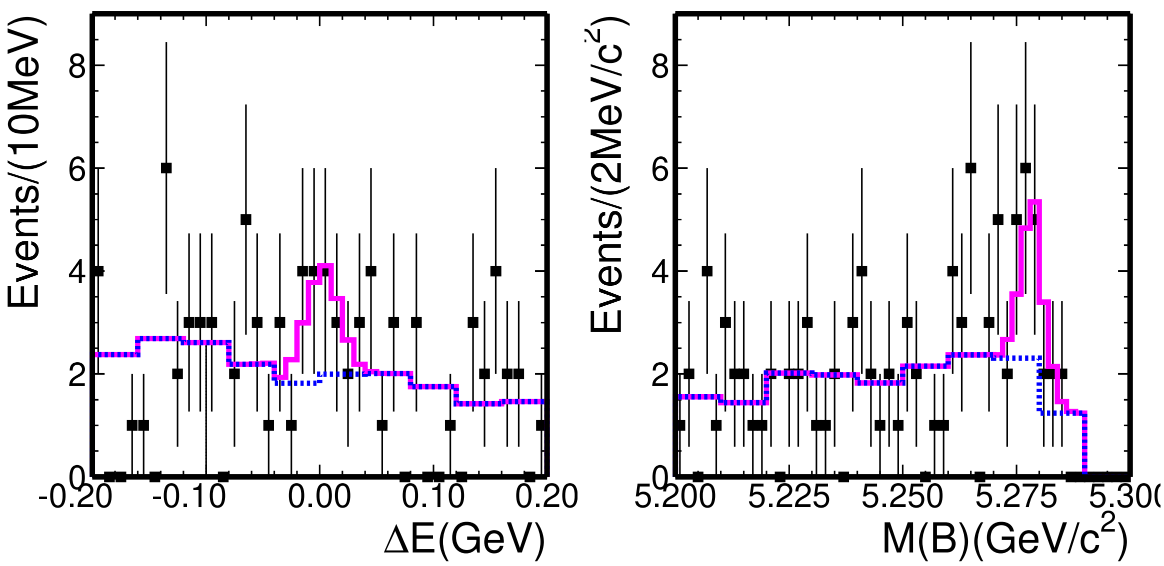

Figure 5.3: ΔE (left) and $M(B)$ (right) for $D_s^{*-}K^+$ after combining all tree D_s decay channels together. Data are shown as points with error bars, with fit results overlaid as histograms, total (solid) and background (dotted).

Assuming $a_1 \approx 1.0$, and the average life time of the neutral B meson, $\tau_{B^0} = (1.542 \pm 0.016) \times 10^{-12}$ s and $V_{cs} = 0.996 \pm 0.013$. Using $B(\bar{B} \to {D_s}^{*-}\pi^+) = (2.14 \pm 0.81 \pm 0.26 \pm 0.54) \times 10^{-5}$

$$|V_{ub}|^2 = \frac{Br(\bar{B}^0 \to {D_s}^{*-}\pi^+)/(1.542\times10^{-12})}{5.1\times0.974\times10^{12}} \tag{5.7}$$

$$\therefore |V_{ub}| = \sqrt{\frac{(2.14\times10^{-5})/(1.542\times10^{-12})}{5.1\times(0.996)^2\times10^{12}}} \tag{5.8}$$

$$= (1.66 \pm 0.78) \times 10^{-3} \tag{5.9}$$

Also from equation 3.3[?],

$$\Gamma(\bar{B} \to {D_s}^{*-}\pi^+) = 0.34|V_{ub}/V_{cb}|^2[C_1'(m_b)]^2 10^{10} s^{-1} \tag{5.10}$$

$$|V_{ub}| = \sqrt{\frac{(2.14\times10^{-5}/1.542\times10^{-12})\times(0.0413)^2}{0.34\times10^{10}}} \tag{5.11}$$

$$= (2.64 \pm 1.26) \times 10^{-3} \tag{5.12}$$

The average value of $|V_{cb}|$ is given as 0.0413 ± 0.0015 which is used in the above calculation, in PDG [?]. Results for V_{ub} can be summarized as follows.

$V_{ub} = (1.66 \pm 0.78) \times 10^{-3}$; A. Deandrea et al.[?]

$= (2.64 \pm 1.26) \times 10^{-3}$; D. Choudhury et al.[?]

Values from the two methods proposed by A. Deandrea et al. and D. Choudhury et al. agrees each other within the errors. The errors are dominated by the errors on the branching fraction of $\bar{B} \rightarrow {D_s}^{*-}\pi^+$. Following exclusive $|V_{ub}|$ measurements can also be found[**?**].

mode	$\lvert V_{db}\rvert \times 10^{-3}$	q^2 range	Form Factor model
CLEO 00 $\rho l\nu$	$3.23 \pm 0.24^{+0.23}_{-0.26} \pm 0.58$	all	model survey
BaBar 01 $\rho l\nu$	$3.64 \pm 0.22 \pm 0.25^{+0.39}_{-0.56}$	all	model survey
CLEO 03 $\pi l\nu$	$3.33 \pm 0.24 \pm 0.15 \pm 0.06^{+0.57}_{-0.40}$	$q^2 < 16$ GeV^2	LCSR
CLEO 03 $\pi l\nu$	$2.88 \pm 0.55 \pm 0.30 \pm 0.18^{+0.45}_{-0.35}$	$q^2 > 16$ GeV^2	LQCD
CLEO 03 $\pi l\nu$	$3.24 \pm 0.22 \pm 0.13 \pm 0.09^{+0.55}_{-0.39}$	average	
CLEO 03 $\rho l\nu$	$2.67 \pm 0.27^{+0.38}_{-0.42} \pm 0.17^{+0.47}_{-0.35}$	$q^2 < 16$ GeV^2	LCSR
CLEO 03 $\rho l\nu$	$3.34 \pm 0.32^{+0.27}_{-0.36} \pm 0.47^{+0.50}_{-0.40}$	$q^2 > 16$ GeV^2	LQCD
CLEO 03 $\rho l\nu$	$3.00 \pm 0.21^{+0.29}_{-0.35} \pm 0.28^{+0.49}_{-0.38}$	average	
CLEO 03 $\pi + \rho$	$3.17 \pm 0.17^{+0.16}_{-0.17} \pm 0.03^{+0.53}_{-0.39}$	average	
CLEO 03 $\pi + \rho$	$3.26 \pm 0.19 \pm 0.15 \pm 0.04^{+0.54}_{-0.39}$	average	no $\rho l\nu$ LCSR

The models used in above measurements are light cone sum rules (LCSR) and lattice QCD (LQCD).The errors for CLEO 0 and BaBar 01 are from statistical, experimental systematic, and form factor modeling uncertainties respectively. For the CLEO 03 measurements, the errors are from statistical, experimental systematics, $\rho l\nu$ form factor, and LQCD and LCSR calculations uncertainties, respectively.

Summary of inclusive V_{ub} measurements are shown below.

	$\lvert V_{ub}\rvert \times 10^{-3}$	
ALEPH	$4.12 \pm 0.67 \pm 0.76$	neural net
L3	$5.70 \pm 1.00 \pm 1.40$	cut and count
DELPHI	$4.07 \pm 0.65 \pm 0.61$	M_X
OPAL	$4.00 \pm 0.71 \pm 0.71$	neural net
LEP avg.	$4.09 \pm 0.37 \pm 0.56$	
CLEO	$4.05 \pm 0.61 \pm 0.65$	$d\Gamma/dq^2 dM_X^2 dE_l$
Belle	$5.00 \pm 0.64 \pm 0.65$	$M_x,\ D^* l\nu$ tag
CLEO	$4.11 \pm 0.13 \pm 0.31 \pm 0.46 \pm 0.28$	$2.2 < p < 2.6$
BaBar	$4.31 \pm 0.20 \pm 0.20 \pm 0.49 \pm 0.30$	$2.3 < p < 2.6$
Belle	$3.99 \pm 0.17 \pm 0.16 \pm 0.45 \pm 0.27$	$2.3 < p < 2.6$
Belle	$4.63 \pm 0.28 \pm 0.39 \pm 0.48 \pm 0.32$	$M_X < 1.7,\ q^2 > 8$
BaBar	$4.79 \pm 0.29 \pm 0.28 \pm 0.60 \pm 0.33$	$M_X < 1.55$

The errors in the first group experimental and theoretical uncertainties. The errors in the second group is from the statistical, experimental systematic, E_γ-based rate fraction, and Γ_{tot} uncertainties.

In PDG[**?**], an average value including all exclusive and inclusive results, for V_{ub} is given as $(3.67 \pm 0.47) \times 10^{-3}$. Both methods give lower values comparing with the average PDG value. The value obtained by the method proposed by D. Choudhury et al., agrees with the PDG value with in errors.

Calculating $R_{D^*\pi}$

Using the equation 3.11,

$$R_{D^*\pi} = \tan\theta_C \sqrt{\frac{Br(B^0 \to D_s^{(*)+}\pi^-)}{Br(B^0 \to D^{(*)-}\pi^+)}} \times \frac{f_{D^{(*)}}}{f_{D_s^{(*)}}}. \tag{5.13}$$

where $\frac{f_{D^{(*)}}}{f_{D_s^{(*)}}} = 1.10 \pm 0.02$[**?**] and $Br(B^0 \to D^{(*)-}\pi^+) = (2.76 \pm 0.21) \times 10^{-3}$[**?**]. The Cabibbo angle is given by $\sin\theta_C = 0.2229 \pm 0.0022$[**?**] . Therefore $\tan\theta_C = 0.2286 \pm 0.0023$.

$$R_{D^*\pi} = 0.2286\sqrt{\tfrac{2.14\times10^{-5}}{2.76\times10^{-3}}} \times 1.10. \tag{5.14}$$

$$= (2.21 \pm 0.53) \times 10^{-2} \tag{5.15}$$

The expected value for $R_{D^*\pi}$ is ~ 0.02[**?**], which is in good agreement with our measurement.

5.2.1 Summary

In this analysis, three B decay modes, $B^0 \to D_s^{(*)+}\pi^-$, $B^+ \to D_s^{(*)+}\pi^0$ and, $B^0 \to D_s^{(*)-}K^+$ were searched. Evidence for $B^0 \to D_s^{(*)+}\pi^-$ was seen. We have been able to make two important measurements, one is estimating V_{ub}, which is one of the least accurately measured CKM matrix element. The other is estimating $R_{D^*\pi}$ which is an important parameter required to measure $\sin(2\phi_1 + \phi_3)$. This measurement provides the opportunity to estimate $\sin(2\phi_1+\phi_3)$ in the time dependent CP violating measurements in $B \to D^*\pi$ decays.

Appendix A

A.1 Particle Identification (PID) System at Belle

Kaon and pion identification is an important part since it needs for the reconstruction of exclusive decay modes. It is also required to determine the flavor of the B meson and is a very important to measure CP violation. Two body decays such as $B \to \pi\pi$ and $B \to \pi K$ produces final state particles with momenta in the range 1.5 to 3.8 GeV/c. Therefore the PID system must be capable of discriminating kaons pions in a broad momentum range.

Belle uses the information of three sub detectors; the Central Drift Chamber (CDC), the Time of Flight counters (TOF), and the aerogel Cerenkov counters (ACC). The CDC provides discrimination between particles using energy loss (dE/dx) measurements. The TOF counter uses time of flight of the particles, with their momentum to identify particles. It provides more than 3σ separation for momenta up to 1.2 GeV/c. In the ACC the choice of refractive index for the barrel is optimized for separating high momentum pions and kaons.

A.1.1 Likelihood ratio

It is useful to combine the information of the three sub detectors into a single variable. This is done by using the likelihood method in the following way. The likelihood of the detector response due to signal particle species, is compared to the likelihood for an assumed background particle species as follows[?].

$$\mathrm{Prob(i{:}j)} = \frac{P_i}{P_i + P_j} \tag{A.1}$$

where P_i is the likelihood calculated for the signal species and P_j is the likelihood for the background species. i and j can be any of the five particle species, e, μ, π, K and p.

Each P_i in the above equation is a product of likelihoods of the three sub detectors.

$$P_i = P_i^{CDC} \times P_i^{TOF} \times P_i^{ACC} \tag{A.2}$$

A.1.2 K/π Separation

ACC provides good Kπ separation in the momentum region, 1.5 to 3.5 GeV. TOF provides a good separation below 1.2 while dE/dx provide good separation in the regions of momentum below 0.8 GeV/c and above 2.5 GeV/c.

A.2 K_S^0 Selection

K_S mesons are reconstructed using $K_S \to \pi^+\pi^-$ decay. K_S candidates are stored in Mdst_vee2 table with 30 MeV mass window selection, without any track or vertex

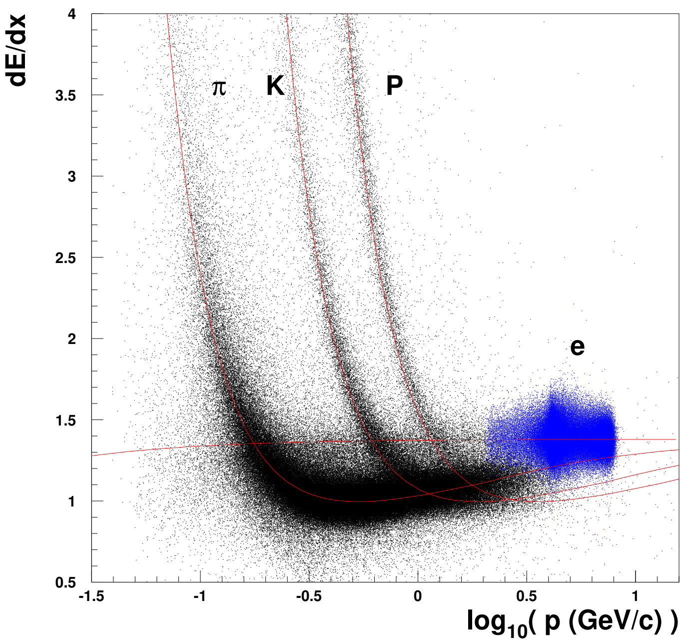

Figure A.1: Expected mean energy loss ($< dE/dx >$) versus momentum observed in collision data. Expected curves for pions, Kaons and protons are superimposed.

quality selection[**?**]. Three variables, $\delta\phi$, dr and χ^2 are used for the selection of K_S. $\delta\phi$ is the angle between the projections of the momentum vector and the decay vertex displacement vector in the $r-\phi$ plane. dr is the smaller of $dr1$ and $dr2$, which are the nearest approach from the Interaction Point (IP) to the two tracks in x-y plane. The variance of the vertex reconstruction quality of the two pion tracks is denoted by χ^2. Using the shapes of $\delta\phi$ and dr for simulated signal and simulated background events, best selection criteria was obtained. With the selections, $\chi^2 < 30$, $dr > 0.009$ cm, and $\delta\phi < 0.2$ rad, 90% of the background was removed, keeping 84% of the signal.

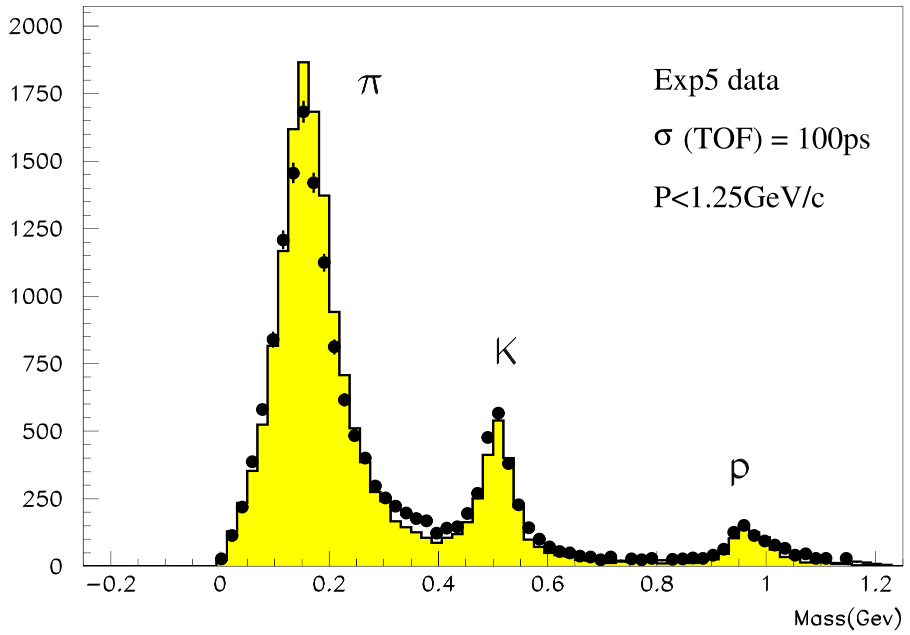

Figure A.2: Distribution of hadron mass calculated from measured time-of-flight and momentum

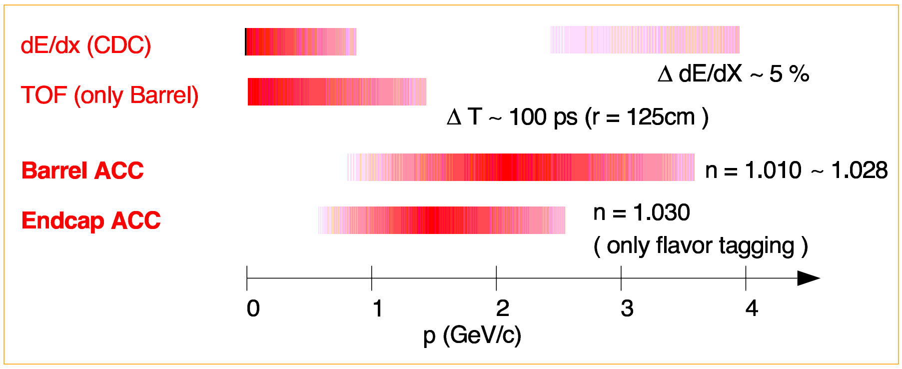

Figure A.3: Momentum coverage of each sub-detector

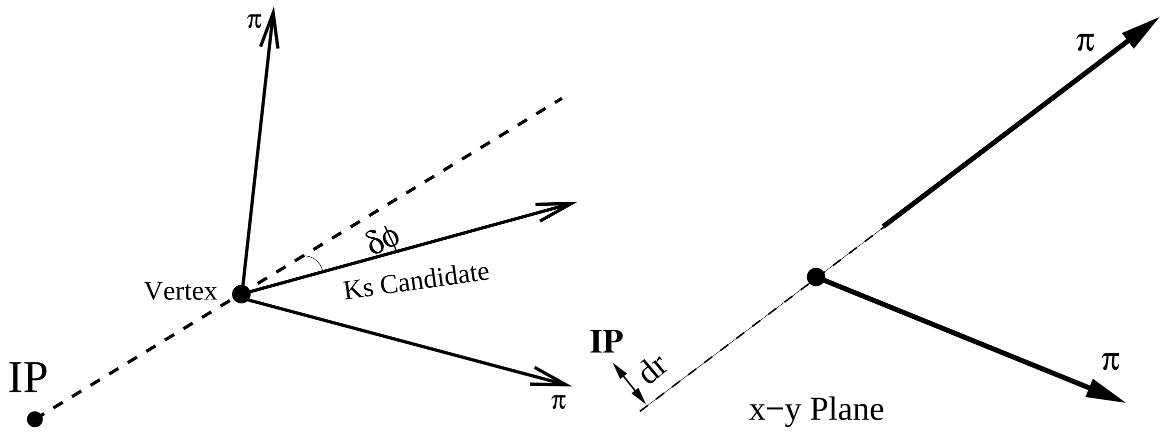

Figure A.4: K_S selection: Angle between the projections of the momentum vector and the decay vertex displacement vector (top) in $r-\phi$ plane and the smaller of $dr1$ and $dr2$(i.e. dr) which are the smallest approach from the IP (bottom) to the two tracks in the x-y plane.

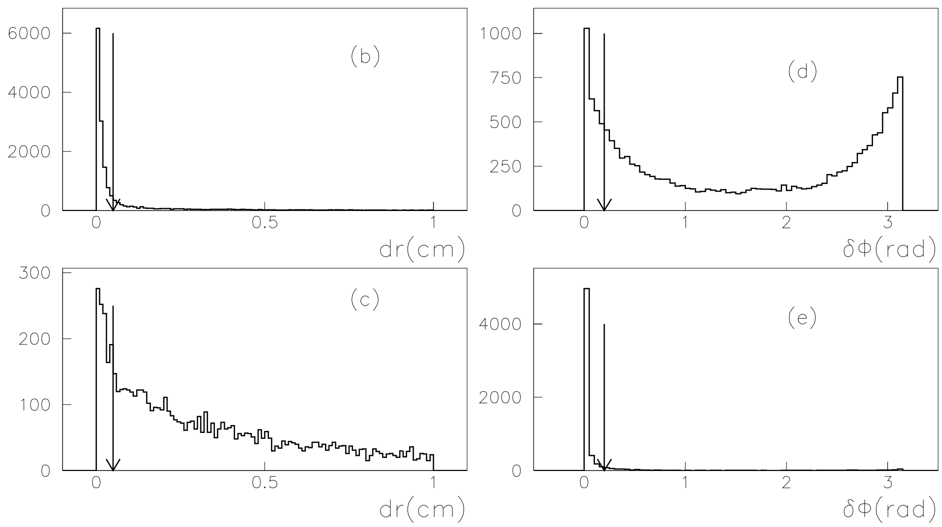

Figure A.5: K_S selection: dr and $\delta\phi$ distribution for real K_S events and background events. Plots (b) and (d) are for the background events, and plots (c) and (e) are for true K_S candidates. Signal Monte Carlo events were used for this study.

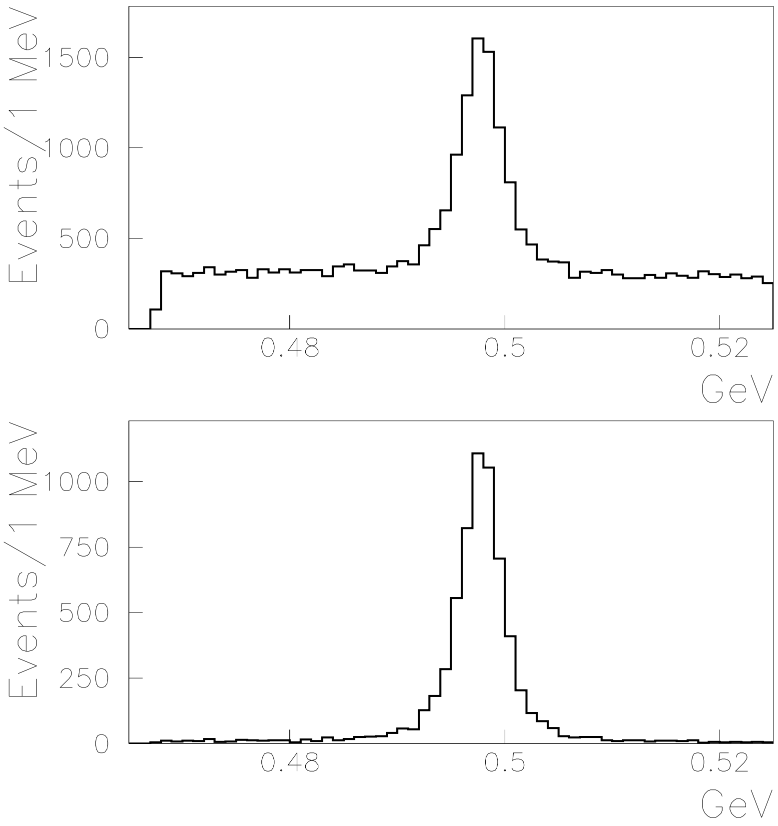

Figure A.6: K_S selection: Invariant mass distribution of K_S, before (top) and after (bottom) the selection criteria, using signal Monte Carlo events.

Bibliography

[1] N. Cabibbo, Phys. Rev. Lett. **10**, 531 (1963).

[2] M. Kobayashi and T. Maskawa, Prog. Theor. Phys. **49**, 652 (1973).

[3] S. Eidelman et al., Particle Data Group, Phys. Lett. B **592**, 1 (2004).

[4] L. Wolfenstein, Phys. Rev. Lett. **51**, 1945 (1983).

[5] J. H. Christenson et al., Phys. Rev. Lett **13**, 138 (1964).

[6] Commissionning of KEKB, **http://www-kekb.kek.jp/Publication/NIM/**.

[7] G. Alimonti et al., Belle Collaboration, Nucl. Instrum. Meth. A **453**, 71 (2000).

[8] H. Hirano et al., Nucl. Instrum. Meth. A **455**, 294 (2000).

[9] T. Iijima et al., Nucl. Instrum. Meth. A **453**, 321 (2000).

[10] K. Suzuki, Ph. D thesis, Graduate School of Science and Technology, Chiba University (2001).

[11] T. Iijima et al., Nucl. Instrum. Meth. A **453**, 315 (2000).

[12] Y. Ushiroda, H. Hirano et al., Nucl. Instrum. Meth. A **511**, 6 (2003).

[13] G. Taylor, H. Hirano et al., Nucl. Instrum. Meth. A **511**, 22 (2003).

[14] K. Miyabayashi, Nucl. Instrum. Meth. A **494**, 298 (2002).

[15] http://belle.kek.jp/group/ecl/ .

[16] B. Block and I. Halperin, Phys. Lett. **385**, 324 (1996).

[17] B. Block and M. Gronau, Phys. Rev. Lett. **78**, 3999 (1997).

[18] R. Fulton et al., CLEO collaboration, Phys. Rev. Lett. **64**, 16 (1990).

[19] J. Bartelt et al., CLEO collaboration, Phys. Rev. Lett. **71**, 324 (1993).

[20] A. Deandrea et al., CLEO collaboration, Phys. Lett. B **318**, 549 (1993).

[21] D. Choudhury et al., Phys. Rev. D **45**, 217 (1992).

[22] I. Dunietz and R. G. Sachs, Phys. Rev. D **37**, 3186 (1988).

[23] T. Gershon, Belle Note **722** (2004).

[24] B. Aubert et al., arXiv:hep-ex/0308018 v1 (2003).

[25] D. Becirevic, Nucl. Phys. Proc. Suppl. **94**, 337 (2001).

[26] P. Krokovny et al., Belle Collaboration, Phys. Rev. Lett. **89**, 231804 (2002).

[27] B. Collaboration, Phys. Rev. D **64**, 072001 (2001).

[28] T. E. Browder and K. Honscheid, Prog. in Part. Nucl. Phys. **35**, 81 (1995).

[29] http://www.lns.cornell.edu/public/CLEO/soft/QQ/ .

[30] http://hep.ucsb.edu/people/lange/EvtGen/ .

[31] K. Abe et al., Belle Collaboration, Phys. Lett. B **511**, 151 (2001).

[32] S. Brandt et al., Phys. Lett **12**, 57 (1964).

[33] E. Fahri, Phys. Rev. Lett. **39**, 1587 (1977).

[34] D. M. Asner et al., CLEO Collaboration, Phys. Rev. D **53**, 1039 (1996).

[35] H. Albrecht et al., ARGUS Collaboration, Z. Phys. C, **48**, 543 (1990).

[36] H. Hamasaki et al., Belle Note 321, KID Group (2000).

[37] http://belle.kek.jp/~hitoshi/private/track/error/index.html .

[38] http://belle.kek.jp/secured/nbb/nbb.html .

[39] http://belle.kek.jp/group/pid_joint/ .

[40] A. Drutskoy et al., Belle Collaboration **hep-ex/0409026** (2004).

[41] J. L. R. Denis A. Suprun, Cheng-Wei. Chiang, Phys. Rev. D **65**, 054025 (2002).

[42] F. Fang, Belle Note 323, Study of $K_S \to \pi\pi$ selection (2000).